

THE  
UNIVERSITY OF SASKATCHEWAN  
SEISMOGRAPH NETWORK

CRAIG W. FUNK

1992

THE UNIVERSITY OF SASKATCHEWAN SEISMOGRAPH NETWORK

A THESIS

SUBMITTED TO THE FACULTY OF GRADUATE STUDIES AND RESEARCH

IN PARTIAL FULFILLMENT OF THE REQUIREMENTS

FOR THE DEGREE OF

MASTER OF SCIENCE

IN THE

DEPARTMENT OF GEOLOGICAL SCIENCES

UNIVERSITY OF SASKATCHEWAN

SASKATOON

By

Craig W. Funk

© 1992. C.Funk

The author has agreed that the library of the University of Saskatchewan may make this thesis available for inspection. Also, the author has agreed that permission for extensive copying of this thesis for scholarly purposes may be granted by the professor or professors who supervised the thesis work recorded herein, or, in their absence, by the head of the Department, or the Dean of the College in which the thesis work was done. It is understood that due recognition will be given to the author of this thesis. Copying, or publication, or any other use of the thesis for financial gain without approval by the University of Saskatchewan and the author's written permission is prohibited.

Requests for permission to copy or to make any use of material in this thesis in whole or in part should be addressed to:

Department Head of Geological Sciences

University of Saskatchewan

Saskatoon

CANADA S7N 0W0

## ACKNOWLEDGEMENT

I wish to express my gratitude to Dr. D.J. Gendzwill of the Department of Geological Sciences, University of Saskatchewan, for his support, supervision and advice. I am especially indebted to him for helping me organise this thesis in the short time period that was available.

My committee members, Drs. R. Renaut, D. Stead, H. Hendry, and the external examiner, Dr. J. Wilson, have given helpful suggestions to this work.

Mr. J. Arnold and Cominco Fertilizers provided the instrumentation support. Mr. B. Reilkoff of Academic Computing Services, University of Saskatchewan, gave advice on the computer programing that was required.

I express my sincere thanks to A. Prugger, L. Ruo, B. Chornobay, and A. Bezdan for their critical reviews of the thesis.

I am especially grateful to Miss R. Gorchinski for her technical help. Mrs. L. Embree has also given some technical assistance.

I was supported, during this study, through Dr. D.J. Gendzwill by research grants from Energy, Mines, and Resources of Canada.

This thesis is dedicated to my special friend, Rachel

Abstract

This thesis discusses the work completed on the University of Saskatchewan Seismograph Network (USSN). The main thrust of the work was the development of an automatic seismic data monitoring algorithm and interactive computer packages which are used to analyze digitally recorded earthquakes. Currently the monitoring package detects two earthquakes, on average, daily. Seven earthquakes within 1500 km of the USSN were detected between the period of September and December of 1991.

The interactive computer packages are used to provide earthquake information such as location, magnitude, and spectral parameters. Instrument calibration is a vital component of the analysis package. A reliable calibration function has been derived for the system by studying the instrument response to known ground-motions, which were introduced into the seismometers electronically.

A direct benefit of the USSN will be a better understanding of seismicity in Saskatchewan and the rest of western Canada. The utility of the network is evaluated by studying the magnitudes of earthquakes which can be reliably recorded. The event resolvibility is limited by the background noise level, whereas the maximum recordable event size is controlled by the inherent limitations of the seismographs. The recording range of the instrumentation is

established using results from both an ambient background-noise study and instrument calibration experiments. The investigation shows that earthquakes from southern Saskatchewan, which have magnitudes between 2.5 and 4.0, can be reliably recorded (based on the present seismograph configuration).

Accurate earthquake location requires a keen understanding of the seismic velocity variations within the crust and upper mantle (a crustal model). Earthquake data recorded by the USSN were interpreted to develop a crustal model for the Saskatoon area. The study used seismograms recorded between epicentral distances of 200 and 11 000 km. The interpretation shows that the depth to the base of the crust (Moho), under Saskatoon, is 46 km. Refractions along the Moho, from regional distance earthquakes, have apparent P-wave velocities of 8.3 km/sec. The P-wave velocity in the upper crust is 6.16 km/sec.

The crust, in this area, is found to be complicated, based on the teleseismic and local earthquake data. P-waves from teleseismic earthquakes show travel time deviations as large as 0.4 sec, which may be related to the fractured nature of the crust. The existence of an inter-crustal discontinuity is suggested by seismograms from a local earthquake. The observed P-wave refractions are consistent with a horizon at 20 km depth, which has a dip of 4.5 deg, and a P-wave velocity of 6.6 km/sec.

## Contents

### Chapter

1	INTRODUCTION.....	1
1.1	The Purpose of this Work.....	4
2	STATIONS AND INSTRUMENTATION.....	5
2.1	Stations.....	5
2.2	Instrumentation.....	9
3	CALIBRATION OF THE INSTRUMENTATION.....	12
3.1	Theoretical Background.....	12
3.2	Obtaining the Instrument Response.....	15
3.2.1	Reducing Random Noise.....	16
3.3	Inversion for the Calibration Function.....	21
4	EVENT DETECTION.....	23
4.1	A Review of Signal Detection Techniques.....	24
4.1.1	Time Domain Techniques.....	24
4.1.2	Frequency Domain Techniques.....	26
4.1.3	Pattern Recognition Techniques.....	27
4.1.4	Optimum Detection Technique.....	28
4.2	An Overview of the Theory for Three-Component Event Detection.....	28
4.3	Development of a Three-Component Detection Algorithm.....	30
4.3.1	Estimating the Covariance Matrix in Real Time.....	30
4.3.2	Estimating the Maximum Eigenvalue in Real Time.....	32
4.3.3	Estimation the Background Noise Power..	33

4.3.4	Detection Decision Making.....	34
4.3.5	Event Discrimination.....	35
4.4	Tuning the Detector.....	37
4.4.1	Pre-Detection Parameters.....	37
4.4.2	Detection Parameters.....	38
4.4.3	Post-Detection Parameters.....	42
4.5	Test Results.....	42
5	SEISMOGRAM PROCESSING AND INTERPRETATION.....	46
5.1	Selecting the Data.....	46
5.2	Filtering.....	48
5.2.1	Frequency Filtering.....	48
5.2.2	Deconvolution Filtering.....	49
5.3	Teleseismic Earthquake Analysis.....	51
5.3.1	Cross-Correlation.....	53
5.3.2	Location.....	55
5.4	Regional Earthquake Analysis.....	58
5.4.1	Location.....	58
5.4.2	Regional Magnitude Calculation.....	62
5.4.3	Spectral Studies for Source Parameters.....	65
6	STUDY OF SEISMIC NOISE IN THE SASKATOON AREA.....	69
6.1	The Sources and Character of Short-Period Seismic Noise.....	69
6.2	Noise Data and Spectrum Calculation Methodology.....	72
6.3	Comparison of the Average Year Noise Between the Stations in the USSN.....	74

6.3.1	Frequencies Between 0.2 Hz to 0.7 Hz.....	74
6.3.2	The Short-Period Seismic Signal Band: 0.7 Hz to 3.5 Hz.....	80
6.3.3	Noise from 3.5 Hz to 10 Hz.....	81
6.4	Diurnal Variations in Noise Levels.....	82
6.5	Seasonal Variations in Noise.....	85
6.6	An Example of the Effect of Wind on Seismic Noise.....	88
6.7	Magnitude Threshold: a Comparison of Station Data Quality.....	94
6.7.1	Calculating the Threshold Functions....	94
6.7.2	USSN Station's Magnitude Thresholds....	96
6.7.3	USSN Station's Magnitude Dynamic Ranges.....	101
6.8	Noise Study Summary.....	103
7	STUDY OF THE CRUST USING EARTHQUAKES.....	105
7.1	Devising a Crustal Model for the Saskatoon Area.....	105
7.2	Regional Earthquake Travel Time Function.....	111
7.3	Relative Travel Time Anomalies of Teleseismic Earthquakes.....	118
7.3.1	The Teleseismic Data.....	119
7.3.2	Method of Analysis.....	121
7.3.3	Teleseismic Azimuthal and Slowness Anomalies.....	122

7.3.4	Teleseismic Relative Travel Time	
	Residual Patterns.....	124
7.3.5	Station Time Corrections.....	129
7.3.6	Discussion.....	132
7.4	The Kuroki Earthquake: A Unique Opportunity	
	to Study P- and S-Wave Refractions From a	
	Discontinuity Within the Crust.....	135
7.4.1	Epicentre Location.....	137
7.4.2	Focal Depth.....	137
	7.4.2.1 Isoleismal Survey.....	139
	7.4.2.2 Surface Waves.....	139
	7.4.2.3 Seismogram Modeling.....	141
	7.4.2.4 Geology.....	143
	7.4.2.5 Focal Depth Conclusion.....	143
7.4.3	Phase Velocities Comparison.....	144
7.4.4	Origin Time.....	146
7.4.5	Depth to $P_1$ Refractor.....	147
7.4.6	Suggestion for the Presence of the	
	Riel Discontinuity.....	149
7.5	A New Crustal Model for the Saskatoon Area....	152
8	CONCLUSIONS.....	155
	REFERENCES.....	157
	APPENDIX A: Theory for Three-Component Event	
	Detection.....	171
	APPENDIX B: Computer Programs.....	176

5.7	Spectral Analysis for Source Parameters.....	67
6.1	Average year noise for the USSN vertical seismometers.....	75
6.2	Average year noise for the BRG station.....	76
6.3	Average year standard deviation of the noise for the USSN vertical seismometers.....	77
6.4	Average year standard deviation of the noise for the BRG seismometers.....	78
6.5	PSD ratios to BRG vertical for the year noise.....	79
6.6	Ratio of day time PSD to year long PSD.....	83
6.7	Ratio of night time PSD to year long PSD.....	84
6.8	Ratio of summer time PSD to year long PSD.....	86
6.9	Ratio of winter time PSD to year long PSD.....	87
6.10	BRG vertical PSD during a windy day.....	89
6.11	BRG north component PSD during a windy day.....	90
6.12	BRG east component PSD during a windy day.....	91
6.13	BLK PSD during a windy day.....	92
6.14	Day time magnitude threshold.....	97
6.15	Night time magnitude threshold.....	98
6.16	Summer time magnitude threshold.....	99
6.17	Winter time magnitude threshold.....	100
6.18	Maximum magnitude capability of the USSN.....	102
6.19	Maps showing magnitude threshold and maximum event size.....	104
7.1	Generalized geological section and P-wave velocity model.....	107
7.2	Depth of Precambrian basement below surface.....	108

7.3	East to west crustal profile of southern Saskatchewan.....	110
7.4	BRG seismograms from a regional earthquake.....	112
7.5a	Regional event magnitude.....	113
7.5b	$P_n$ and $L_g$ phase distribution.....	113
7.5c	$P_g$ phase distribution.....	113
7.5d	$S_n$ phase distribution.....	113
7.6	Travel time table for regional earthquakes.....	115
7.7	Location map of teleseismic earthquakes.....	120
7.8	Array diagram showing mis-located earthquakes.....	123
7.9	Map showing an example of the mis-location of an earthquake.....	125
7.10	Relative travel time residuals for the teleseismic data.....	126
7.11	Array diagram after application of azimuth variable travel time corrections.....	130
7.12	Array diagram after application of azimuth and slowness variable travel time corrections.....	131
7.13	Map showing the mis-location of the earthquake in figure 7.9 after the station corrections.....	133
7.14	The vertical USSN seismograms from the Kuroki earthquake.....	136
7.15	Isoseismal map from the Kuroki earthquake.....	138
7.16	Low velocity $R_g$ from the Kuroki earthquake.....	140
7.17	Seismogram modeling.....	142

7.18 Comparison of phase arrival times from the Kuroki earthquake to times suggested by the GSC model.....	145
7.19 P phase arrival assuming a flat $P_1$ discontinuity..	150
7.20 P phase arrivals assuming a 4.5 deg dip on the Riel A discontinuity.....	153
7.21 Crustal model for the Saskatoon area.....	154

List of Tables

## TABLES

2.1	University of Saskatchewan seismograph network.....	6
5.1	Natural earthquakes in Saskatchewan.....	60
5.2	Mining induced earthquakes in Saskatchewan.....	61
5.3	Nuttli magnitude estimate comparison.....	64
7.1	Comparison of crustal phase velocities.....	116
7.2a	Average relative travel time residuals for the azimuthal groups.....	128
7.2b	Average relative travel time residuals for group 5.....	128
7.3	Origin time analysis using $P_n$ .....	148

## CHAPTER 1

INTRODUCTION

The University of Saskatchewan Seismograph Network (USSN) tripartite array was established to provide information on natural and induced seismic events in the province. Low-level shallow seismicity, scattered across southern Saskatchewan, is also observed in the north west Dakotas, and north east Montana. To date, there have been thirty-eight induced earthquakes and thirteen natural earthquakes in Saskatchewan. The largest earthquake, in 1909, had an estimated magnitude of 5.5 (Horner and Hasegawa, 1978).

The cause for earthquakes in Saskatchewan is not well understood. The area is tectonically stable. Part of the reason for a lack of knowledge of the phenomenon is the sparse seismograph instrumentation coverage of the region. Prior to 1965, the Canadian Seismograph Network (CSN) was incapable of locating events in the province lower than about magnitude 4. This former coverage is apparent in the history of the seismicity in the area. Only three earthquakes were recorded before 1968. Although there were probably more events in the past, they were not recorded. In recent years, seismograph instrumentation has provided essential data for investigating Saskatchewan earthquakes.

Horner et al. (1973) investigated one of the first

natural events to be recorded by a number of stations in the CSN. They suggested a strike-slip mechanism for a 1972 event based on surface wave amplitude radiation patterns. The recordings of the body waves were too small to facilitate any interpretation of the focal mechanism. Gendzwill et al. (1982) used instrumental and isoseismal data to study a series of induced events at the Cory Potash Mine near Saskatoon. The depths for these events could be confined to an area above the mine workings, but the focal mechanism was in question due to poor azimuthal coverage. In another publication, Gendzwill (1984) applied spectral analysis theory to the digital recordings to show that the events had large rupture surfaces, and postulated that the mechanism must be one of horizontal shear failure (although this may now be questionable; Gendzwill, personal communication). A completely different sequence of seismic events occurred when another potash mine in the province was flooded in 1987. Many seismic events were noticed in the area; their character was consistent with a ongoing collapse around the periphery of the mine workings (Gendzwill and Prugger, 1990). The largest event in the sequence - with a magnitude 2.7 - was about two minutes in duration, and appeared to consist of many overlapping impulsive shocks.

A key publication related to seismicity in southern Saskatchewan is given by Horner and Hasegawa (1978) who discuss the seismotectonics of the area. They found that there is an apparent spatial correlation between known

earthquakes in the region and structures found in both the Precambrian basement and in the overlying sediments. The accuracy of locations of some of the earlier events was crude, resulting in speculative analysis. Now, with the addition of the USSN short-period instruments and other CSN stations in southern Saskatchewan, events as small as magnitude 2.3 have been located.

The first station in the USSN array was established in 1979. Since then, two more stations have been added, forming a triangular array with each leg approximately forty-five kilometers long. In 1987, an analogue-to-digital converter was added to the hardware. Digital data are essential for understanding the recorded seismic events. Earthquakes cannot be characterized by their locations and magnitudes alone. Other characteristic parameters can be derived from detailed analysis of their digital seismograms.

Digital seismogram analysis requires quality data. Prior to 1990, data collection and analysis methods available for the USSN were crude. Everyday, event detections were performed manually and the only digital analysis available was via a computer package which could plot digital seismograms onto paper at any desired time- or amplitude-scale. Seismic events could not be analyzed thoroughly because the tools were unavailable.

## 1.1 The Purpose of this Work

The main purpose of this work has been the development of an automatic seismic data monitoring algorithm and interactive computer analysis packages which can be used to analyze seismograms. In this thesis, I describe these programs which were designed for use on the USSN. Thorough descriptions of the instrumentation, monitoring and analysis packages are given in Chapters 2 to 5. The standard parameters necessary for describing a recorded earthquake can be derived quickly using the computer software. Chapter 6 examines the recording ability of the USSN using a study of the ambient seismic earth noise and results from calibration experiments. Chapter 7 investigates the crustal structure using recorded earthquake data for the purpose of developing a crustal model necessary for proper earthquake location.

## CHAPTER 2

STATIONS AND INSTRUMENTATION

A crucial component of any seismological study is the instrumentation. One must understand both the capabilities and limitations of the seismograph system. This chapter gives a description of the stations in the network and the instrumentation. Pertinent information on the equipment is shown in Table 2.1.

## 2.1 Stations

Locations of the three short-period stations in the USSN, named Blackstrap (BLK), Bergheim (BRG), and Cominco (COM), are shown on Figure 2.1. BRG, and BLK are both surface sites, whereas COM is located in a main access tunnel in the Cominco potash mine at a depth of about one kilometer. Several locations for the surface sites were tested to decide on the final positions for the stations. The locations are situated away from any significant cultural noise or traffic (see section 6.1 for a discussion on cultural noise). BRG is the closest station to Saskatoon, at about 15 Km from the edge of the city. Approximately a week of monitoring at each of the experimental sites showed that the present positions had the lowest relative noise background compared to other locations

University of Saskatchewan Seismograph Network

Array

Station Abbreviation	Latitude (north)	Longitude (west)	Elevation (m)	Type of site
BLK	51°49'37"	106°17'42"	541	Open (vert)
BRG	52°11'08"	106°23'53"	594	Vault (3comp)
COM	52°00'29"	107°05'31"	-512.5	Mine (vert)

Instrumentation

- Seismometers — Mark Products Inc. L-4C.
- Resonant frequency = 1.0 Hz.
  - Electrodynamic constant = 283 V/m/sec.
  - Open circuit damping = 0.266 of critical damping.
- Amplifiers — Sprengnether Instruments Inc.
- Gain = 78 dB
  - Range of gain settings possible:  
60 dB to 120 dB in 6 dB increments.
  - Anti-alias filter low-cut = 5.0 Hz
  - Anti-alias roll-off = 12 dB/octave
- Voltage Controlled Oscillators and Discriminators
- Sprengnether Instruments Inc.
- Digitization and Event Detection/Analysis
- DIGITAL 3200 VAX-station
  - Digitization rate = 20 Hz (adjustable)

Table 2.1. University of Saskatchewan seismograph network parameters.

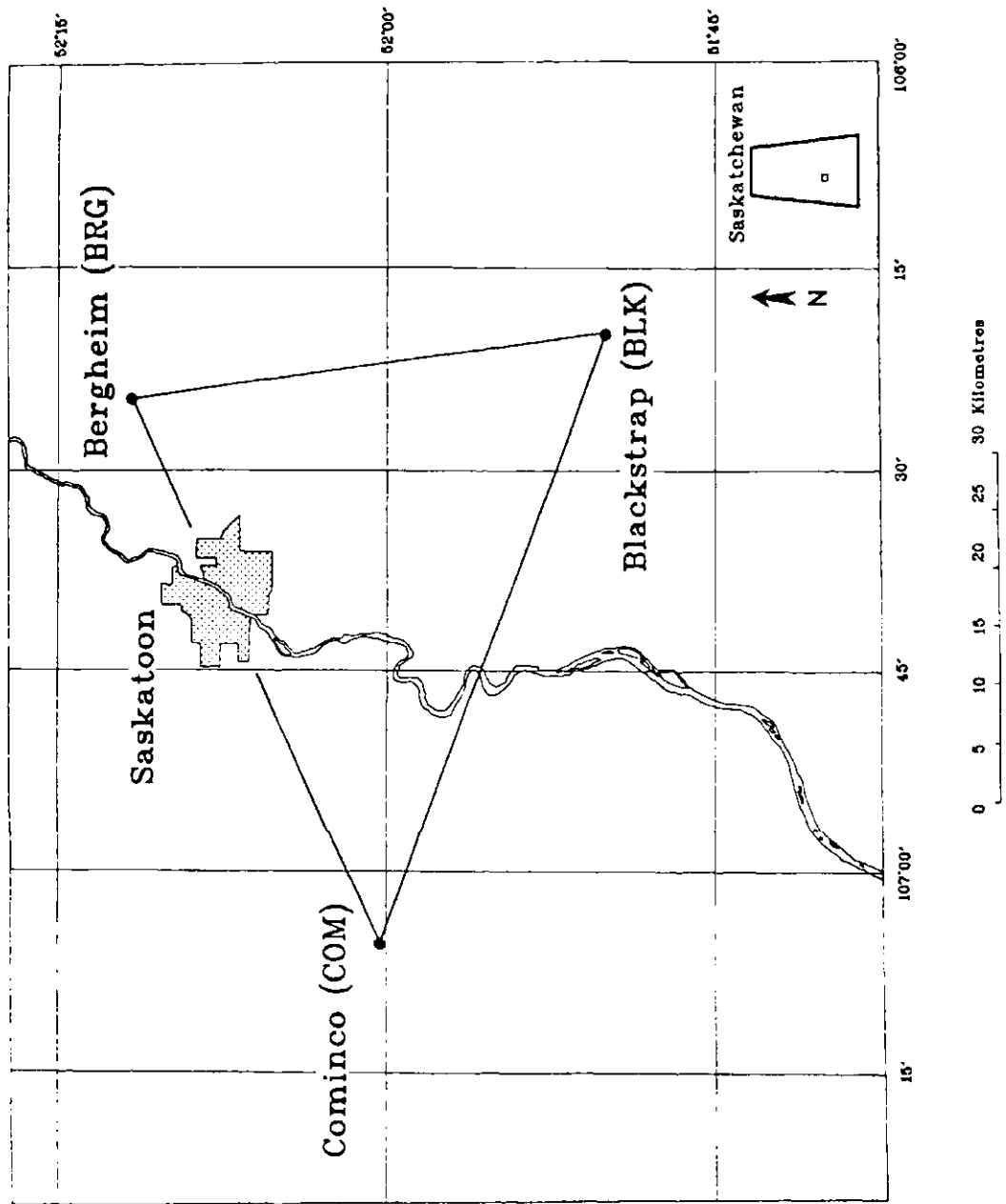


Figure 2.1.1. Map of the University of Saskatchewan seismograph array.

tested.

All of the stations in the USSN use Mark Products L-4C geophones, which have an undamped peak response at 1 Hz (Mark Products, 1992). BRG is the only site with two orthogonal horizontal seismometers. All three seismometers at BRG are equipped with calibration coils.

The BRG station is a state-of-the-art seismic vault which offers a stable low noise environment. The vault is both temperature and humidity controlled and is flush with the side of a hill to reduce wind noise. The top few meters of unconsolidated glacial till and sand were stripped away so that a concrete pier could rest directly on hard packed sand.

BLK is the noisiest station in the array because it is an earth site: the single vertical geophone is buried in the ground at about 1 m depth in the middle of a farmer's field. Both surface locations are situated over about 100 m of glacial till.

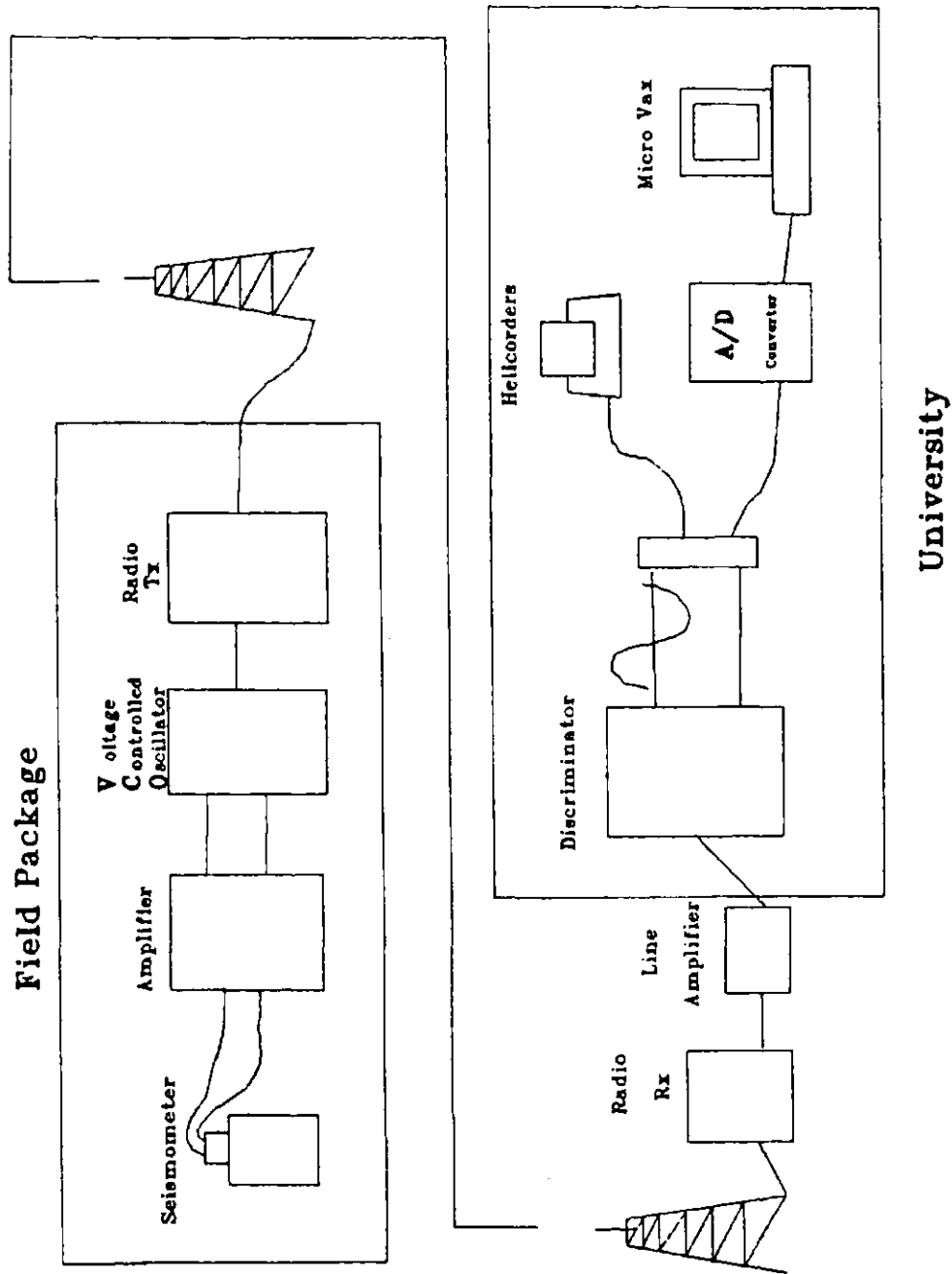
The vertical component geophone at the COM site is clamped to the roof of the tunnel with a metal bracket which is bolted into the rock. The station is situated close to a power transformer which has 13 800 V of 60 Hz power passing through it. The line often experiences short power bursts that cause sharp spikes to appear on the COM seismograms. The COM site is the quietest station in the USSN as the location does not have a lot of traffic.

## 2.2 Instrumentation

Figure 2.2 depicts the instrumentation. At each site, the output from the seismometers is amplified by 78 dB gain and anti-alias filtered with a low cut of 5 Hz, and a fall off of about 12 dB per octave. Voltage controlled oscillators (VCOs) convert the seismic data to FM signals, which are transferred at a dedicated carrier frequency back to the University of Saskatchewan department of Geological Science's facility. The VCO has a peak to peak capacity of 5 V, which limits the dynamic range of the system to about 60 dB. The largest possible particle velocity at 1 Hz that can be recorded without distortion at 78 dB gain is about 4.0  $\mu\text{m}/\text{sec}$ .

The FM signals received at the department are converted back to voltages and digitized at 20 Hz. DIGITAL software (VAXLab) on a DIGITAL 3200 VAX-station is used for the real time digitizing. The multiplexed data files are continuously saved in both 15 min and 1 hr lengths, and are available for 24 hrs on the hard disk. An array seismic event detector screens the 24 hrs of data once daily in a batch mode, and saves triggered time segments of data to permanent files. Later post-processing can provide spectra, locations of events, and magnitudes for local and regional distances.

Based on past experience, the array can record any earthquakes in southern Saskatchewan of magnitude greater



University

Figure 2.2. USSN instrumentation.

than about 2.3, any events in the Prairie Provinces over 3.0, and events in North America over about 4.5. Relationships of perceptible and maximum magnitude as a function of distance will be derived later in the chapter on the seismic noise analysis.

## CHAPTER 3

CALIBRATION OF THE INSTRUMENTATION

Calibration is an important processing component in seismic analysis. An instrument response function is needed for calibration. This function relates voltage outputs from the instrument system to actual variations in ground particle motions (in units of  $\mu\text{m}/\text{sec}$  for example). Calibrated seismograms make quantitative evaluation of the seismic data possible. Furthermore, on short period systems, calibration is particularly useful for timing phase arrivals since the process recovers some wave frequencies that have very small amplitudes on the uncalibrated traces. As a result, the enhanced seismogram greatly improves phase timing accuracy. The instrument response function for the USSN instrumentation is obtained using standard procedures which were first discussed by Espinosa et al. (1962). Those procedures will be briefly discussed in this chapter along with a technique used to reduce the influence of random noise on the response function. The final portion of the chapter discusses how the instrument response function is used to calibrate the seismograms.

## 3.1 Theoretical background

The preferred technique for obtaining instrument

response is the "black box" approach (Willmore 1975). The seismometer instrumentation is modeled as a black box which transforms an impulsive input into a filtered output. Nothing needs to be known about the instrumentation; one only has to know the characteristics of the input and output signals. That makes the black box approach convenient because instrument constants are difficult to determine accurately.

The impulsive input is provided by calibration coils on the seismometers. A small current is introduced into the coils which lifts the seismometer mass (a step function). The current in the calibration coils is related to the step in the seismometer mass by

$$s(t) = (10^{-6})(T_s/T_c)(IG/M) \quad 3.1$$

where:  $s(t)$  is the step function ( $\mu\text{m}/\text{sec}^2$ ),

$T_s$  is the number of turns of wire in the seismometer coil,

$T_c$  is the number of turns in the calibration coil,

$I$  is the current through the calibration coil,

$G$  is the calibration constant of the seismometer (N/Amp),

$M$  is the mass of seismometer coil (kg).

Typical values for the above are tabulated below:

---


$$\begin{aligned} T_s &= 9900 \text{ turns,} \\ T_c &= 12, \\ I &= 0.067 \text{ mAmps,} \\ G &= 40.2 \times 10^{-5} \text{ N/Amp, and} \\ M &= 0.980 \text{ kg.} \end{aligned}$$


---

Entering the values into equation 3.1, gives a step function size of  $22.7 \mu\text{m}/\text{sec}^2$ . The USSN uses velocity seismometers so equation 3.1 must be integrated to obtain units of ground velocity. Then, at 1 Hz, the step function size is  $3.8 \mu\text{m}/\text{sec}$ .

The instrument response (h) is obtained by

$$h(t) = r(t) * s^{-1}(t), \quad 3.2$$

where:  $r(t)$  is the response seismogram to the calibration sequence and is recorded in volts.

This last equation is easier to implement in the frequency domain:

$$H(f) = R(f) / S(f) \quad 3.3.$$

The calibration function is obtained by inverting  $H(f)$

and inverse Fourier transforming  $H^{-1}(f)$  into the time domain to obtain  $h^{-1}(t)$ . The seismograms are calibrated by convolving  $h^{-1}(t)$  with the trace

$$c(t) = h^{-1}(t)*u(t), \quad 3.4$$

where:  $c(t)$  is the calibrated seismogram, and  
 $u(t)$  is the uncalibrated seismogram.

Note that

$$i(t) = h(t)*h^{-1}(t), \quad 3.5$$

where:  $i(t)$  is a delta function.

### 3.2 Obtaining the Instrument Response

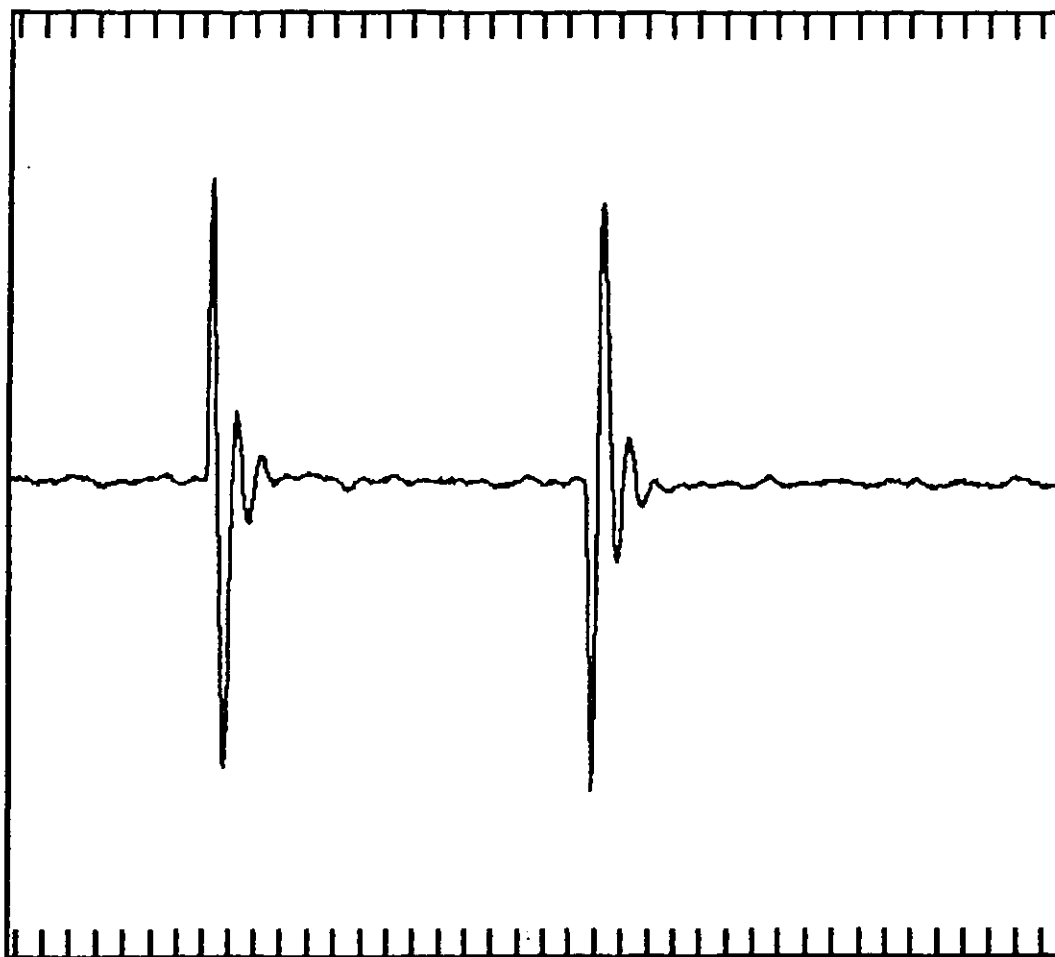
Responses can only be computed from BRG because the seismometers at the other two sites are not equipped with calibration coils. The instrumentation and gain settings are identical at all stations, so the instrument response calculated for BRG is assumed to be the same for the other stations. Aging of the electrical equipment could cause differences in response between the stations, but the effect is impossible to determine, so BRG's response is the best estimate available for the other stations. Only the BRG

seismograms are used for quantitative analysis of recorded earthquakes (ie., magnitude calculation).

Hardware at the BRG site introduces two steps into the calibration coils, twice daily at 12 hr time intervals. The calibration begins with a positive step in current, followed about 14 sec later by a step down in current back to the original state. Figure 3.1 shows a sequence of calibration pulses. I have developed an analysis program called US\_CALBR which uses the calibration pulses to obtain the frequency response function for the system. A typical example of a function is shown in figure 3.2.

### 3.2.1 Reducing Random Noise

The influence of random noise on a response function is apparent in figure 3.2, especially above frequencies of about 2.5 Hz. The program US\_CALBR reduces the random noise by stacking a number of calibration pulses together. US\_CALBR reads in the first pulse sequence and stores it as a reference. All the pulses read into the program are cross-correlated against the reference sequence to obtain the optimum phase alignment. The aligned series of calibration pulses are then averaged together to produce a stacked calibration pulse sequence. The noise is greatly reduced on the stacked calibration sequence (figure 3.3). The reduction in noise significantly decreases contamination in the frequency response function (figure 3.4).



(Seconds)

Figure 3.1. A calibration pulse sequence from the BRG station. The first pulse is a response to positive step in ground motion, and the second is a response to the step down back to the undisturbed state.

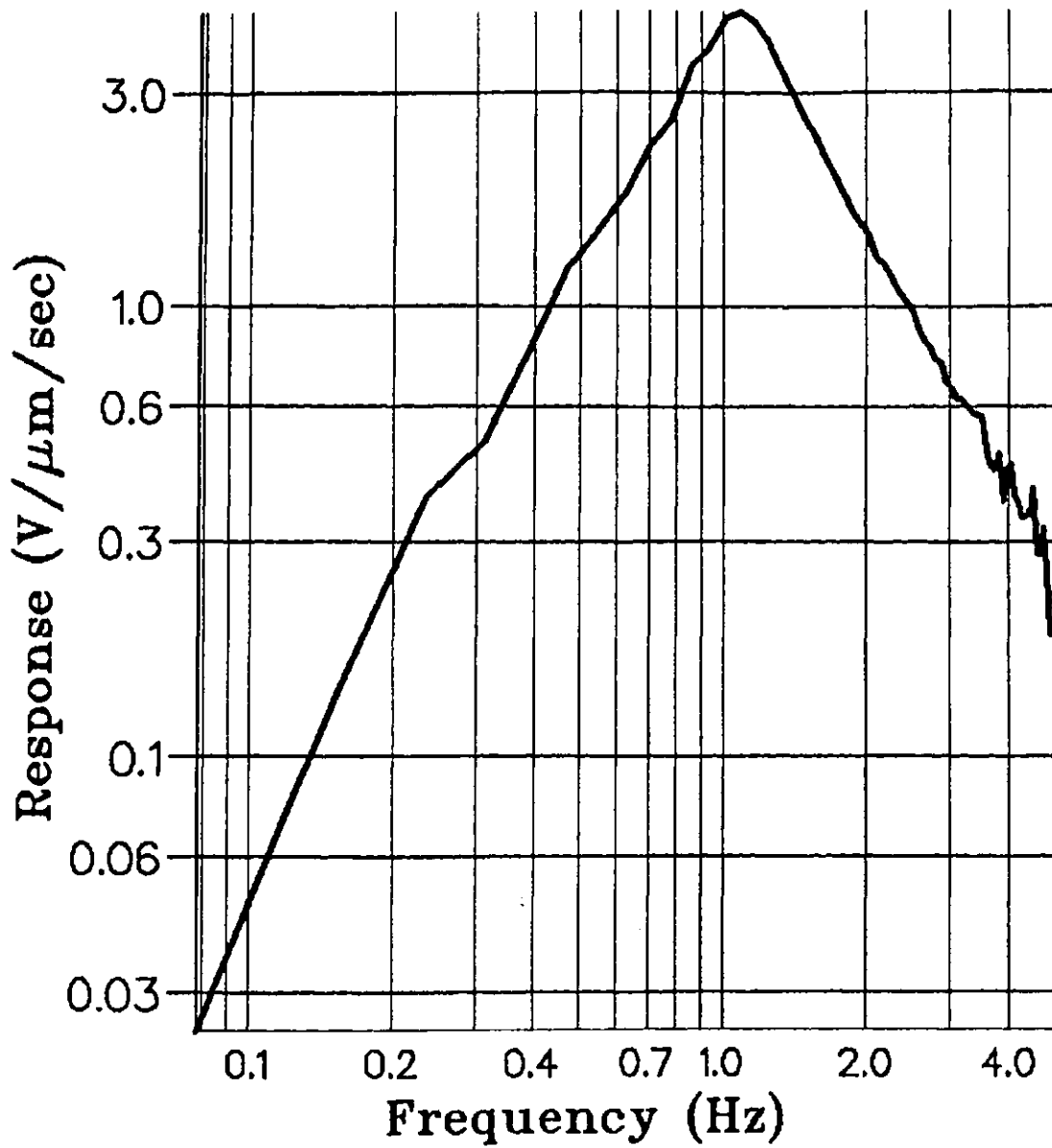
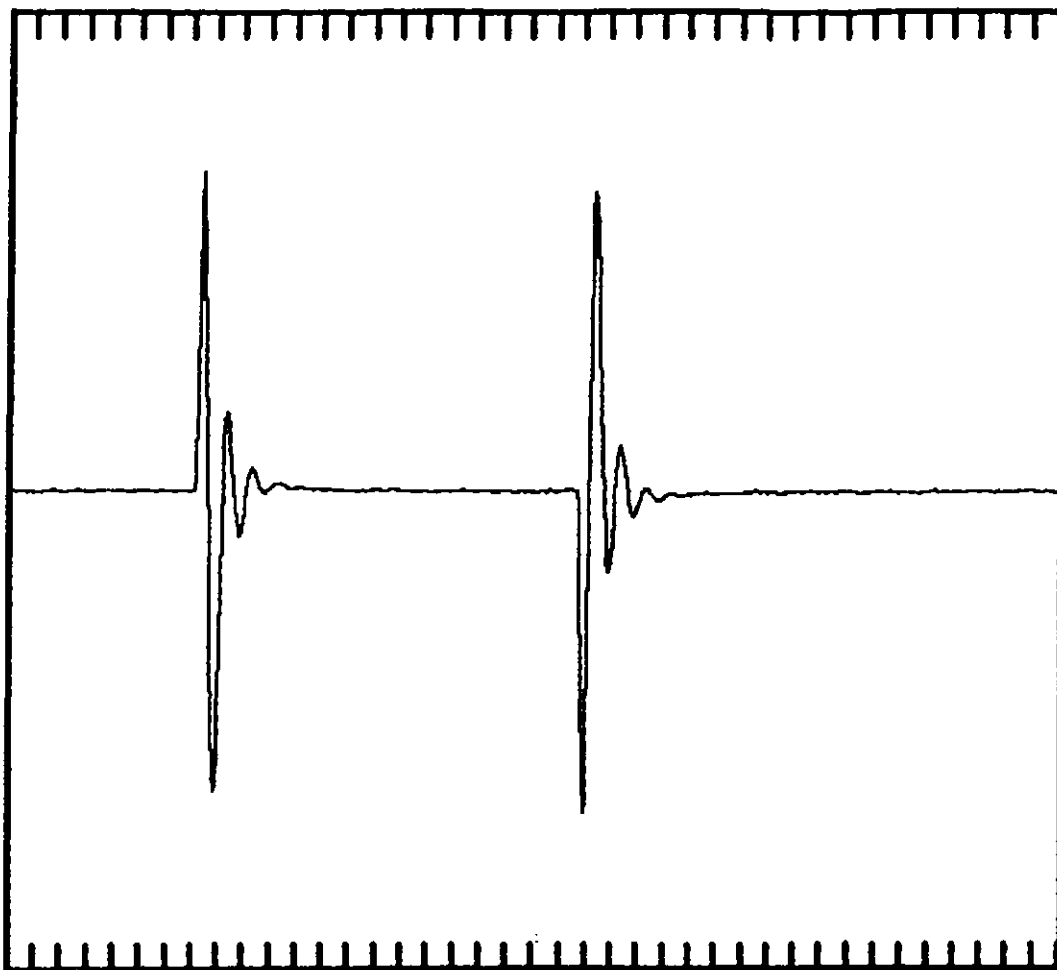


Figure 3.2. Frequency response from the calibration pulse sequence in figure 3.1.



(Seconds)

Figure 3.3. A stacked set of calibration pulses. Twenty-seven pulse sequences have been cross-correlated and averaged together to reduce the background noise.

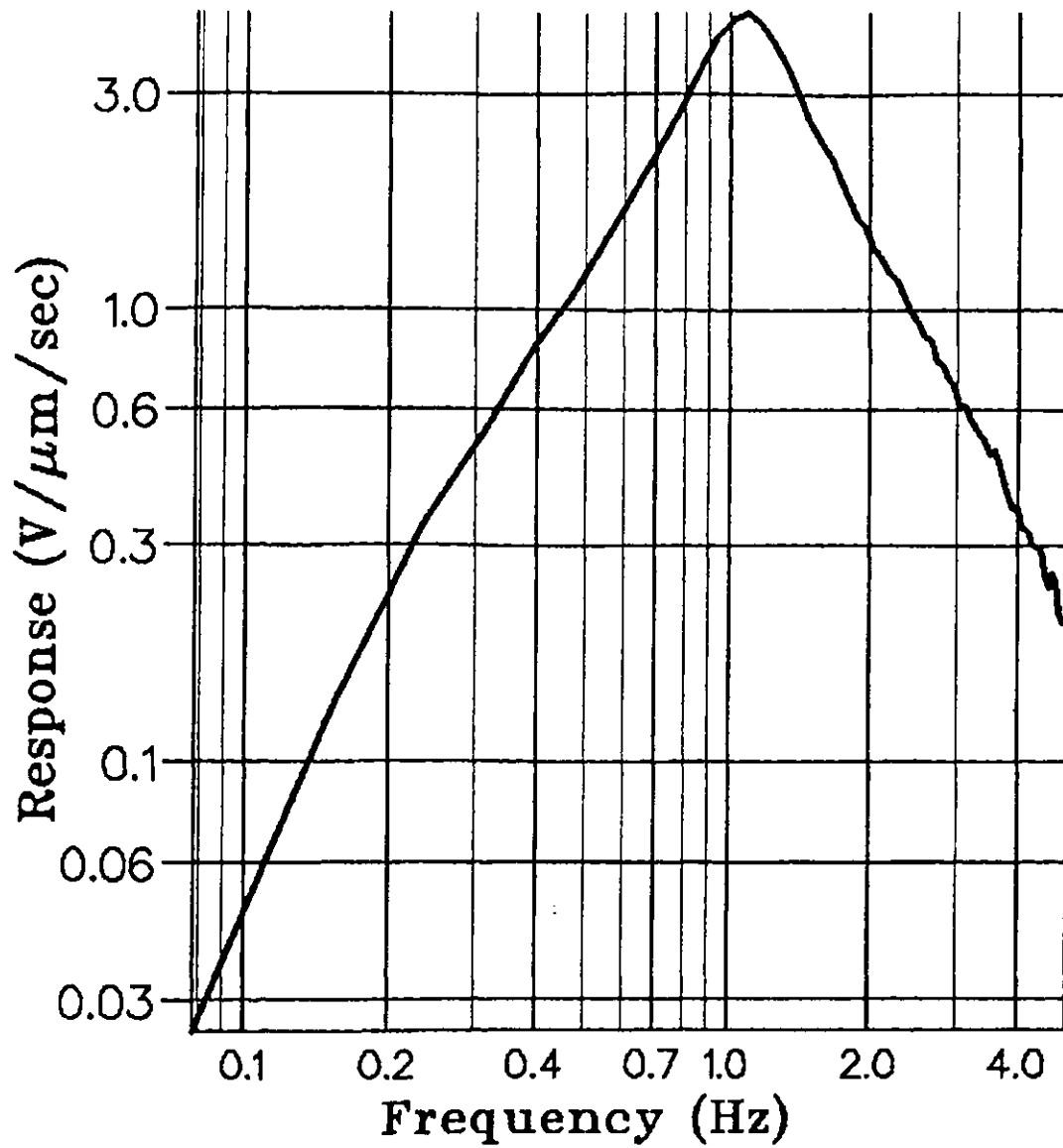


Figure 3.4. Frequency response derived from the stacked pulses in figure 3.3.

### 3.3 Inversion for the Calibration Function

The inversion of  $h(t)$  for the calibration function,  $h^{-1}(t)$ , is performed after a satisfactory response function is obtained. Small amplitudes in the response can make the inversion unstable so pre-whitening is required. Typically, a number of pre-whitening factors around about 0.15% are tested. The pre-whitening factors are evaluated by examining their effect on the time series of both the calibration functions and the delta functions (ie. the calibration function convolved with the instrument response to give  $i(t)$  in equation 3.5). The pre-whitening causes the delta function to take the form of a sinc function. The optimum pre-whitening is the value that gives the sharpest delta function with the least "ringing" in the calibration function (see figure 3.5).

The optimum calibration function is saved by US\_CALBR to a permanent data file. This file is used by other programs to deconvolve the instrument response from USSN seismograms. The inherent error in the function varies somewhat with frequency; the average value within the seismic signal band (0.7 Hz to 3.5 Hz) is about 4 percent. The deconvolution makes magnitude estimation possible and greatly improves first arrival and phase timing accuracy. The procedure is an essential component of the post detection processing discussed in chapter 5.

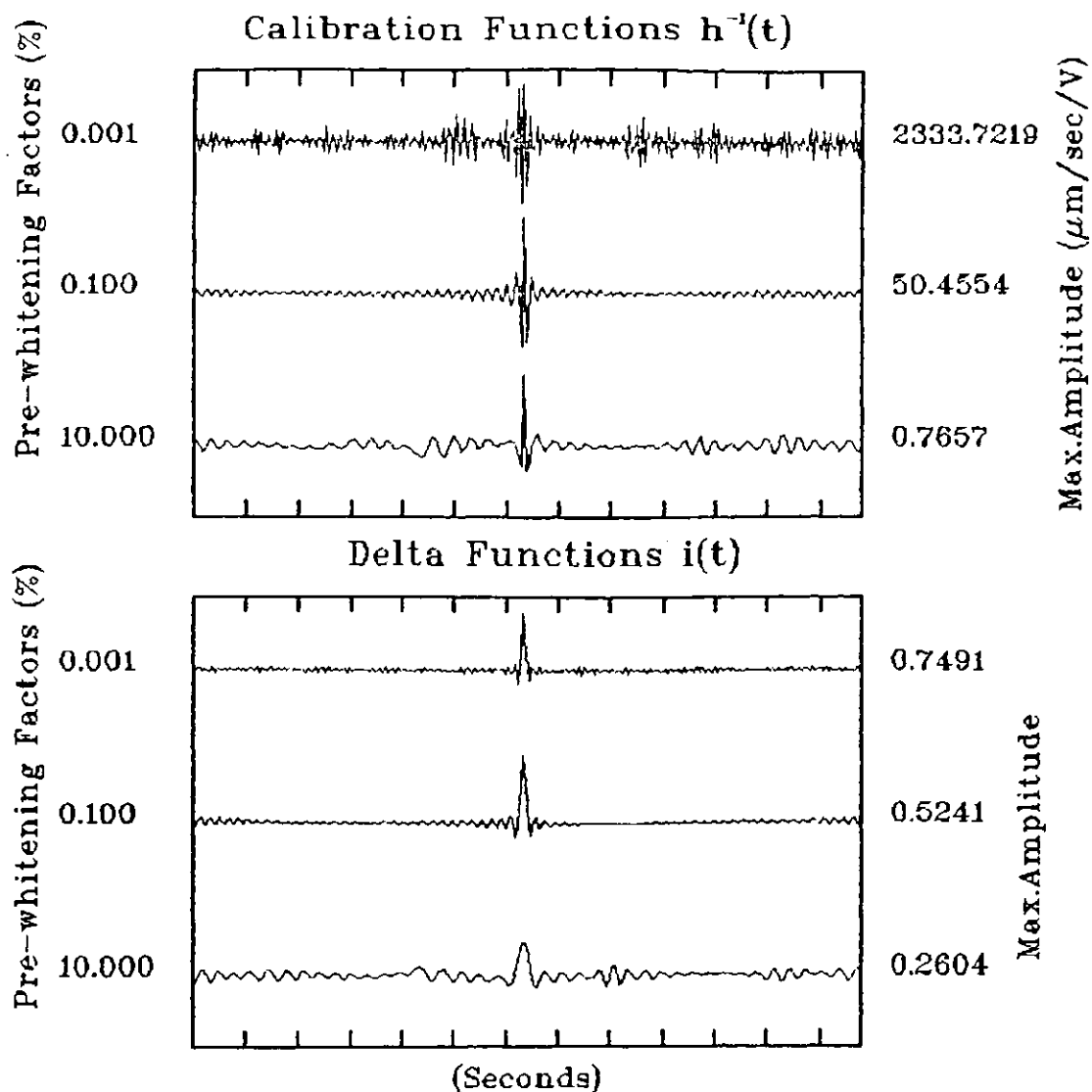


Figure 3.5. A set of calibration operators and delta functions used for the evaluation of pre-whitening factors. The optimum pre-whitening factors are in the range of 0.1%.

## CHAPTER 4

EVENT DETECTION

Automated event detection is a necessary component of any seismic monitoring program. Manually scanning chart records can be very time consuming and results in missed events. Also, for small institutions, human seismic interpreters are not available every day of the year. With modern, fast computers event detection algorithms can be quite sophisticated so that small events not apparent to human analysts may be detected.

Most event detectors operate only on the vertical component seismometer. A tri-axial (ie., three component) seismic event detection algorithm would perform better because all three orthogonal components of the incoming signals are used for detection. That should result in an improvement in the signal to noise ratio for seismic events. The event detector used on the USSN is an adoption of a tri-axial detector. Only the BRG station has tri-axial seismometers, so a modified version for one component monitoring has been developed for BLK and COM.

This chapter discusses the event detector that has been adopted for seismic monitoring in the USSN. In the literature there are many publications related to event detection, but all of the routines can be broken down into a few core designs. It is important to understand the basic

algorithms, so this chapter begins with a discussion on the background of event detection and the merits of three component detection. Next, a description of the algorithm in the USSN is given, followed by a performance evaluation after four months of continuous monitoring.

#### 4.1 A Review of Signal Detection Techniques

##### 4.1.1 Time Domain Techniques

The first discussion on detection theory was presented by Freiburger (1963). He suggested that for best detection, the data should be filtered for optimum signal to noise ratio (S/N) and a measure of the power should be used for deciding whether signals of interest are present. Blandford (1982) indicates that the first practical application of this theory was the short term/long term averaging technique (STA/LTA) applied to the Montana Large Aperture Seismic Array. The data from this array were first filtered by a digital recursive band pass filter which approximated the optimum filter frequency response specified by Freiburger (1963). The STA of these data used a window which was the length of the signals of interest. The LTA had a much larger window length which was used to estimate the noise power. If the STA exceeded the LTA by a certain ratio, a detection was declared. Blandford (1982) indicates that analysts were satisfied with the detector's ability to

notice weak signals. However, a systematic evaluation of the threshold of this detector, as compared to some optimum, was never made.

The Z detector (Swindell and Snell, 1977) is an improvement over the STA/LTA technique because it adapts to diurnal and seasonal changes in the seismic noise (Joswig, 1990). The Z detector continuously estimates the variance of the seismic noise, using the STAs and LTAs of the seismic data. Detection is declared when the STA exceeds a sum of the LTA and a multiple of the standard deviation of the noise. The Z detector essentially uses a variable detection threshold to hold the false alarm rate due to fluctuations in white Gaussian noise constant. Blandford (1982) indicates that this procedure is desirable in theory. However, most false alarms are not statistical but result from system failures, cultural noise, or true seismic events which are not of interest.

Allen (1978) formulated a detection algorithm for micro-earthquake arrays which uses post-detection logic to reduce non-statistical false alarms. Allen (1978) converts the seismic data into a characteristic function which depends on the time series of the seismic trace and its first derivative. This characteristic function tunes signal processing for optimum post-detection criteria (Joswig, 1990). Blandford (1982) indicates that Allen used no pre-filtering of the data, and therefore Allen's algorithm may only be able to detect weak signals if the system response

is close to the response of the optimum filter as formulated by Freiburger (1963). Blandford (1982) suggests that system responses are not ideal for detection, so pre-filtering is necessary. These characteristic function based algorithms have lower false alarm rates due to their post-detection logic (Joswig, 1990).

#### 4.1.2 Frequency Domain Techniques

Detection routines have been developed which do not operate in the time domain. An example is the Walsh detector developed by Goforth and Herrin (1980), which operates in the sequency domain. Sequency is a special form of frequency. Square waves are used in place of sinusoidal waves.

The Walsh spectra, used for detection, are calculated over short segments of the seismic data. The spectra are then band-passed to filter out microseisms, and weighted to whiten the noise. Each spectrum of sequency is summed, and the sum ( $M$ ) is used to update a histogram of the past 512 sums. The LTA is taken as the median value ( $M_{50}$ ) of this histogram, and the variance ( $\sigma^2$ ) is estimated as the difference between the 75% point ( $M_{75}$ ) and  $M_{50}$ . A detection is declared if  $M > M_{50} + \beta \sigma^2$ , where  $\beta$  is a constant. Blandford (1982) notes that this approach minimizes the inflation of the detection threshold caused by occasional small spikes in the data.

A detection routine which operates in the frequency domain was developed by Gledhill (1985). The Fourier spectra are calculated over windows and are divided into five equal spectral bands. Each spectrum is summed and this sum is compared to a band-trigger level. If a trigger in a spectral band is declared, an appropriate weight number is added to a spectral weight number. If the spectral weight number is large enough and continues for a pre-set length of time, a detection is declared. The weight numbers for the band levels are chosen to emphasis energy in particular bands, so that an optimum S/N is obtained. The band-trigger levels are determined by past band-levels and are continuously up-dated. Gledhill (1985) indicates that this algorithm performed well at fairly high S/N.

#### 4.1.3 Pattern Recognition Techniques

Entirely different types of detectors are the pattern recognition based algorithms. Both earthquakes and temporary noise signals are known to the detectors as defined patterns. The incoming data are converted into patterns and these are compared to the detector knowledge base (see Joswig, 1990, for a review). Short period systems may not perform well with pattern recognition based algorithms because of the lack of frequency bandwidth. Pattern based routines require a broader bandwidth system, especially for teleseismic earthquakes (Joswig, 1990).

#### 4.1.4 Optimum Detection Technique

Allen (1982) suggested that detection algorithms which operate in the frequency domain are very sensitive to signals which are buried in noise, but cannot pick phase arrivals as well as STA/LTA or characteristic function based algorithms. Unfortunately, time domain techniques do not detect seismic events as well as frequency domain techniques in moderate S/N. An algorithm which is both a good detector and phase timer would be useful.

#### 4.2 An Overview of the Theory for Three-Component Event Detection

Three-component detectors are rare in the literature; discussions have been given by Magotra et al. (1987, 1989), Roberts et al. (1989), and Ruud and Husebye (1992). The algorithms differ in the core designs, but in general, the three-component detectors provide better performance than their one-component counterparts, because of the inherent improvement in S/N. The work by Magotra et al. forms the basis for the following discussion.

Magotra et al. (1987) developed a detection algorithm which combines the two horizontal channels of a three-component station and searches for rapid increases of linearly polarized power. Noise generally has random

variations in polarization, while first arrivals from earthquakes exhibit high degrees of linear polarization. Therefore by monitoring the polarized power one can differentiate between noise and seismic events of interest. The algorithm continuously updates the covariance matrix, and calculates the maximum eigenvalue ( $\lambda_m$ ) for the two horizontal channels providing a measure of signal power present. An estimate of the noise power is obtained by recursively averaging past  $\lambda_m$  values to produce a smoothed maximum eigenvalue ( $\lambda_{sm}$ ). A detection is declared when  $\lambda_m > (\alpha)(\lambda_{sm})$ , where  $\alpha$  is a constant. When a detection occurs, the azimuth of the arrival is estimated using the eigenvectors corresponding to the maximum eigenvalues. The algorithm then searches for a rapid change in polarization of 90 deg indicating an Lg (Love wave) arrival. The time difference between the P (P-wave) and Lg arrivals is used to obtain the distance to the event. The technique is attractive because S/N is improved by using two horizontal channels.

Magotra et al. (1989) improved their algorithm to monitor all three orthogonal components of the seismic data. Such an algorithm should have a better detection threshold because the S/N is improved. A detailed discussion on the theory can be found in Appendix A.

### 4.3 Development of a Three Component Detection Algorithm

This section will show how the three component detector theory is applied to the design of the algorithm for real time operation. Modifications to the design of the algorithm are also presented. The scheme has been simplified for vertical one component monitoring. These detectors are used for BLK and COM, while the three component scheme is used on BRG. The three stations are combined to produce an array detector.

#### 4.3.1 Estimating the Covariance Matrix in Real Time

Estimating the covariance matrices is the most difficult element of this detection scheme because they must be estimated in real time. Magotra et al. (1986) compared two variance estimation schemes: one is a simple running average of the squared data, and the other is:

$$s^2(m) = \beta s^2(m-1) + (1-\beta)x^2(m) \quad 4.1,$$

where:  $s^2$  is the estimated variance,  
 $x(m)$  is the current data value,  
 $m$  is the sample number,  
 $\beta$  is a constant.

One advantage of equation 4.1 is that this recursive

equation is easy to calculate and requires less computation time and space than a running average. Magotra et al. (1986) found that equation 4.1 produces more accurate estimates of the variance, and the estimates are more stable than those obtained from a running average.

In the time domain, the impulse response for an equation in the form of:

$$y(t) = \beta y(t-1) + (1-\beta)x(t) \quad 4.2,$$

is

$$h(t) = (1-\beta)(\beta^t) \quad 4.3.$$

Assuming that  $-(1-\beta)$  is approximately equal to the natural log of  $\beta$ , for  $\beta$  close to unity, equation 4.3 can be approximated as

$$h(t) = (1/\tau) \exp(-t/\tau) \quad 4.4,$$

where:  $\tau$  is a time constant.

When the impulse response (eq. 4.4) is convolved with a time series one realizes that equation 4.1 is an exponentially weighted sum of past data values and has a time constant  $\tau$  which is equal to  $1/1-\beta$ . For a  $\beta$  of 0.90, the time constant ( $\tau$ ) is 10 samples, and for a  $\beta$  of 0.98,  $\tau$  is equal to 50

samples. Larger time constants use more past data values to calculate a sum of the data. In the STA/LTA schemes the STA window approximates the length of the first arrival wavelets. In equation 4.1,  $\tau$  controls the averaging length which is determined by  $\beta$ .

Several advantages result from equation 4.1 as compared to a running average. If a larger window length is desired,  $\beta$  can be altered to meet the requirement. The impulse response (eq. 4.3) implies that equation 4.1 is very sensitive to present data values (they are weighted the most in the exponential sum). This is desirable for signal detection because the recursive equation is tuned to sense rapid increases in power and, therefore, should be a good phase detector.

#### 4.3.2 Estimating the Maximum Eigenvalue in Real Time

Following determination of the covariance matrix, the maximum eigenvalue must be estimated for the three component detector. Magotra et al. (1989) explicitly calculate the maximum eigenvalue. For the USSN detector, the value is approximated using the power method, which is a quick and accurate estimation procedure for determining the maximum eigenvalue and its corresponding vector (Anton, 1977). One must first estimate an eigenvector ( $u_{est}$ ), then

$$[u_{\text{new}}] = [C][u_{\text{est}}] \quad 4.5,$$

where:  $[\ ]$  implies a matrix.

provides a new estimate of the eigenvector, where  $C$  is covariance matrix. The estimate of the maximum eigenvalue  $\lambda_m$  is

$$\lambda_m = [u_{\text{new}}] \cdot [C][u_{\text{new}}] / [u_{\text{new}}] \cdot [u_{\text{new}}] \quad 4.6,$$

where: dots imply dot products.

Generally, for test data sets, the  $\lambda_m$  for the covariance matrices was estimated with a error of 0.15% after only one iteration. The reason for this accuracy is that the estimated eigenvector for the past time sample is used as the new estimate. These eigenvector magnitudes are low-pass filtered versions of the actual values, so they change slowly and consequently make this estimation possible. The real time performance is improved using this technique because fewer calculations are required.

#### 4.3.3 Estimating the Background Noise Power

For signal detection, one must compare the present  $\lambda_m$  to a measure of the noise power. For this scheme, the noise power is estimated by applying equation 4.1 to past maximum

eigenvalues as Magotra et al. (1989) did in their detection scheme:

$$\hat{E}_{sm}(m) = \beta \hat{E}_{sm}(m-1) + (1-\beta) \hat{E}_m(m-D) \quad 4.7,$$

where:  $\hat{E}_{sm}$  is a smoothed eigenvalue,  
 $D$  is the sample delay between the present sample and the sample used by the equation.

The one component detectors use the same equation for estimating their noise power.

#### 4.3.4 Detection Decision Making

With an estimate of the signal power (eq. 4.1) and noise power (eq. 4.7), a detection decision can be made by using

$$\hat{E}_m \geq \alpha \hat{E}_{sm} \quad 4.8.$$

Theoretically,  $\alpha$  could be set to unity because this algorithm should detect strongly linear, polarized signals in any amount of noise. Tests on synthetic data in noise with S/N being less than unity indicated that detection in an automated mode would be difficult. This is probably due to poor estimation of the covariance matrices in high S/N using the recursive technique. When equation 4.8 is found

to be true, a trigger for the station is declared and an event flag is turned on.

#### 4.3.5 Event Discrimination

A flow chart illustrating the processes in array seismic monitoring is shown in figure 4.1. The Monitoring Mode (MM) is a process that operates continuously and decides whether any station in the array has an event flag. A flag on one station does not necessarily imply that a seismic event has been detected. The array detection algorithm must use some post-detection processing to discriminate against noise signals.

The post-processing has two requirements: minimum event duration (MED), and maximum array moveout time (AMT). The minimum event duration is a requirement tested for each station. The event flag for a station must stay on for some minimum time period, otherwise a false alarm is declared (figure 4.1). Once the minimum duration is met, a channel detection flag is declared. This minimum event duration requirement discriminates against power and lightning spikes and short duration cultural noises.

The maximum array moveout time is a parameter tested for the entire seismic array. If several channel detection flags have occurred, the trigger times are used to calculate the apparent slowness of the event across the array in units of sec/km. A true event is declared only if the triggers

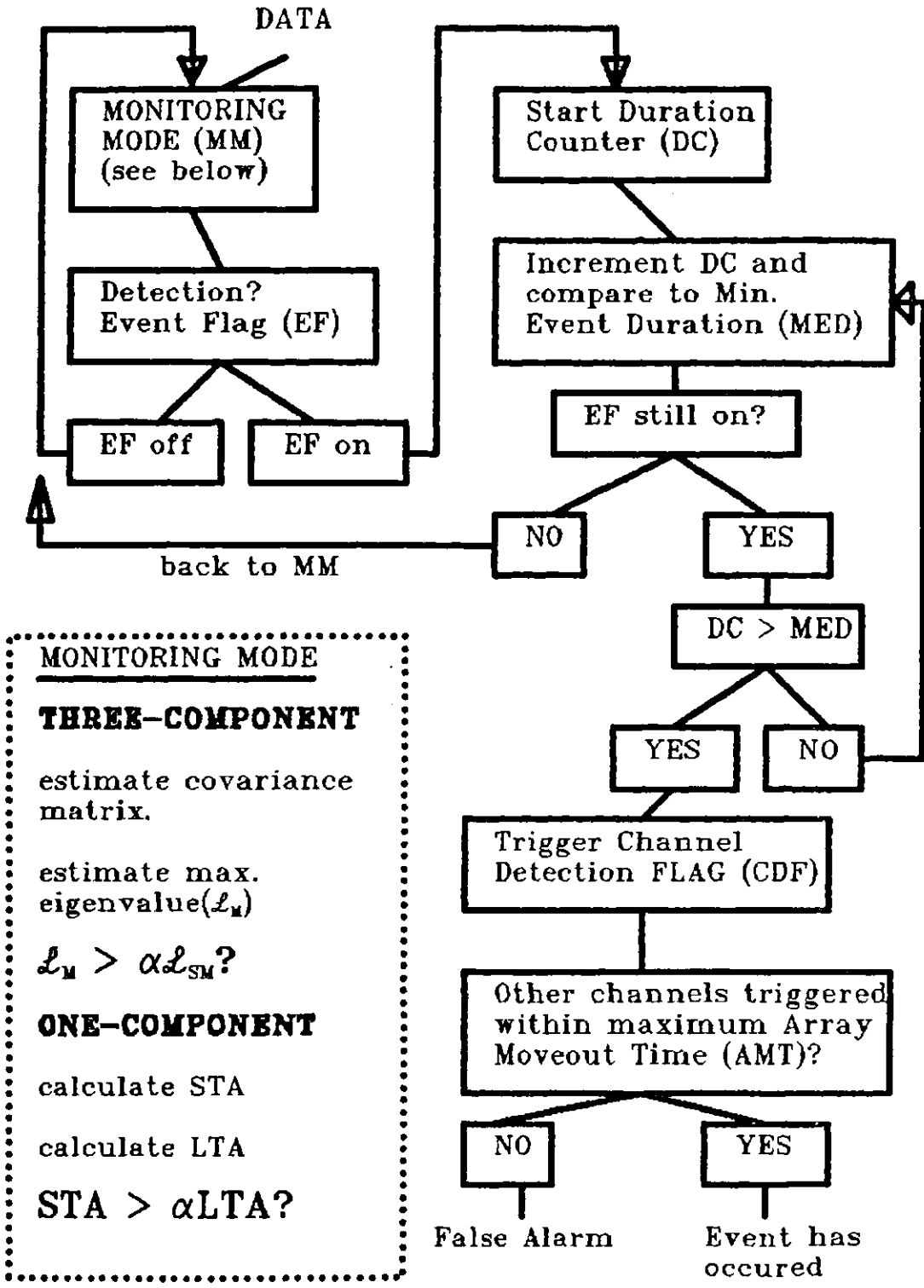


Figure 4.1. Flow chart of the array detector.

have all occurred within the maximum allowable apparent slowness (figure 4.1). This is a powerful method for reducing false alarms because the entire array is used for event discrimination.

#### 4.4 Tuning the Detector

The detection algorithm requires a number of parameters which must be tuned for optimum performance. The parameters can be divided into three classes: pre-detection, detection, and post-detection. The best performance level would have the lowest number of false alarms and missed events and the most accurate arrival times. The detectability of the algorithm is affected by how large the ratio  $\epsilon_m/\epsilon_{sm}$  (eq. 4.8) becomes at the arrival of an event. A large ratio above the background level makes the event much more detectable. This section shows how the parameters were determined.

##### 4.4.1 Pre-detection Parameters

Filtering is a key component of the algorithm and comprises the pre-detection parameters. Micro-seismic noise falls into the low frequency band, typically below 0.7 Hz. Cultural noise usually dominates frequencies above 3 Hz, while seismic events on short-period systems have their highest response around 1 Hz. The pre-detection band-pass

filter has been set to have a low cut of 0.7 Hz and a high cut of 3.5 Hz.

#### 4.4.2 Detection Parameters

The optimum detection parameters were determined by running the algorithm with twenty-five combinations of parameters on real data sets. Two different tests were performed on the data. The purpose of the first test was to determine the variations in false alarm rate and missed events as a function of the parameters. The first data set consisted of 24 hrs of USSN data and had two known teleseismic events. The events were recognized by manually studying the chart records. A windy day was chosen and the data were relatively noisy compared to most days in the area (see section 6.6 for examples of the effect of wind on USSN data). The  $\beta$ s (eq. 4.1) ranged from 0.970 to 0.990 in 0.005 increments. The delays (eq. 4.7) ranged from 10 to 100 in 20 sample increments. This leads to a total of twenty-five possible combinations. The threshold parameter  $\alpha$  was set to a ratio of 3.0.

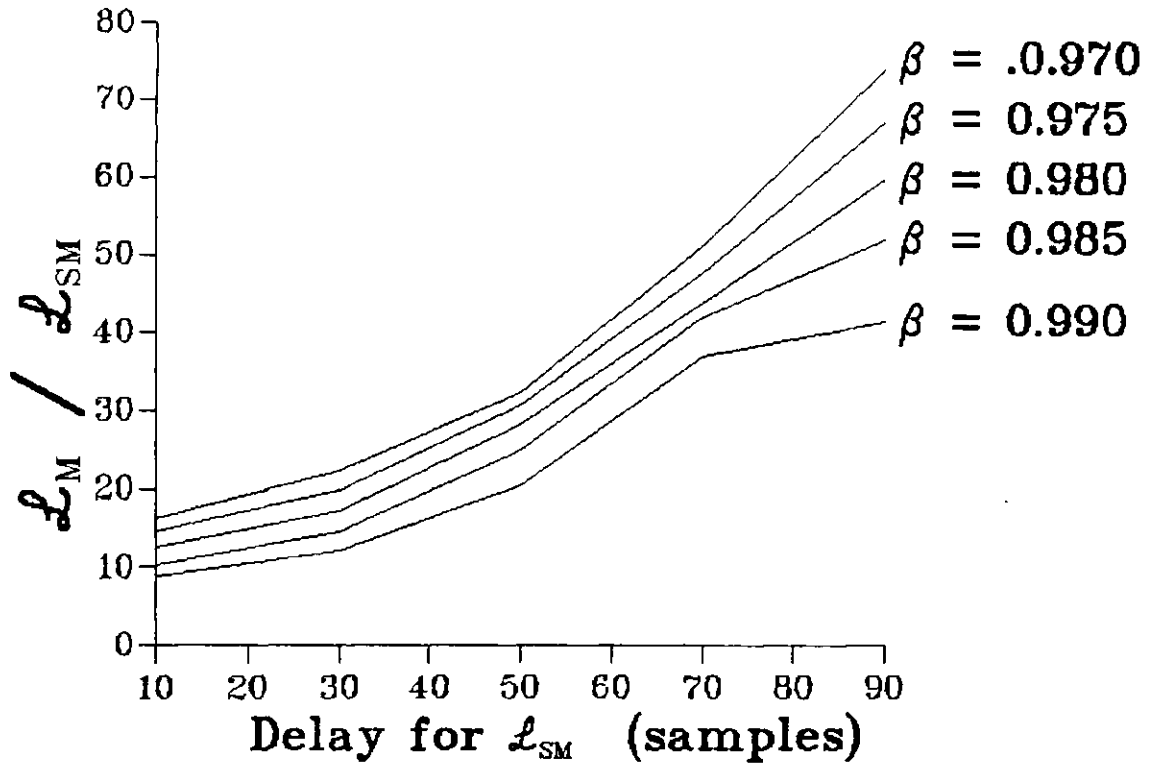
There were no false alarms for any of the combinations. Below (but not including)  $\beta = 0.980$ , there was only one detected event for the combinations rather than the two known seismic events. Processing time for the data did not change with the parameters, staying constant at about 45 min of CPU time on a DIGITAL 3200 VAX-station, for the 24 hrs of

data.

The purpose of the second test was to determine variation of detectability and timing accuracy with the parameters. The data consisted of a USSN regional distance three-component seismogram with an emergent first arrival. The lowest  $\beta$  gave the most accurate arrival times as compared to the times manually picked from the digital traces. Below, and including  $\beta = 0.980$ , the timing error was 0.2 sec late. These times were as good as those manually determined from the chart recorder seismographs. The ratio of  $\epsilon_m$  to  $\epsilon_{sm}$  was found to be larger for the lower  $\beta$ s and larger delays (figure 4.2).

Based on the test results, a  $\beta$  of 0.98 and a delay of 50 samples were chosen. The decision is a compromise between the two extremes: the first test showed that the higher  $\beta$ s detected all the known events, while the second test indicated that the lower  $\beta$ s gave a higher detectability. The lower  $\beta$ s seem to make the detection routine less robust. A  $\beta$  of 0.98 corresponds to a time constant of 50 samples (2.5 sec) for the exponentially weighted sum.

An  $\alpha$  of 3.0 seems to be adequate for the system. A number of  $\alpha$ s were tested on many recordings of cultural noise and regional and teleseismic events with  $\beta = 0.98$  and a delay of 50 samples. A regional event with a very weak initial phase arrival is shown in figure 4.3, together with the ratio  $\epsilon_m/\epsilon_{sm}$  and a plot of both  $\epsilon_m$  and  $\epsilon_{sm}$ . The ratio



$$L_M = \text{STA}$$

$$L_{SM} = \text{LTA}$$

Figure 4.2.  $L_M/L_{SM}$  versus delay for  $L_{SM}$ . The smaller  $\beta$ s give a higher detection ratio, however tests on a 24 hr segment of data show that the lower  $\beta$ s make the detector less robust.

## Detector Response

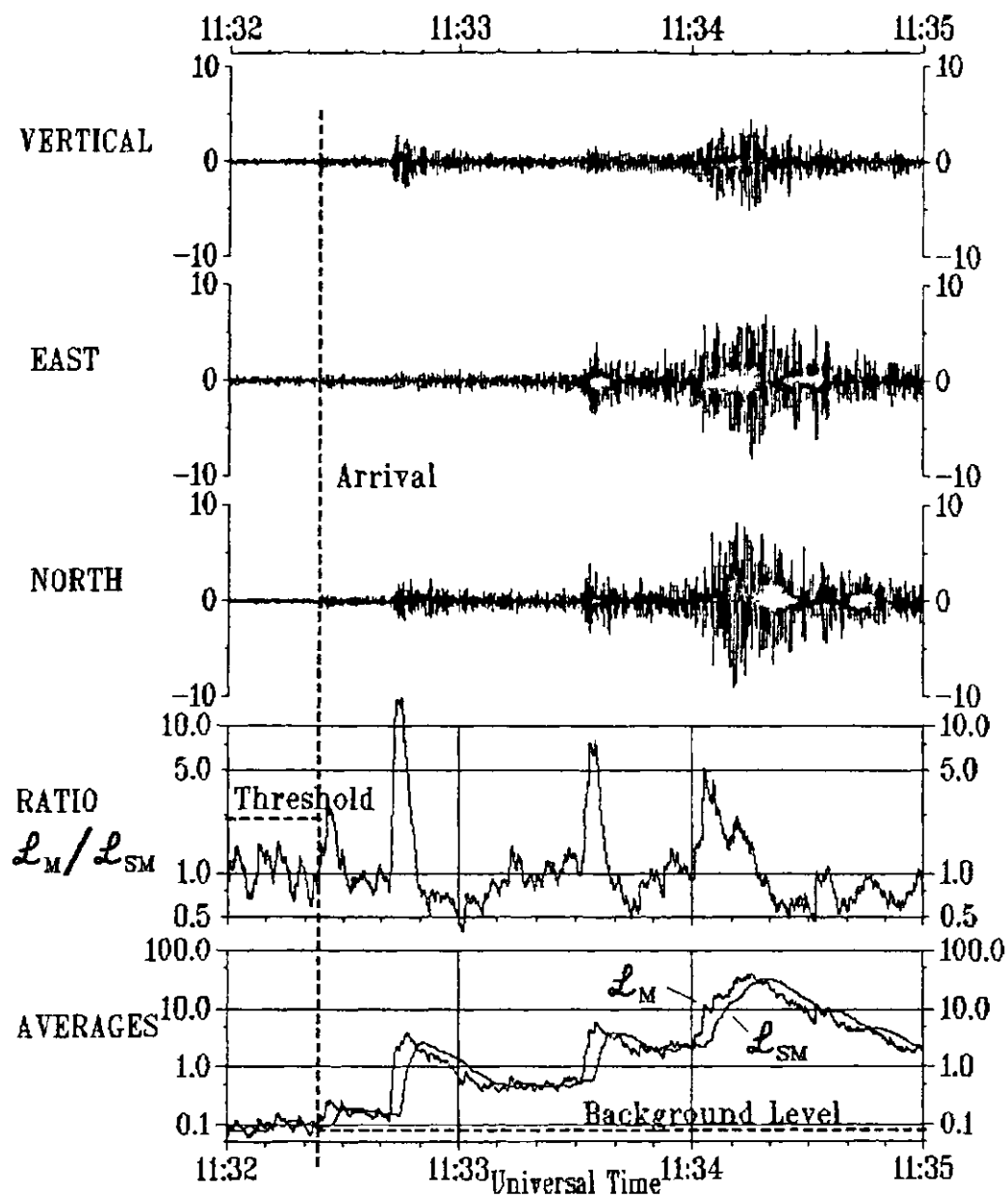


Figure 4.3. A regional event with a very weak initial phase arrival.  $L_M/L_{SM}$  rises above 3.0 - the threshold - even though the arrival is barely perceptible. The turn-off point is found when  $L_M$  drops to the background level.

$\mu m/\mu sm$  rises above 3.0 in this case, even though the arrival is barely perceptible.

#### 4.4.3 Post-detection Parameters

The post-detection parameters have been established from preliminary monitoring during the installation of the detector. The minimum event duration has been set to 5 sec and maximum array moveout time is set to 15 sec. A minimum of two stations is required for triggering a detection. The moveout time corresponds to a velocity of about 3.3 km/sec. This is a very slow apparent velocity for body waves, but includes the possibility of the detectors triggering on surface waves from regional events. The surface waves always have the largest amplitudes on seismographs recorded in this distance range; typical apparent velocities are around 3.5 km/sec.

#### 4.5 Test Results

After four months of operation the detector performance was reviewed, the results are presented in figure 4.4. The performance was found to be excellent, with 81% of the detections being true events. An analysis of the cause of the false alarms is also given in figure 4.4. A number of the detected events were so small that they were barely perceptible on the chart records. That makes determination

## Array Detector Performance (4 months of operation)

81.0% True Events	209 detected teleseisms
19.0% False Alarms	7 detected regionals
	1 missed local
	33 days of down time

### False Alarm Analysis

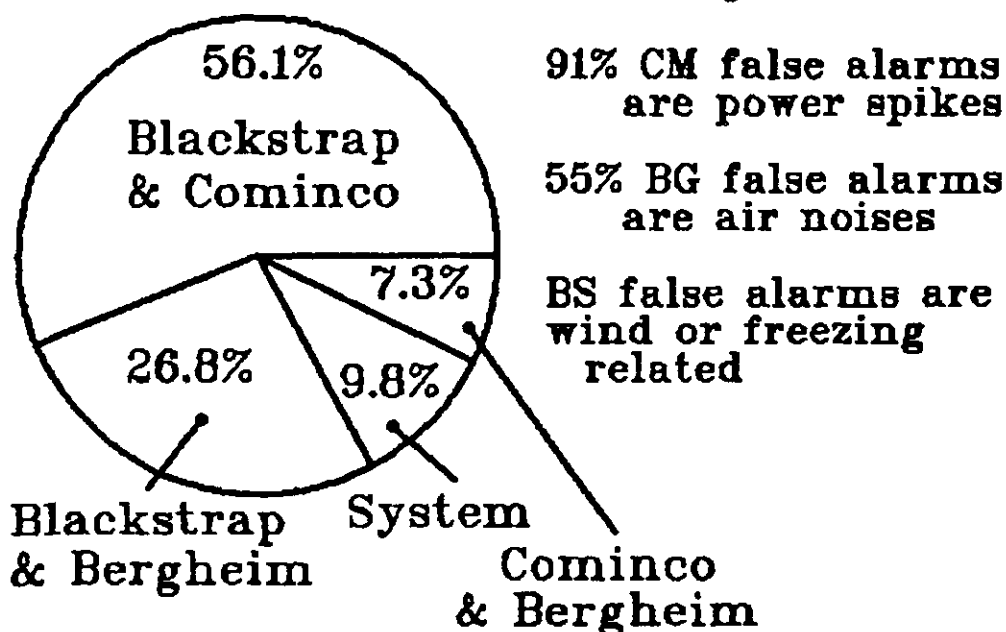


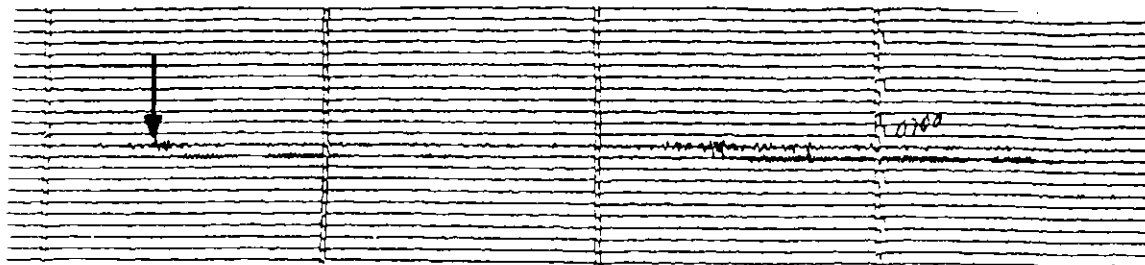
Figure 4.4. Detector performance evaluation and false alarm analysis based on four months of operation.

of the number of missed events difficult based only on visual inspection of the chart records. Figure 4.5 gives some examples of detected events.

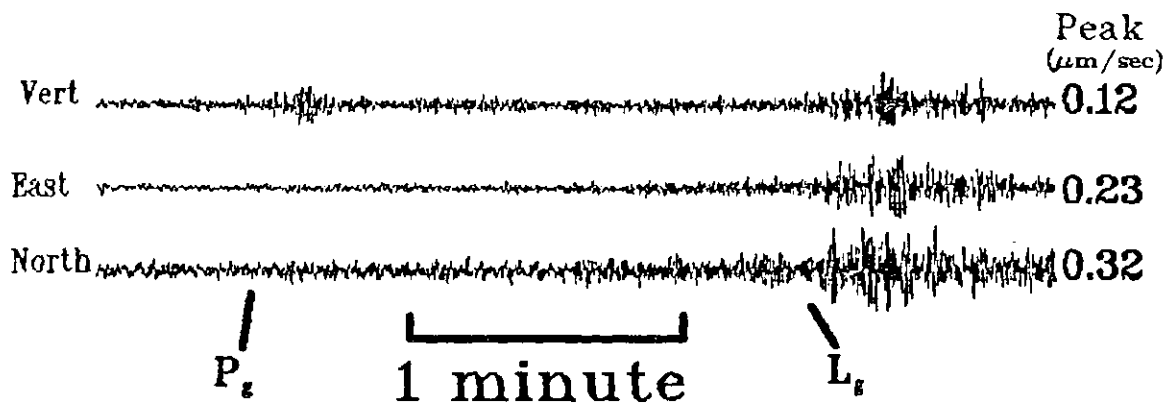
Most of the false alarms can be attributed to the BLK and COM stations. COM station is subject to many power spikes, and BLK is affected by wind and freeze-thaw cycles in the soil. A number of the false triggers on BRG resulted from unexplained high frequency, emergent events. They are found to travel with the velocity of sound waves, and may be related to sonic booms or explosions near the array.

One known missed event occurred during normal detector operation. The Potash Corporation of Saskatchewan's Lanigan mine experienced a noticeable event and notified the University several days after it had occurred. The mine is 120 km from the array and the event was quite small on the chart records so it was not noticed. The detector did not trigger on the event, but has been found to trigger on other events of similar trace motions (figure 4.5). As a result of the missed local event, the threshold,  $\alpha$ , was reduced by 20% to 2.4 after the four months of monitoring had been completed. The false alarm rate may rise, but that should not be a problem, as the rate was found to be very low in this study.

## Paper Record of a Regional Event



## Digital Record of Regional Event



## Paper Record of a Teleseism

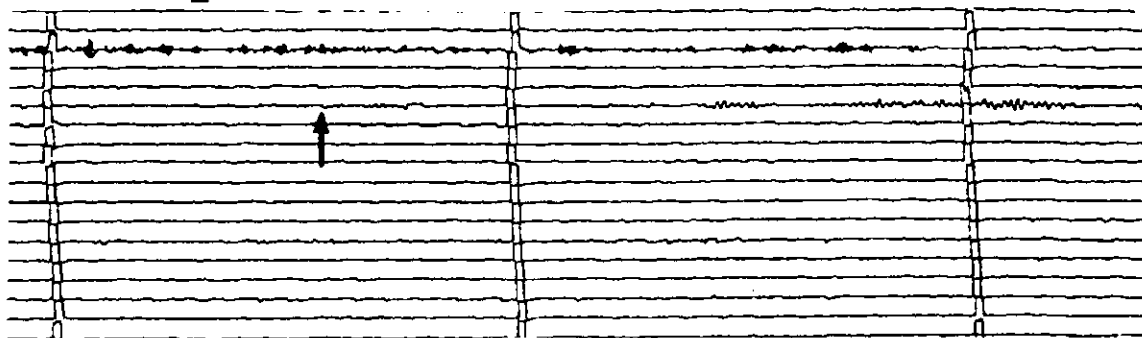


Figure 4.5. Seismograms of small detected events. A number of the detected events in the four month study (figure 4.4) were too small to be easily recognized on the helicorder records.

## CHAPTER 5

SEISMOGRAM PROCESSING AND INTERPRETATION

Seismograms contain information on both the source of the seismic event and the material through which the waves travel. Many techniques have been developed to facilitate processing and interpretation of seismograms. These methods can yield source size, amount of energy released, location, and seismic velocities and depths to layers within the earth.

The following chapter presents a number of programs which have been developed for processing and interpretation of data collected by the USSN. The programs have been compiled into one main module called US\_ANALYSE. Through the main program all the sub-programs can be accessed interactively using a graphics work station. A flow chart of the operations available in the program is shown on figure 5.1. The preliminary steps in the program involve choosing the data and filtering the traces. The program is further subdivided into two main streams: teleseismic and regional earthquake analysis.

### 5.1 Selecting the Data

The data saved by the event detector are in a compressed multiplexed form. US\_ANALYSE reads a selected

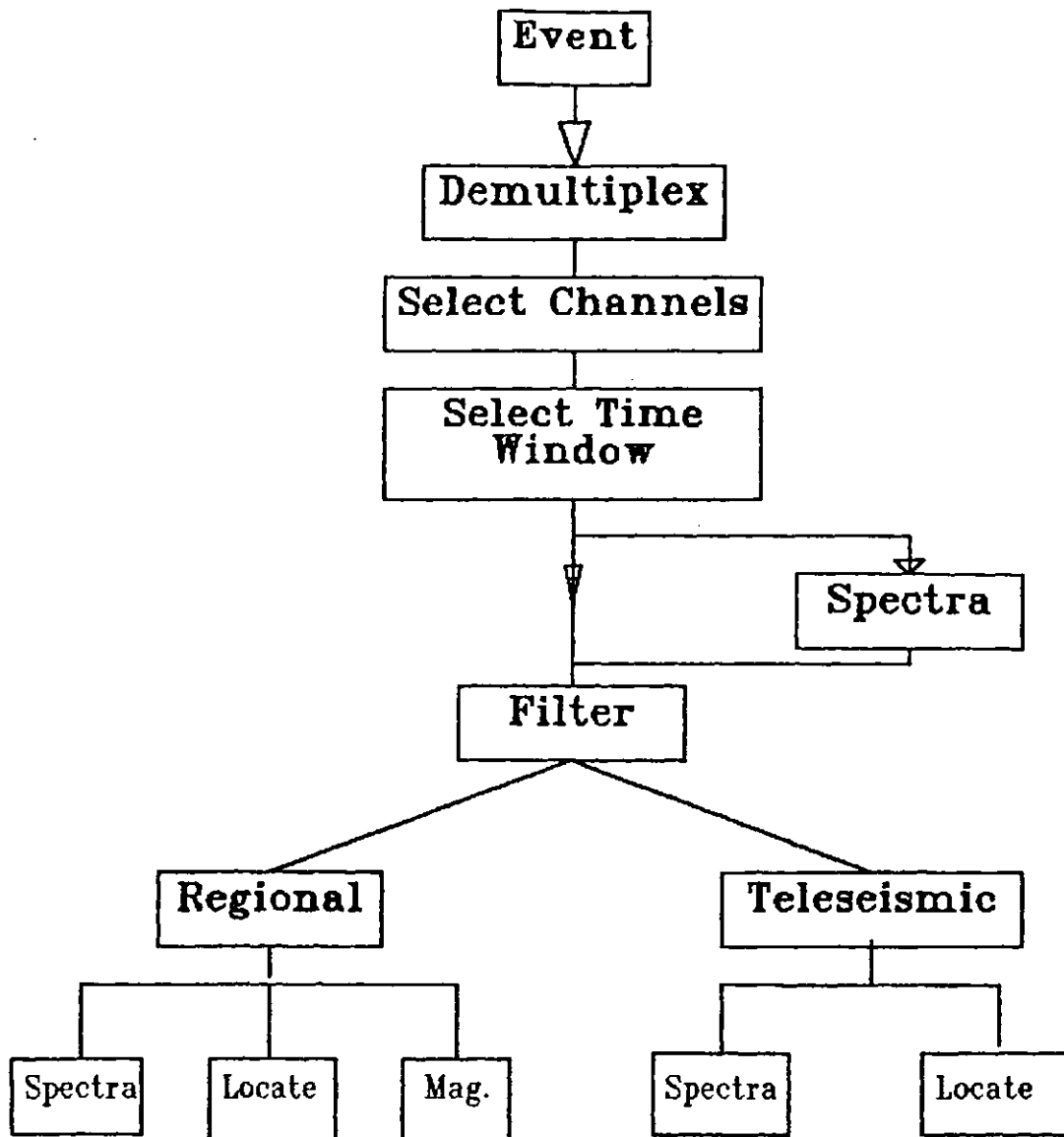


Figure 5.1. Typical processing flow in US\_ANALYSE for teleseismic or regional distance earthquakes.

file, demultiplexes the channels, and converts the data to a format suitable for presentation on a graphics terminal. The entire saved file is plotted on the screen and the user can then zoom in on a portion of interest using the mouse. A scrolling option is also available to move the viewing window up or down the traces. Once the desired data window is chosen, the processing can begin.

## 5.2 Filtering

The filtering component of US\_ANALYSE can be divided into two sub components: frequency filtering and deconvolution of the instrument response from the data.

### 5.2.1 Frequency Filtering

Frequency filtering can be used to remove undesired frequencies in the data and to improve the signal quality on the seismograms. US\_ANALYSIS uses a digital filter available from the VAXlab signal processing library. The filter is an adaptation of the  $I_0$  - sinh filter, which is described by Hamming (1983).

Through US\_ANALYSIS, the user can specify a low-pass, high-pass, band-pass or band-reject filter. The filter is nonrecursive so a length must also be specified for the operator. The length determines the sharpness of the filter. Longer operators give sharper cutoffs. A sharp

filter is desirable, but the processing time increases linearly with the length of the filter.

Gibbs Phenomenon oscillations are an undesirable side-effect resulting from sharp filters. The attenuation of the oscillations ( $a_0$  in units of -dB) can be controlled by an argument  $W$ :

$$|a_0| = 10^{(-W/20.0)} \quad 5.1.$$

Minimum damping of the oscillations occurs when  $W$  is set to 0.0. As  $W$  increases, the oscillations become smaller; but, the sharpness of the filter decreases. A compromise is suggested by using a  $W$  of 50.0.

Spectral analysis is often used to obtain filter cutoff points. An example is given in figure 5.2. Spectra are readily calculated by `US_ANALYSE` using the fast Fourier transform technique. The data to be transformed are selected with the mouse by delineating the window with the cursor. The plotted spectra can be displayed on log or linear axes. In the example on figure 5.2, frequencies below 0.7 Hz and above 4.0 Hz are removed using a band-pass filter. The filtering makes the data easier to interpret by improving the S/N.

### 5.2.2 Deconvolution Filtering

Instrument deconvolution restores the actual ground

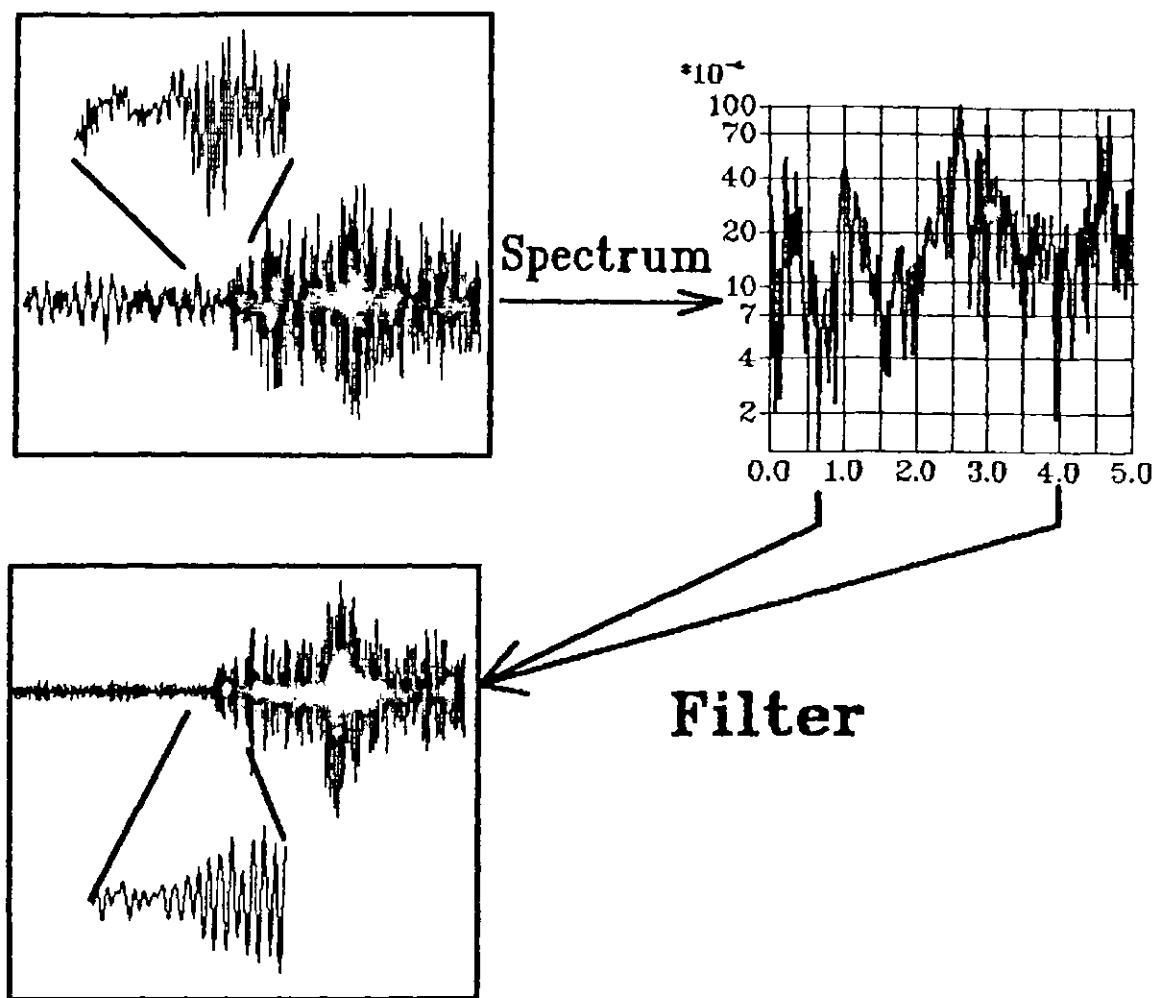


Figure 5.2. Band-pass filtering. The spectrum is convenient for determining optimum filter cut-offs in this example. The filtered trace shows an improvement in signal quality.

motions that occurred at the seismometers. The process also removes all the instrumental distortions, making the data easier to interpret as shown in figure 5.3. In this example, the first phase arrival is more discernible on the deconvolved trace. Also, the process has clarified many other packets of energy in the trace. The operator for the deconvolution that is used by US\_ANALYSE has 128 elements and was obtained by analyses of calibration pulses (described in chapter 3).

### 5.3 Teleseismic Earthquake Analysis

Teleseismic observations of earthquakes can provide an opportunity to study the characteristics of the crust below the array. For such a study, relative P phase arrival times between the stations are required. The arrival times are easily determined through US\_ANALYSE using cross-correlation between the channels. The primary P phase times are then used by the program to resolve the location of the event. In chapter 7, the errors in the locations of many events will be used to study velocity anisotropies in the crust in the Saskatoon area.

Magnitudes for teleseismic events are not calculated here because the earthquakes are widely recorded by other networks, such as the Canadian Geological Survey's Yellowknife array. Magnitudes calculated by the Yellowknife array are readily obtained through a computer link called

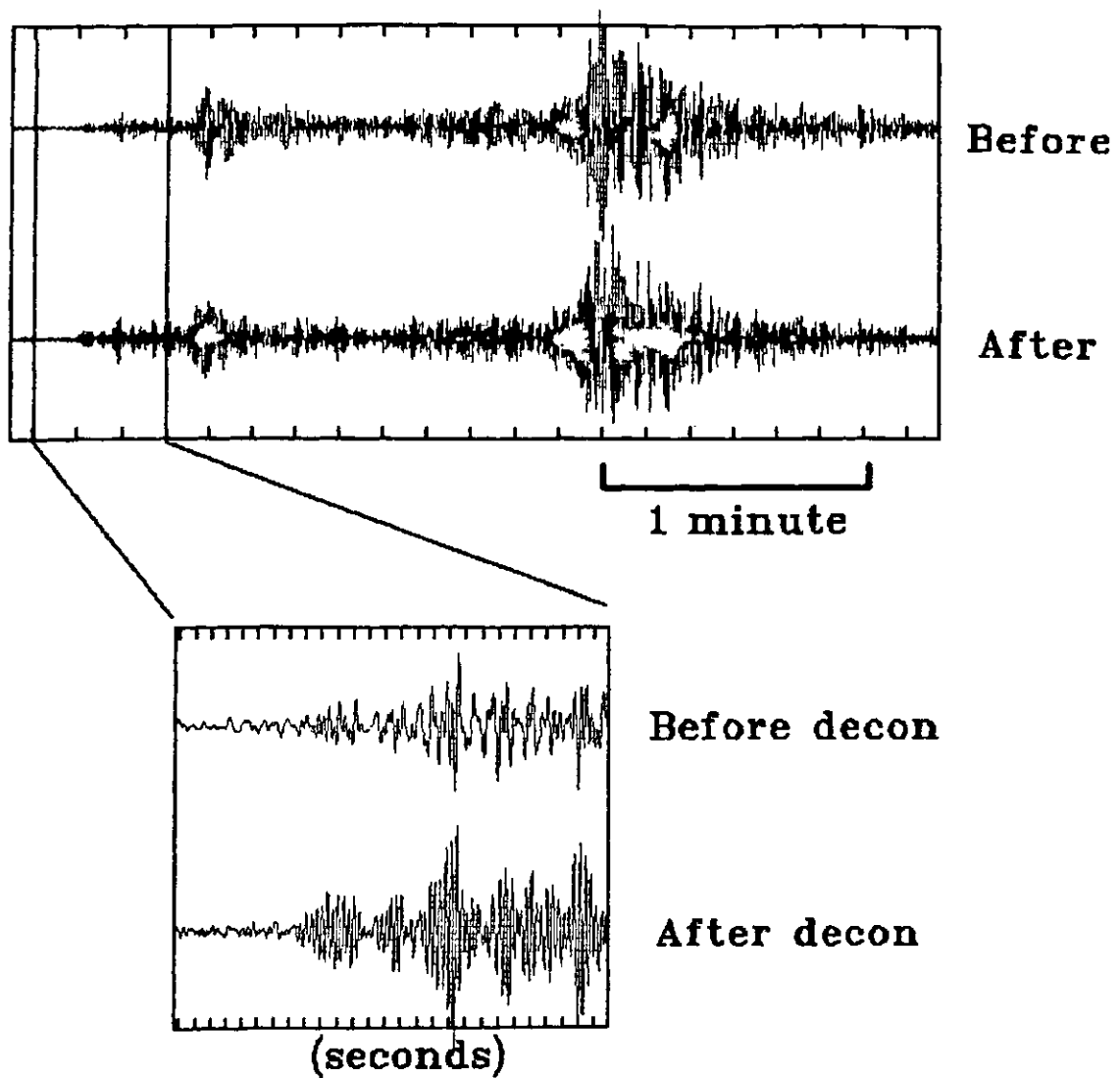


Figure 5.3. Improvements realized with deconvolution. The process makes the first phase arrival more discernable and clarifies many packets of energy in the seismogram.

DATAPAC.

### 5.3.1 Cross-correlation

In US\_ANALYSE, the initial P phases are picked interactively using the mouse to guide the cursor to the approximate position of the arrivals. The similarity between teleseismic waveforms makes cross-correlation useful for refining the arrivals (eg., Bungum and Husebye 1971; Mok et al. 1982; VanDecar and Crosson 1990). An example from US\_ANALYSE is shown in figure 5.4. The panel on the left shows the data before correlation. The traces have been aligned according to the initial arrival times picked by the analyst. The position of the initial picks are marked by a vertical dashed line in figure 5.4. The two vertical solid lines delineate the correlation window (which is 4 sec long in this case). The position and length of the window can be controlled by the analyst. The panel on the right displays the traces after correlation. Each trace is cross-correlated against the other two to find the optimum alignment between all the traces. The optimum times are displayed in a column on the right of figure 5.4, together with the correlation coefficients. After correlation, one can see that the traces appear to be well aligned.

The cross-correlation procedure has been found to be problematic in cases where the arrivals are not similar between the stations. Usually the first few cycles exhibit

09JAN92- Start time= 09:16:46.7

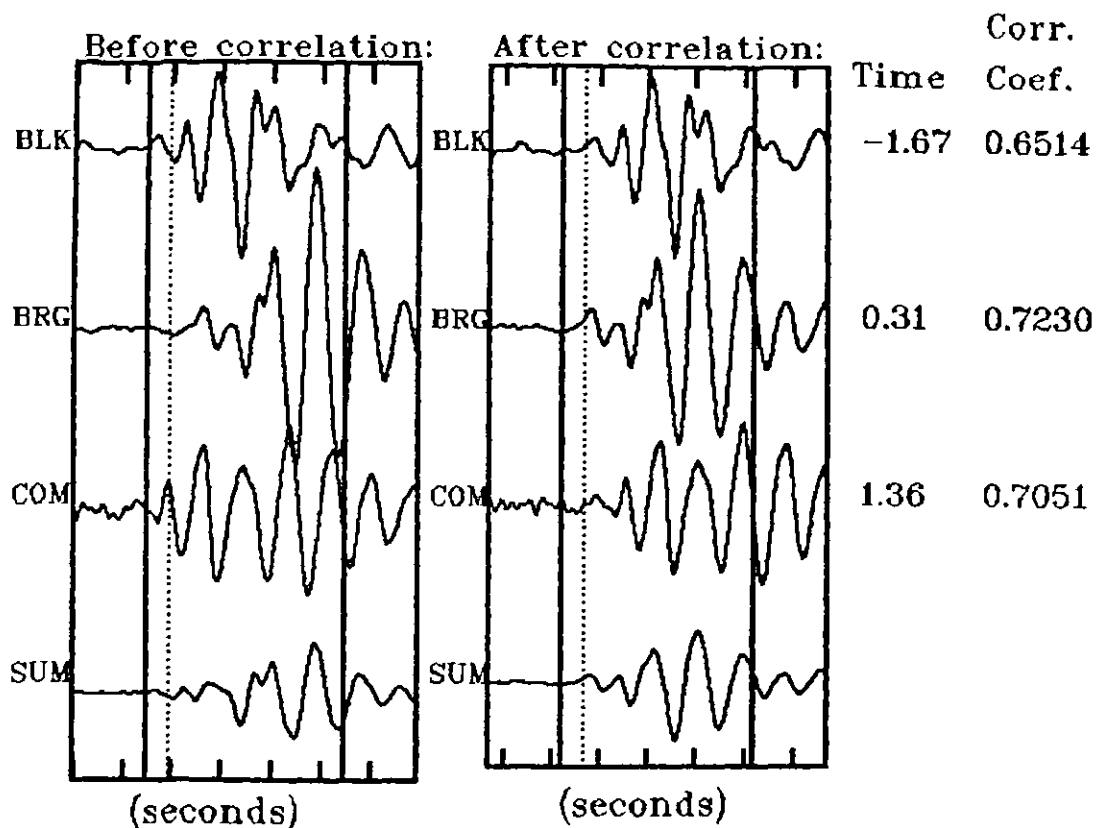


Figure 5.4. The utility of cross-correlation for improving arrival P phase picks from teleseismic earthquakes. The dashed line mark the phase arrival positions on the traces within the correlation window. The window is delineated by the two vertical solid lines. A typical window length is 4.0 sec.

some similarity so that the cross-correlation can be improved by shortening the correlation window. The problem is particularly pronounced with smaller amplitude events and events that have shallow hypocentral depths. Also, the Cominco station (which is 1 km deep) often exhibits a surface multiple arriving about 0.6 sec to 0.8 sec after the first arrival. As a result of these problems, the correlation procedure cannot be automated and intervention by the interpreter is required.

### 5.3.2 Location

Final arrival P phase picks are used for location by fitting a plane to the cross-correlation derived times. This is valid for distant events since the aperture of the array is small compared to the velocity gradient in the earth at greater depths. A fitted plane completely describes the location of the earthquake: the dip direction is the azimuth, and the dip is the apparent velocity. The latter is uniquely related to epicentral distance and has been tabulated by Herrin et al. (1968a).

The arrivals times have an accuracy of 0.1 sec for events with adequate S/N, so that the apparent velocity is accurate to about 0.3 sec/deg, and the azimuth is accurate to 3.0 deg. These are average quantities; the actual error varies with both the distance and azimuth.

US\_ANALYSE uses spherical trigonometry to determine the

location of the epicenter. The initial location must then be corrected because the Cominco station has a large difference in elevation from the other two stations in the array. The correction function also accounts for velocity anisotropies and structures under the array. The derivation of this function is discussed in chapter 7. The relationship varies both with distance and azimuth. The corrected epicenter coordinates are employed by US\_ANALYSE to produce a map which shows the geographic location of the earthquake (eg., figure 5.5).

The map displays both the location of the epicenter and the inherent error in the location. The true errors in apparent velocity and azimuth are transformed into errors of latitude and longitude by US\_ANALYSIS. The error region is plotted around the epicenter. The map also has an arrow from the epicenter, which indicates the azimuth to the center of the USSN array. The colours and the size of the mapped region can be controlled by separate data files accessed by US\_ANALYSIS each time a map is produced.

The location method can only be used for earthquakes within about 100 deg of the array. Beyond this distance P-waves begin to graze the earth's core and diffractions occur. Also, initial arrivals from regional earthquakes will be refractions along the upper mantle or lower crust. These arrivals persist to about 1800 km and have an apparent velocity of 8.30 km/sec (see chapter 7). Derived locations, using the fitted plane method over this distance range, will

05FEB92- Arrival time= 05:43:32.4

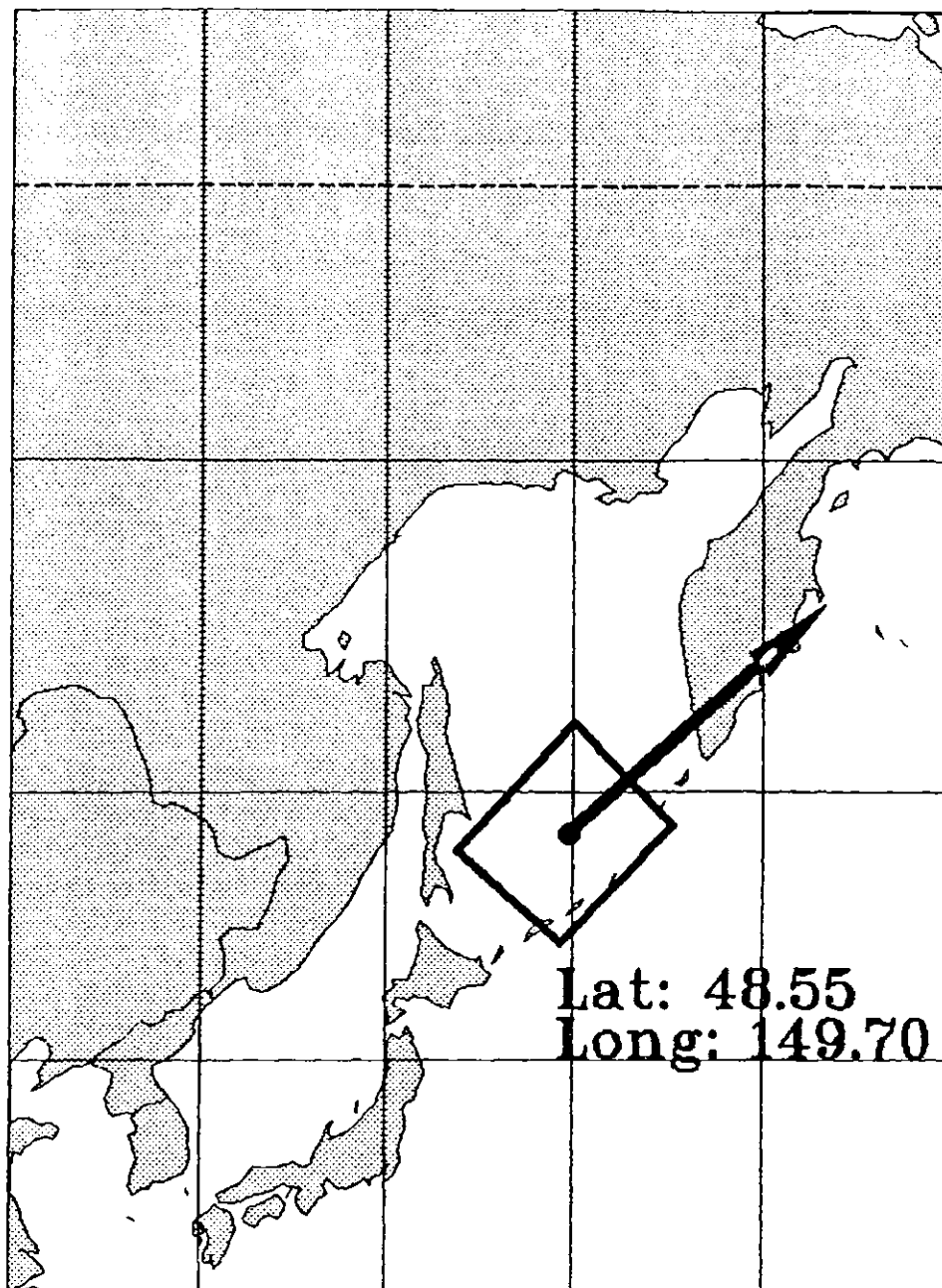


Figure 5.5. Example of an earthquake location map. The tail of the arrow is the location. The box delineates the inherent error location region. The arrow points in the azimuthal direction of Saskatoon.

be ambiguous because the apparent velocity is constant with distance.

#### 5.4 Regional Earthquake Analysis

Numerous seismograph stations close to the epicenter are required for a thorough examination of a regional earthquake. The problem in Saskatchewan is that few stations are available to offer data for analysis. The events are usually small and not widely recorded. Figure 5.6 shows the locations of stations in the region and also plots the known seismicity. Earthquake information is listed in tables 5.1 and 5.2 for natural and induced events, respectively.

Recordings of regional events by the USSN offer meaningful contributions to an understanding of Saskatchewan seismicity. Crucial components of the analysis procedure are the filtering and deconvolution because phase arrivals within the coda are enhanced, and the ground motion histories are restored. As a result, the location estimate is improved and a magnitude can be determined.

##### 5.4.1 Location

Several phase arrival times from at least three stations are required for regional earthquake location. The phase arrival times are picked interactively by the analyst

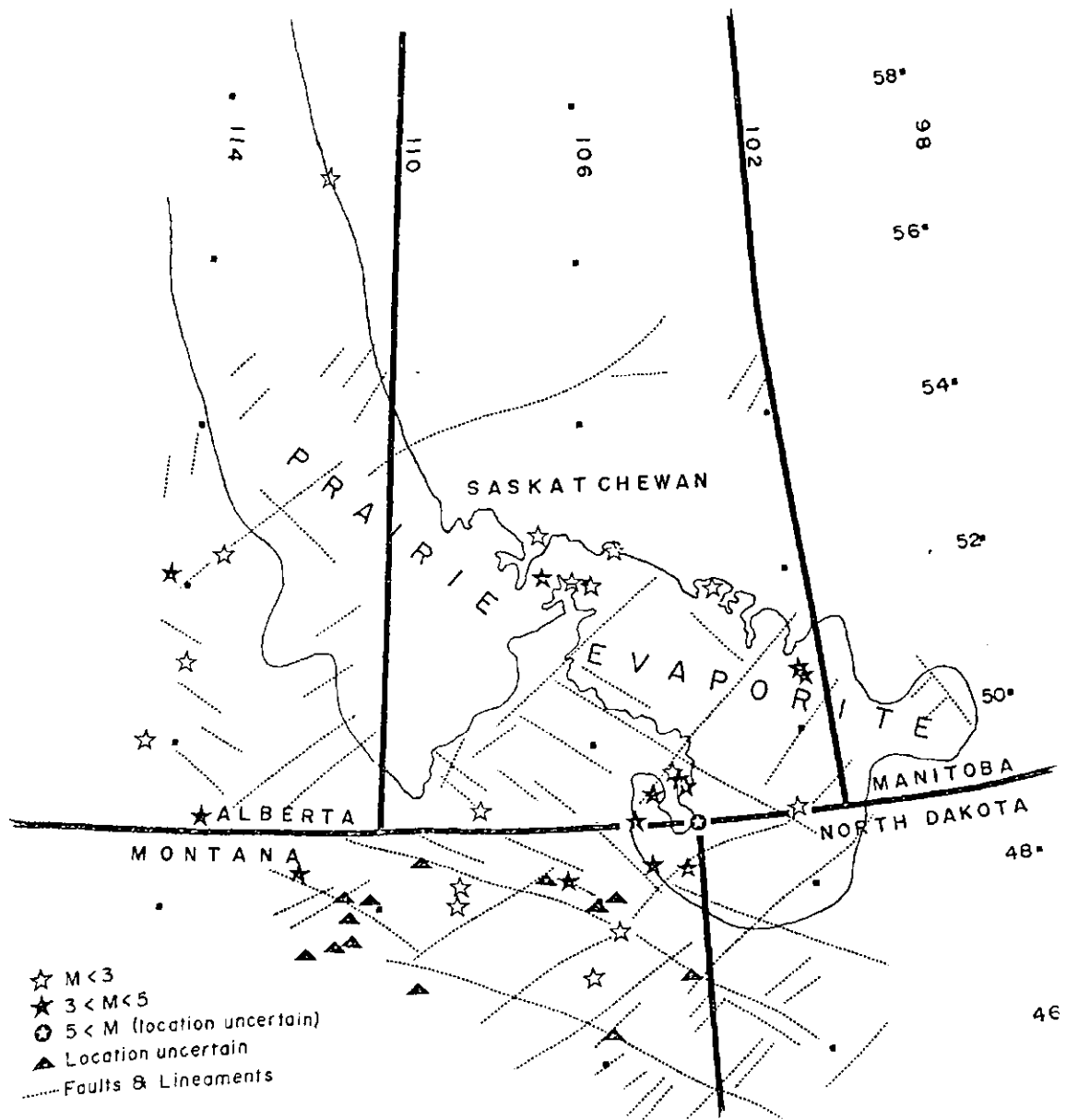


Figure 5.6. Known seismicity in southern Saskatchewan. Map also shows faults and basement lineaments in the area (map from D.J. Gendzwill, personal communication, 1992).

	Location	Date	U.C.Time	Lat	Long	Mag
1	U.S. Border	1909, May 16	04:15:--	49.00	104.00	5 1/2
2	Val Marie	1968, Sep 11	12:00:06	49.25	108.14	2.7
3	Radville	1968, Oct 11	12:28:04	49.61	104.49	2.8
4	Bengough	1972, Jul 26	03:58:19	49.35	104.93	3.7
5	Radville	1976, Mar 23	22:31:47	49.56	104.37	3.2
6	Radville	1976, Mar 25	00:12:16	49.39	104.27	3.5
7	Humboldt	1976, May 15	06:21:12	52.45	105.44	2.3
8	Kuroki	1981, Jan 10	08:34:31	51.91	103.44	3.1
9	Big Beaver	1982, Aug 17	04:50:31	49.01	105.27	3.9
10	Redberry Lake	1984, Feb 5	04:30:14	52.70	106.95	2.3
11	Northgate	1985, Oct 10	12:43:37	49.07	102.17	2.9
12	Kuroki	1991, Apr 25	20:53:53	51.90	103.48	3.1
13	Kuroki	1991, Apr 26	00:02:26	51.90	103.48	2.5

Table 5.1. Natural earthquakes in Saskatchewan (data from D.J. Gendzwill, personal communication, 1992).

	Location	Date	U.C. Time	Lat.	Long.	Mag.	Ref
1	I.M.C. K-1	1976, Nov 7	12:27:15	50.69	101.94	3.0	GSC
2	I.M.C. K-1	1978, Nov 4	01:23:52	50.70	101.90	3.1	GSC
3	Cory	1979, Nov 18	23:02:13	52.10	106.92 S	2.4	GSC
4	Cory	1980, Feb 29	19:41:41	52.12	106.93 S	3.0	GSC
5	Cory	1980, Mar 18	00:31:51	52.08	106.90 S	2.8	
6	Cory	1980, Aug 6	05:23:53	52.11	106.93 S	2.3	
7	I.M.C. K-1	1981, Jan 27	06:13:11	50.70	101.90 S	2.9	
8	I.M.C. K-1	1981, Jan 27	19:34:09	50.70	101.90 S	2.7	
9	I.M.C. K-2	1981, Apr 13	03:28:21	50.66	101.85 S	3.2	
10	Cory	1981, May 11	14:50:09	52.11	106.91 S	2.3	
11	Cory	1982, Jan 8	16:46:16	52.11	106.93 M	2.4	
12	I.M.C. K-1	1982, Sep 28	07:17:49	50.72	101.95 S	3.4	
13	Cory	1983, Jan 6	02:35:04	52.12	106.93 S	2.7	GSC
14	C.C.P.	1984, Feb 20	01:19:23	51.95	105.77 S	2.4	GSC
15	I.M.C. K-2	1984, Sep 27	08:48:10	50.65	101.89 S	3.5	GSC
16	I.M.C. K-2	1984, Oct 25	13:00:18	50.65	101.89 R	2.5	GSC
17	I.M.C. K-1	1984, Nov 2	10:24:21	50.68	101.90 R	3.0	GSC
18	I.M.C. K-2	1984, Nov 9	02:11:41	50.61	101.83 S	2.7	DJG
19	Cory	1985, Apr 6	19:43:39	52.11	106.93 R	2.9	GSC
20	I.M.C. K-2	1985, May 15	10:39:03	50.70	101.80 R	3.0	GSC
21	I.M.C.	1985, Nov 29	19:27:35			2.5	DJG
22	I.M.C. K-2	1985, Dec 25	15:50:--	50.65	101.88 S	2.6	DJG
23	I.M.C. K-2	1986, Jan 6	08:--:--				DJG
24	Cory	1986, Jan 29	18:02:36	52.11	106.93 R	1.5	DJG
25	I.M.C. K-2	1986, May 18	16:20:13	50.74	101.85 R	2.9	DJG
26	Cory	1986, Dec 6	14:51:18	52.11	106.93 R	2.1	DJG
27	P.C.A.	1987, Jul 3	11:28:43	52.06	106.34 S	2.1	DJG
28	P.C.A.	1987, Jul 21	08:06:40	52.06	106.34 M	2.7	GSC
29	I.M.C. K-2	1987, Jul 30	14:33:19	50.66	101.84 S	3.3	GSC
30	I.M.C.	1987, Oct 22	04:34:29			3.4	DJG
31	I.M.C. K-2	1988, Jan 7	09:57:05			2.7	DJG
32	I.M.C. K-1	1988, Feb 18	05:27:13	50.71	101.95 S	3.6	DJG
33	I.M.C. K-2	1988, Mar 25	22:14:19	50.65	101.89 M	3.7	DJG
34	I.M.C. K-1	1988, Nov 7	14:28:20	50.72	101.89 S	3.5	DJG
35	I.M.C. K-2	1989, Jan 20	15:56:10			2.7	DJG
36	Cory	1989, Mar 29	04:10:30	52.12	106.95 S	2.2	DJG
37	Cory	1989, Jun 5	12:43:05	52.12	106.95 S	2.6	DJG
38	Lanigan	1991, Sep 11	23:25:28.6	105.155	51.869 M	2.3	DJG

R = location based on regional seismic network, accuracy 20 km.  
 No symbol where regional location is not available.  
 S = location based on isoseismal survey, accuracy 1 km.  
 M = location based on microseismic system, accuracy 100 m or better.

Note:

Event 22 occurred coincidentally with arrival of surface waves from a M = 5.7 Northwest Territories earthquake. It was felt but instruments were saturated with the NWT event.

Event 23 was felt but not recorded on instruments

GSC - Geological Survey of Canada

DJG - Dr. D.J. Gendzwill

Table 5.2. Mining induced earthquakes in Saskatchewan (data from D.J. Gendzwill, personal communication, 1992).

on a work-station. US\_ANALYSE compares the phase time differences to a travel time function in order to determine a distance to the event. A detailed discussion on the crustal model, regional travel time function and its derivation can be found in chapter 7. Event azimuth is estimated by using the arrival times of the phases to find the direction of approach. With the direction and distance, a location can be obtained.

Many stations are needed around an event for a reliable estimate of the epicenter. The location method used by US\_ANALYSE offers a preliminary appraisal of an event origin. Regional USSN seismograms have only a small spatial sampling of the radiated waves. Unknown velocity variations in the crust cause ray paths to deviate, which introduces uncertainty into the locations. Phase arrival times measured on the USSN seismograms can be used in conjunction with recordings from other stations in the area to enhance location accuracy.

#### 5.4.2 Regional Magnitude Calculation

The magnitude relationship used by US\_ANALYSE is the Nuttli scale ( $M_N$ ). This function was empirically determined from eastern North America earthquakes and is reliable between distances of 400 km and 2000 km (Nuttli 1973; Horner et al. 1973). The scale is used by the CSN and the United States Geological Survey (USGS) for regional earthquakes.

$M_N$  is calculated from short-period vertical ground amplitudes of Love waves:

$$M_N = 3.3 + 1.66 \log(\hat{\Delta}) + \log(A/T), \quad 5.2$$

where:  $\hat{\Delta}$  is epicentral distance in degrees,  
 A is zero to peak maximum trace amplitude  
 in  $\mu\text{m}$ ,  
 and T is the corresponding period (sec)  
 of the wave.

The factor 3.3 in equation 5.2 is replaced with -0.10 when  $\hat{\Delta}$  is measured in kilometers. The USSN seismograms are proportional to ground velocity; so when A is differentiated, A/T in equation 5.2 is reduced to  $A/2\pi$ .

$M_N$  is interactively determined by US\_ANALYSE. Love wave coda are windowed by the interpreter using the mouse; then US\_ANALYSE finds the largest trace particle velocity in  $\mu\text{m}/\text{sec}$ . This measurement along with a distance estimate are used to obtain  $M_N$ . The accuracy of  $M_N$  for large events is about 0.2 units and is controlled by the S/N.

Estimates of  $M_N$  can often vary by as much as one unit between stations in the CSN (for an example, see Horner et al., 1973). To test US\_ANALYSE's accuracy,  $M_N$  estimates were compared to CSN and National Earthquake Information Centre (NEIC) values for seven widely recorded regional earthquakes listed in table 5.3. The USSN seismogram

Date	Location	Lat	Long	$\Delta$ (km)	$M_N$	US_ANALYSE $M_N$
28Jan89	Rocky Mtn. House,Alta.	52.2	-115.2	586	3.4	3.5
20Oct89	Rocky Mtn. House,Alta.	52.2	-115.2	586	3.6	3.6
14Apr90	Washington State	48.8	-122.0	1115	4.7	4.5
19Oct90	Quebec	46.5	-75.6	2310	5.0	4.9
11Nov90	Rocky Mtn. House,Alta	52.1	-115.3	592	3.6	3.5
30Nov90	Montana State	47.8	-113.2	667	3.5	3.6
25Apr91	Kuroki, Sask.	51.9	-103.5	215	3.2	3.5

Table 5.3. Nuttli magnitude estimate comparison. The list of regional earthquakes compares US\_ANALYSE estimates of  $M_N$  to the values published by the CSN and the NEIC.

distances vary from 200 km to 2200 km and magnitudes of the events range from  $M_N$  3.2 to 5.0. The agreement was found to be excellent at  $\pm 0.1$  units for all but one of the events. That earthquake has a difference of 0.3 units, and also has the smallest epicentral distance at 200 km. The distance may be too small for an  $M_N$  calculation since the Nuttli scale was intended for epicentral distances greater than about 400 km.

Magnitude estimates were also compared between the USSN stations. Bergheim and Blackstrap are in good agreement, while Cominco estimates are far too low. Trace amplitudes of Love waves on Cominco seismograms are often four times as small as the surface recorded seismograms. Most of the higher mode surface waves are confined in the upper sediments so the trace amplitudes should decrease with depth. Hauksson et al. (1987) report a similar experience with vertically incident P- and S-waves, where they found the amplitudes to be four and nine times smaller, respectively, at a depth of 1500 m.

#### 5.4.3 Spectral Studies for Source Parameters

Spectral analysis of P- and S-wave arrivals offers a different approach to magnitude calculation. The spectra are presented as particle displacement versus frequency in a log-log plot. Ideal spectra would exhibit a plateau for the lower frequencies, with a sudden transition to a certain

slope for the higher frequencies. The level of the plateau ( $\Omega_0$ ) depends on the released energy. This can be related to magnitude, seismic moment ( $M_0$ ), or stress drop ( $\Delta\sigma$ ). The fall-off point of the plateau, the "corner frequency" ( $f_0$ ), is inversely proportional to the fault area radius ( $R_0$ ). An example of the analysis is given in figure 5.7; the necessary equations are listed in the figure. A full discussion on the topic, and case histories of the methods applications, can be found in Aki (1967), Brune (1970, 1971), Wyss and Hanks (1972), Bath (1974), and Spottiswoode and McGarr (1975).

The spectral analysis example in figure 5.7 is on the vertical seismogram from the "Kuroki earthquake"; a local Saskatchewan event. Both P- and S-wave displacement spectra are displayed. The low frequency plateaus ( $\Omega_0$ ) and corner frequencies ( $f_0$ ) are labeled in the figure. Ideally, spectral analysis is completed on all the orthogonal components of the S-wave coda. Unfortunately, the horizontal seismograms were clipped for this earthquake. Using the vertical S-wave displacement spectrum, the spectral parameters for the example are as follows: a seismic moment ( $M_0$ ) of  $8.3 \times 10^{12}$  Nm, a source radius ( $R_0$ ) of 310 m, and a stress drop ( $\Delta\sigma$ ) of 120 kPa. The seismic moment can be related to a "moment magnitude" using the equation given by Spottiswoode and McGarr (1975), which is:

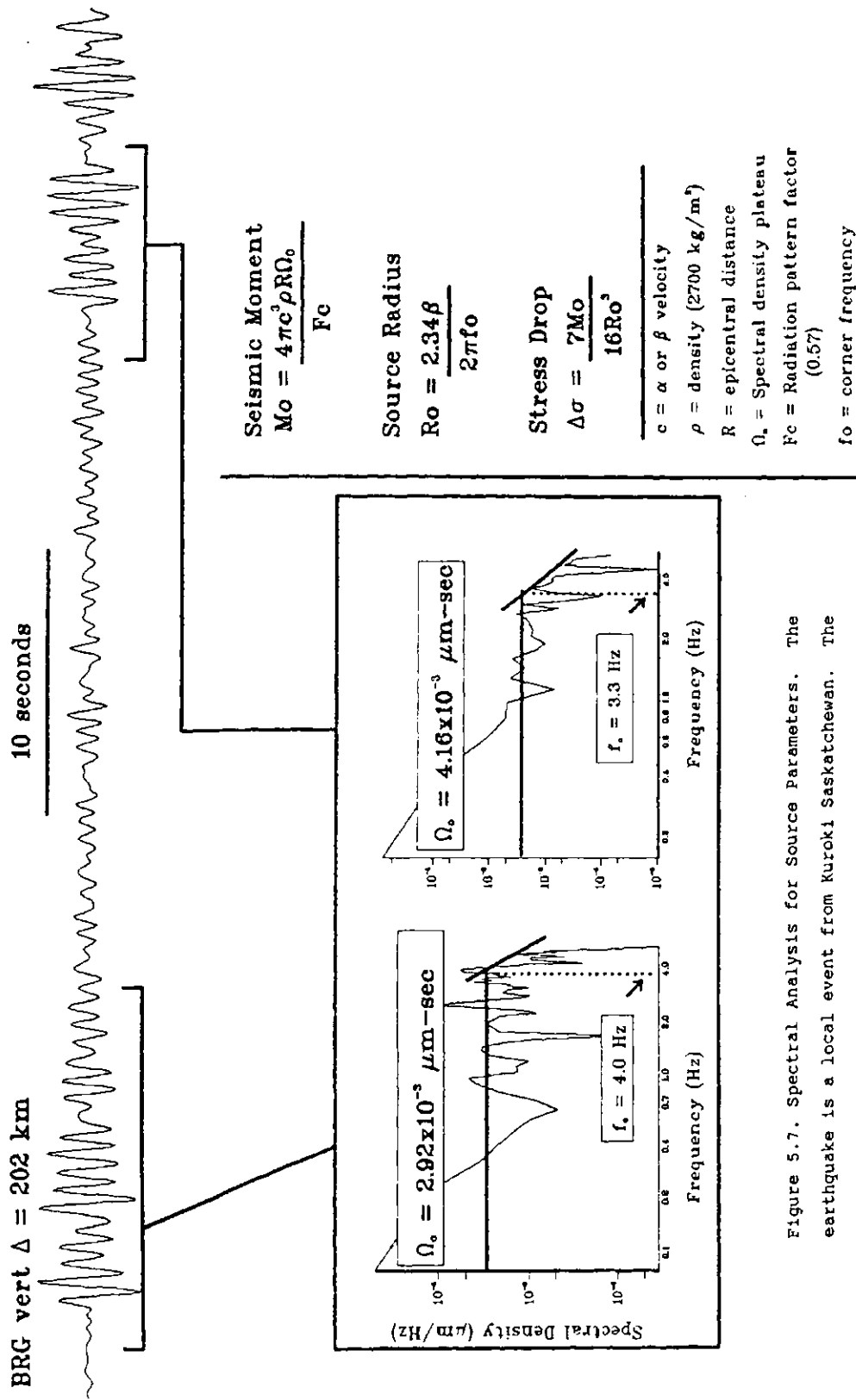


Figure 5.7. Spectral Analysis for Source Parameters. The earthquake is a local event from Kuroki Saskatchewan. The event size was  $M_w = 3.2$ . Note the exceptional S-wave arrival.

$$\log(M_0) = 10.7 + 1.2 M, \quad 5.3$$

where:  $M_0$  is in Nm,

$M$  is moment magnitude.

For the Kuroki earthquake, a moment magnitude of 1.9 is calculated. The GSC Nuttli magnitude for this event was 3.2 so the derived seismic moment appears to be almost forty times too small. The discrepancy is due to the omission of the horizontal components (which were clipped). The horizontal seismograms always have the largest displacements for S-waves from local earthquakes.

The spectral analysis procedures have not been automated in US\_ANALYSE. These procedures are difficult to automate but are easily completed manually, on paper copies of the spectra. Displacement spectra are readily calculated and plotted on paper by the program.

## CHAPTER 6

STUDY OF SEISMIC NOISE IN THE SASKATOON AREA

The ambient earth noise at the stations in the USSN has a great influence on the reliability of recordings of earthquakes within Saskatchewan. Low noise levels at a station increase the likelihood of recording small magnitude events. Seismic noise is a complex function of time, location, and frequency (Carter et al., 1991). Differences in noise levels between the USSN stations should be especially pronounced because of varying site conditions. The BRG station is a soundly constructed vault, whereas BLK is an open site, and COM is at 1 km depth within an operating mine. In this chapter, the ambient short-period earth noise in the Saskatoon area is investigated to determine how varying site conditions, time of day, and time of year affect the noise. The study is based on one year of continuous noise monitoring. The results are used to devise a minimum perceptible event magnitude as a function of distance for the Saskatoon area.

### 6.1 The Sources and Character of Short-Period Seismic Noise

The noise field consists of body waves, fundamental- and higher-mode surface waves, and forced deformations of

the earth's surface. Noise signals are similar to seismic signals in that they are governed by their sources, travel paths, and receiver sites. However, in contrast to seismic signals, the noise sources can be very complex as they are distributed over large areas and are confined to the surface (Carter et al., 1991). Most noise is attributed to phenomena such as cultural activity, weather disturbances, wind, sea tides, ocean storms, etc.. The nature of these sources change with time causing a non-stationary component in the noise. Some of the variations in the noise show regular patterns. The diurnal changes can be related to cultural activity, and seasonal patterns are related to changes in the climate.

Cultural noise variations can be significant for surface stations. It is widely accepted that this effect is confined to frequencies between 1 and 100 Hz (eg. Bungum et al., 1985; Given, 1990; Carter et al., 1991). In the USSR (now the CIS) Given (1990) observed time-of-day variations in noise power as large as 10 dB. Given notes that the variations are site dependent. Obviously, stations close to urban centers will show more variation than isolated sites. Station construction can also influence variations in cultural noise. Given found that soundly constructed vaults cannot eliminate cultural noise, but are necessary for reducing its impact.

Seasonal changes in noise are manifested in the lower frequencies. Detailed studies on microseisms are given by

Basham and Whitham, 1966, Toksöz and Lacoss, 1968, Rind and Donn, 1979, and Rind, 1980. Microseisms originate from ocean wave interaction and large atmospheric pressure disturbances. The most affected frequencies are between 0.1 and 0.2 Hz (ie., the micro-seismic peak); the influence is negligible above 0.7 Hz. Microseisms are significant in the winter because of the increase in ocean storm activity. Near coastal areas, microseisms can dominate seismograms during storms (seismogram examples in Kulhánek, 1990). Even within the center of continents, Given (1990) found that the micro-seismic peak can increase by 7 dB in noise power during the winter.

Wind-induced seismic noise is not as well understood as cultural or micro-seismic noise. Kromer (1986) found that the seismic noise at an array in south east Norway was most affected by wind up to velocities of 3 m/sec. Little change in the noise was noticed with higher velocities. In contrast, Gurrola et al. (1990) found that the wind had little affect on noise at stations in the U.S. and the C.I.S. until velocities of 4 to 5 m/sec were reached. Both studies used data collected from seismometers in seismic vaults. This may imply that surface vegetation and geology control the influence of wind on seismic noise.

There is a general consensus that borehole and mine seismograph sites are quieter and more stationary than surface locations (Frantti, 1963; Isacks and Oliver, 1964; Fix, 1972; Bungum et al., 1985; Bache et al., 1986; Given,

1990; Gurrola et al., 1990; and Carter et al., 1991). The reduction in noise increases with depth; the most noticeable improvement is in the frequency band between 1 and 100 Hz. Micro-seismic noise does not decrease significantly as a function of depth. This is thought to be related to the structure of microseisms which propagate both as body waves and higher mode surface waves (Douze, 1967; Toksöz and Lacoss, 1968). In contrast, cultural noise consists mainly of fundamental-mode Rayleigh waves, and random body waves (Douze, 1967). The Rayleigh waves are most prevalent at the surface, so deep seismograph sites show significantly less cultural noise than surface stations. Also, the wind-effect on seismic noise decreases rapidly with depth (Sorrells et al., 1971; Gurrola et al., 1990; Carter et al., 1991). In general, deep seismographs have lower noise levels and better S/N than surface sites.

## 6.2 Noise Data and Spectrum Calculation Methodology

One year of digital noise data has been compiled from the USSN. Noise samples were collected for all stations, six times daily, at four hour increments. Each noise window was sampled at 20 Hz and had a length of 3 min 24.8 sec.

The noise is studied as power spectral density functions. The spectra were calculated following procedures similar to Bath (1974). The steps are listed as follows:

- 1 Each station sample was divided into 15 overlapping

- windows of 512 samples in length;
- 2 The dc level and any drift in the samples were removed;
  - 3 The windows were screened by an event detector for spurious events or earthquakes;
  - 4 Each window (which passes the event detector test) was cosine tapered with a taper length of 51 samples;
  - 5 Amplitude spectra were calculated for each window using the Fast Fourier Transform technique;
  - 6 The 15 spectra were averaged together;
  - 7 The average spectrum was corrected for the instrument response to yield amplitudes with units of particle velocity;
  - 8 The average spectrum was converted into a power spectral density (PSD) which has units of  $(\mu\text{m}/\text{sec})^2/\text{Hz}$ .

A PSD for a time period is calculated by averaging together all the corresponding noise sample PSDs within the time span; all the PSDs in the summer, for example. Each PSD is displayed on log-log plots between frequencies of 0.2 Hz and 10 Hz. The instrumental output from the short-period system is very low and unreliable below 0.2 Hz (see chapter 3). The Nyquist frequency is 10 Hz and the effect of the anti-aliasing filter has been removed from the spectra for the frequencies above 5 Hz.

### 6.3 Comparison of the Average Year Noise Between the Stations in the USSN

The average noise level for the entire year is shown for the vertical components on figure 6.1. The BRG vertical and horizontal components are shown on figure 6.2. These spectra are the average of about 24000 separate spectra for each station, so the confidence limits are good. The standard deviation introduced by the averaging is displayed in figures 6.3 and 6.4 for vertical and horizontal components, respectively. For comparison purposes, the BRG vertical component spectrum has been chosen as the reference because the station is a soundly constructed vault. Figure 6.5 displays the PSD ratios between each station and BRG (the horizontal BRG components are included in this figure).

#### 6.3.1 Frequencies Between 0.2 Hz to 0.7 Hz

The peak values in the noise spectra occur between 0.2 Hz and 0.3 Hz for the three stations. The micro-seismic noise drops rapidly and is negligible above about 0.6 Hz to 0.7 Hz. The peak horizontal values are nearly a decade (20 dB) higher than the vertical at BRG (figure 6.5). BLK and BRG have similar noise levels in the band, while COM is about 2.67 times lower (-8.5 dB).

The standard deviations for the PSDs within the micro-seismic band are about half of the average values (-6 dB)

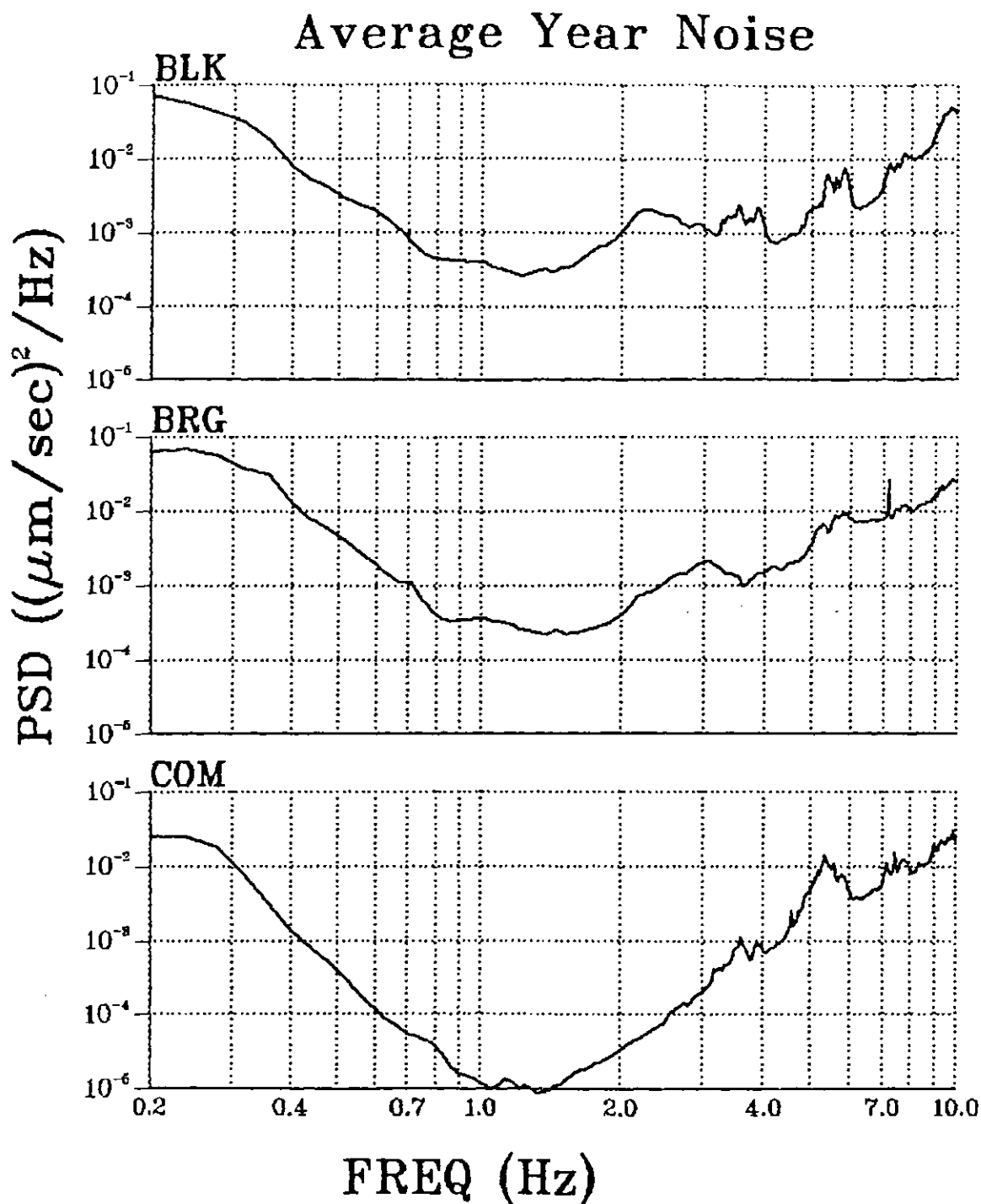


Figure 6.1. Average year noise for the USSN vertical seismometers.

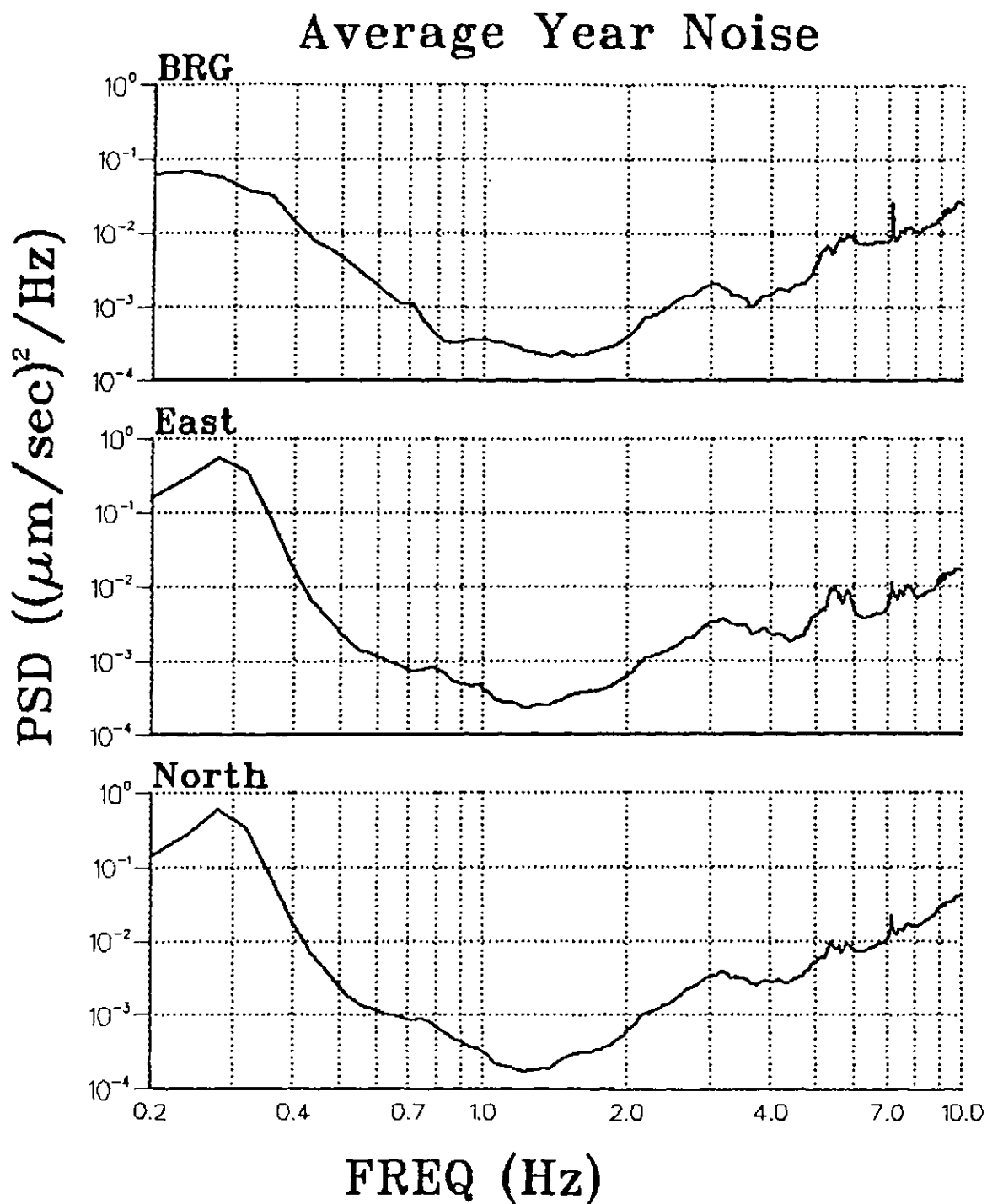


Figure 6.2. Average year noise for the USSN BRG station: vertical and horizontal components.

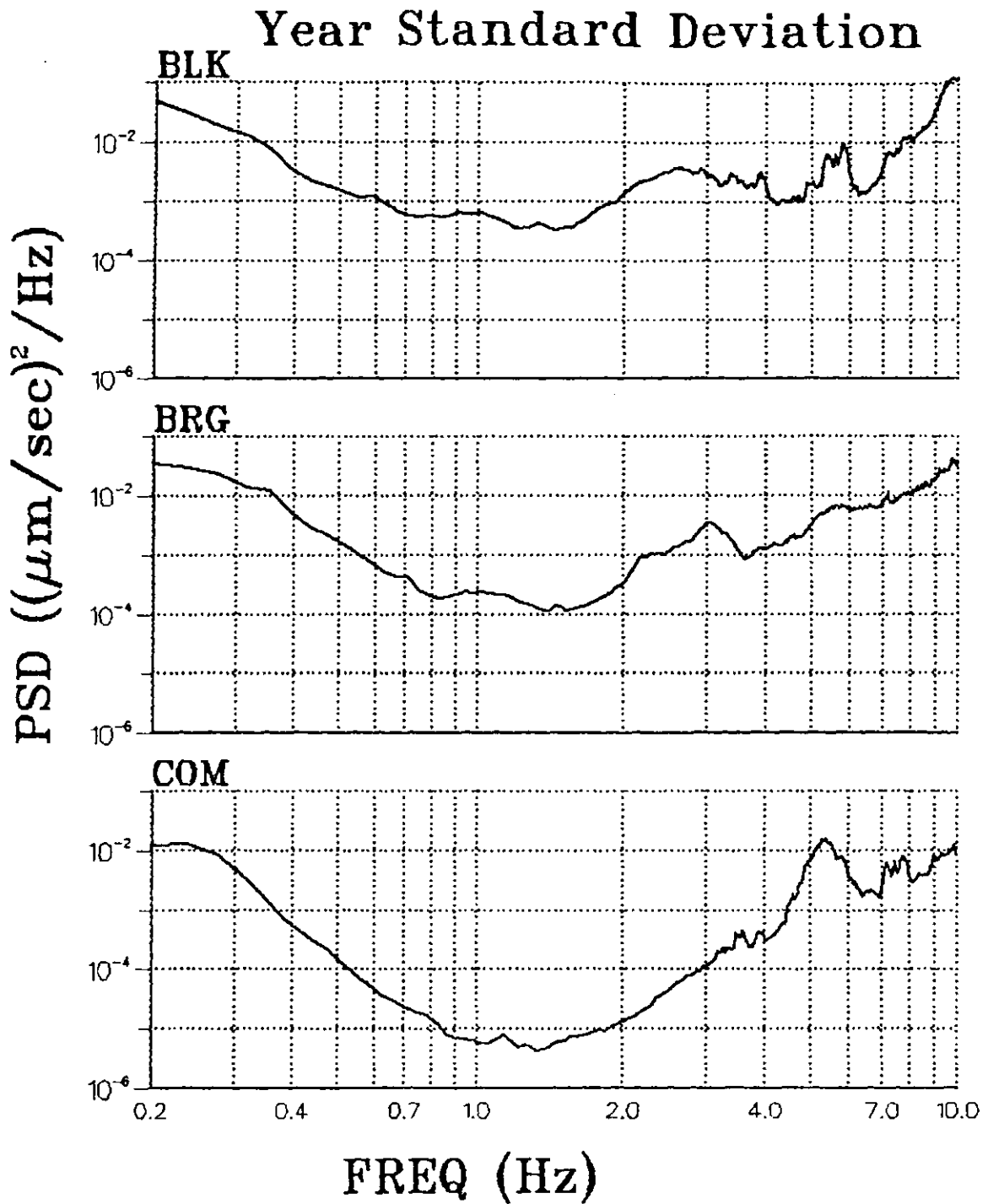


Figure 6.3. Average year standard deviation of the noise for the USSN vertical seismometers.

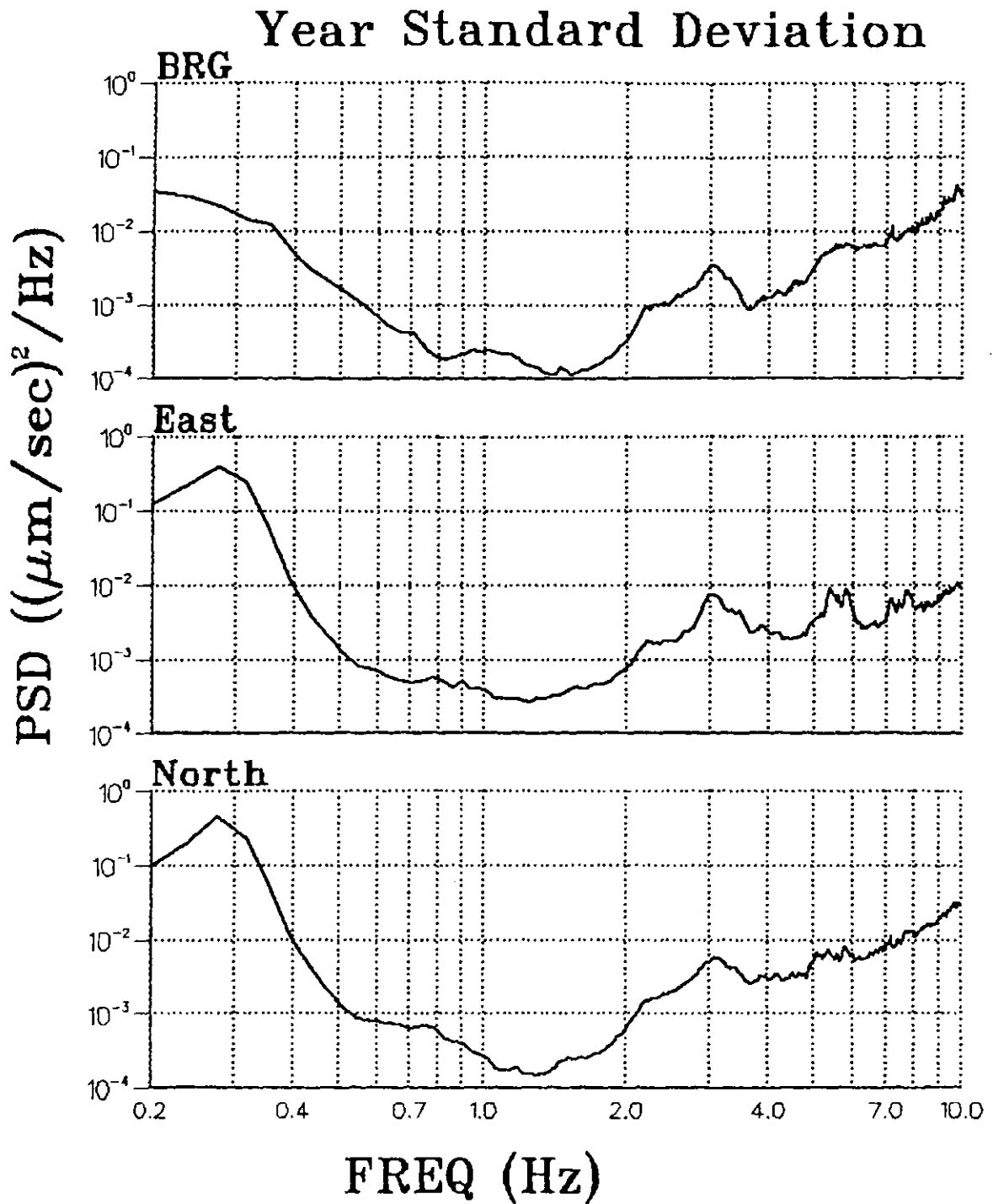


Figure 6.4. Average year standard deviation of the noise for the USSN BRG station: vertical and horizontal components.

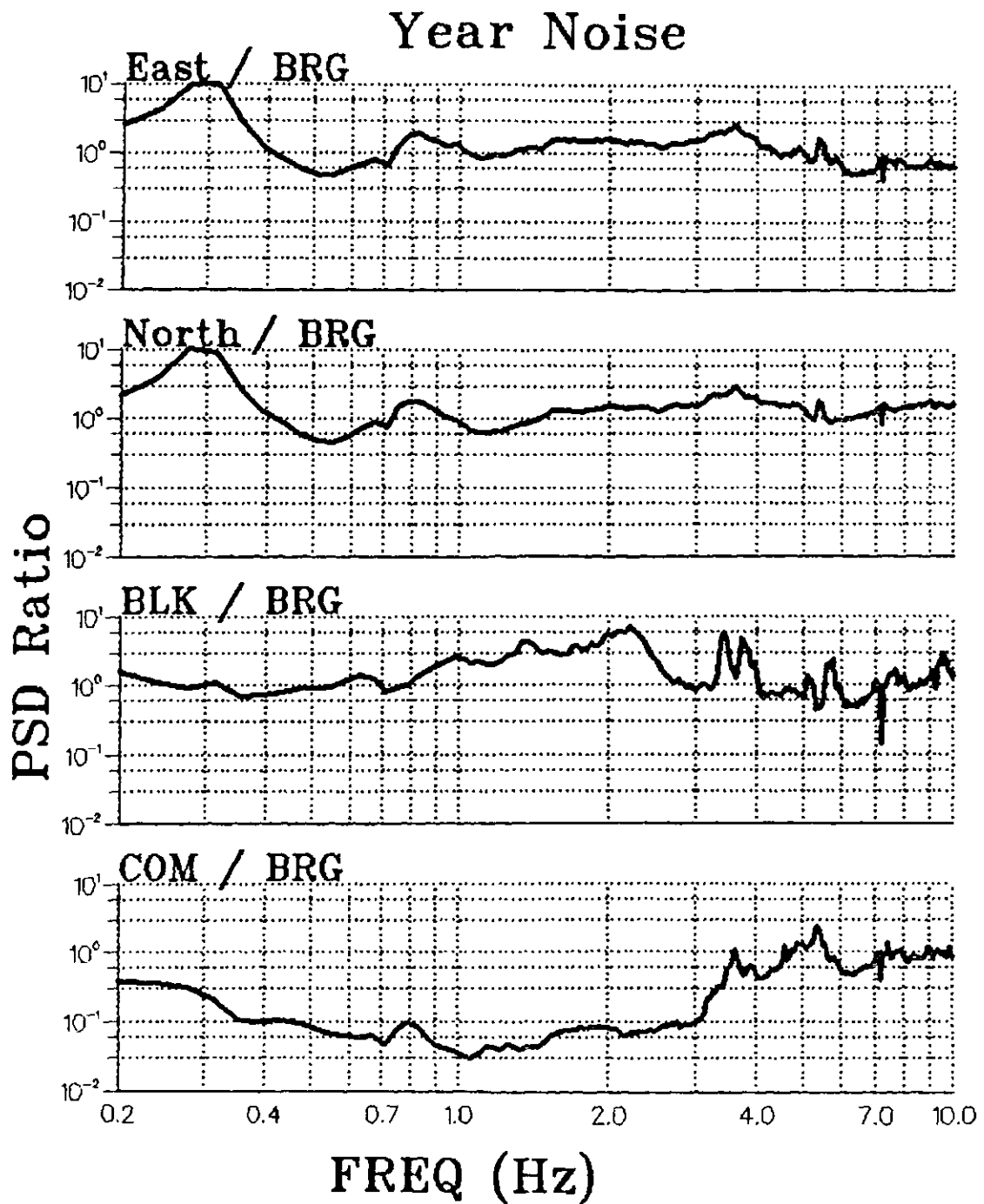


Figure 6.5. PSD ratios to BRG vertical for the year noise.

for all the stations and components. Assuming a Gaussian distribution, 68.3 percent of the data in this band fall within about -6 dB of the average PSD. The deviation is small, showing that the band noise level is fairly consistent.

### 6.3.2 The Short-Period Seismic Signal Band: 0.7 Hz to 3.5 Hz

This band shows the lowest noise levels, which is desirable because most earthquake seismograms from regional and greater distances have their peak ground velocities in this frequency band. A remarkable decrease in the noise level from the micro-seismic band of more than three decades (about -68 dB) is found at the COM site (figure 6.1). In figure 6.5, the COM PSD is found to be about a 36 times smaller (-30 dB) than the BRG vault site. The noise level at the unsheltered site (BLK) begins to exceed that of BRG at 0.8 Hz and becomes about 3 times higher (10 dB) between 1 Hz and 2 Hz (figure 6.5). The horizontal components at BRG have about the same noise levels as the vertical component in this band.

The standard deviations of the PSD between 0.7 Hz and 1.7 Hz are found to be about -4 dB of the average values at COM and BRG (figure 6.3). BLK has both the highest noise in this band and the largest standard deviations, being almost 2 dB larger than the average PSD values. This indicates

that the vault and the mine site give a more stable and lower noise background than the dirt site.

A local maximum is observed in the BLK PSD at 2.2 Hz, whereas BRG exhibits a local maximum at 3.0 Hz (figures 6.1 and 6.2). These local maxima are thought to be caused by cultural activity at the surface as COM does not exhibit a local maximum. This hypothesis is supported by the standard deviations (figure 6.3) which show an anomalous rise in the band for the surface sites, in contrast to a slow increase observed at the COM site. The frequencies most affected by cultural activity should have a large standard deviation because the phenomenon has a strong diurnal component.

#### 6.3.3 Noise from 3.5 Hz to 10 Hz

The noise for all the stations rises steadily above 3.5 Hz (figures 6.1 and 6.2). COM's noise levels are nearly as large as the surface sites at these frequencies (figure 6.5). Above 3.0 Hz, the noise at COM rises steadily to a local maximum at about 5.2 Hz. This does not agree with observations from other researchers (discussed in section 6.1). The noise may be caused by a power transformer which is close to the COM seismometer. Vibrations from continuous mining within several kilometers of the station may also be responsible for the noise.

Spurious spikes in the spectra are observed for all the stations above 4.0 Hz; the BRG component show a strong spike

just above 7.0 Hz. Similar anomalous spikes are apparent in noise data compiled from other researchers, for example: Rodgers et al., 1987; Berger et al., 1988; Given, 1990; and Carter et al., 1991. The authors attribute the spikes to seismometer or instrumental noise; or local cultural sources, such as saw mills, water pumps, or wind induced resonance of telemetry antennas. A 387 m television antenna is situated about 800 m east of the BRG vault. Windy days are common in Saskatchewan, so the antenna close to the BRG vault may be the cause of the spurious spike in the BRG spectrum.

#### 6.4 Diurnal Variations in Noise Levels

The time-of-day variations in seismic earth noise are studied using average day-time and night-time spectra. Day-time noise samples were taken during the local times of 11:00 and 15:00; and the night time samples were taken at 23:00 and 03:00. The day and night spectra are displayed as PSD ratios to the average total year spectra in figures 6.6 and 6.7, respectively. The horizontal BRG components are not displayed in these figures because they showed similar patterns to the BRG vertical component seismometer.

The most notable variations in the noise levels from day to night occur between 0.7 and 6.0 Hz at the surface. During the day the PSD for the surface stations doubles; at night, the PSDs decrease by about 4 times that of the year

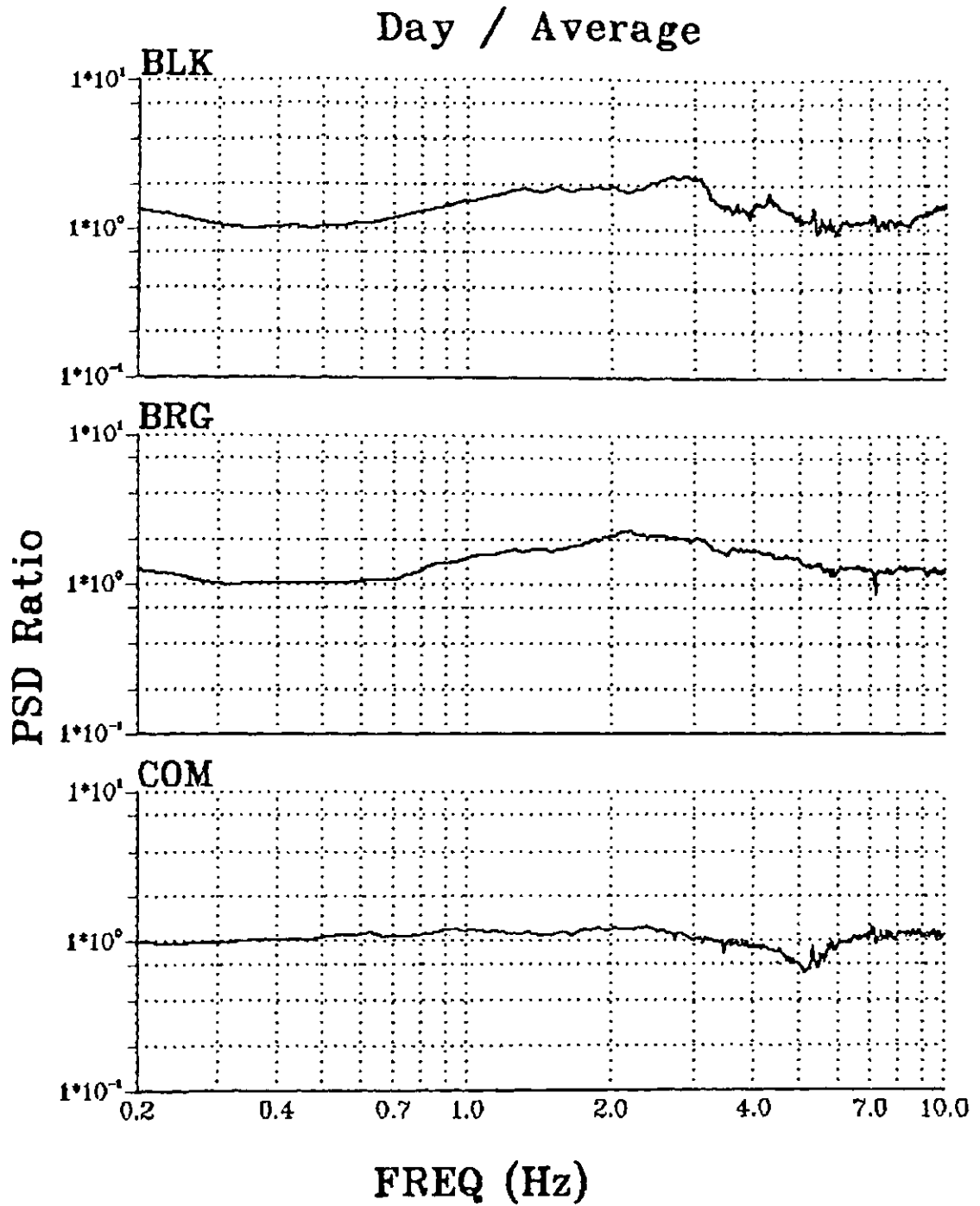


Figure 6.6. Ratio of day time PSD to year long PSD for the vertical USSN stations.

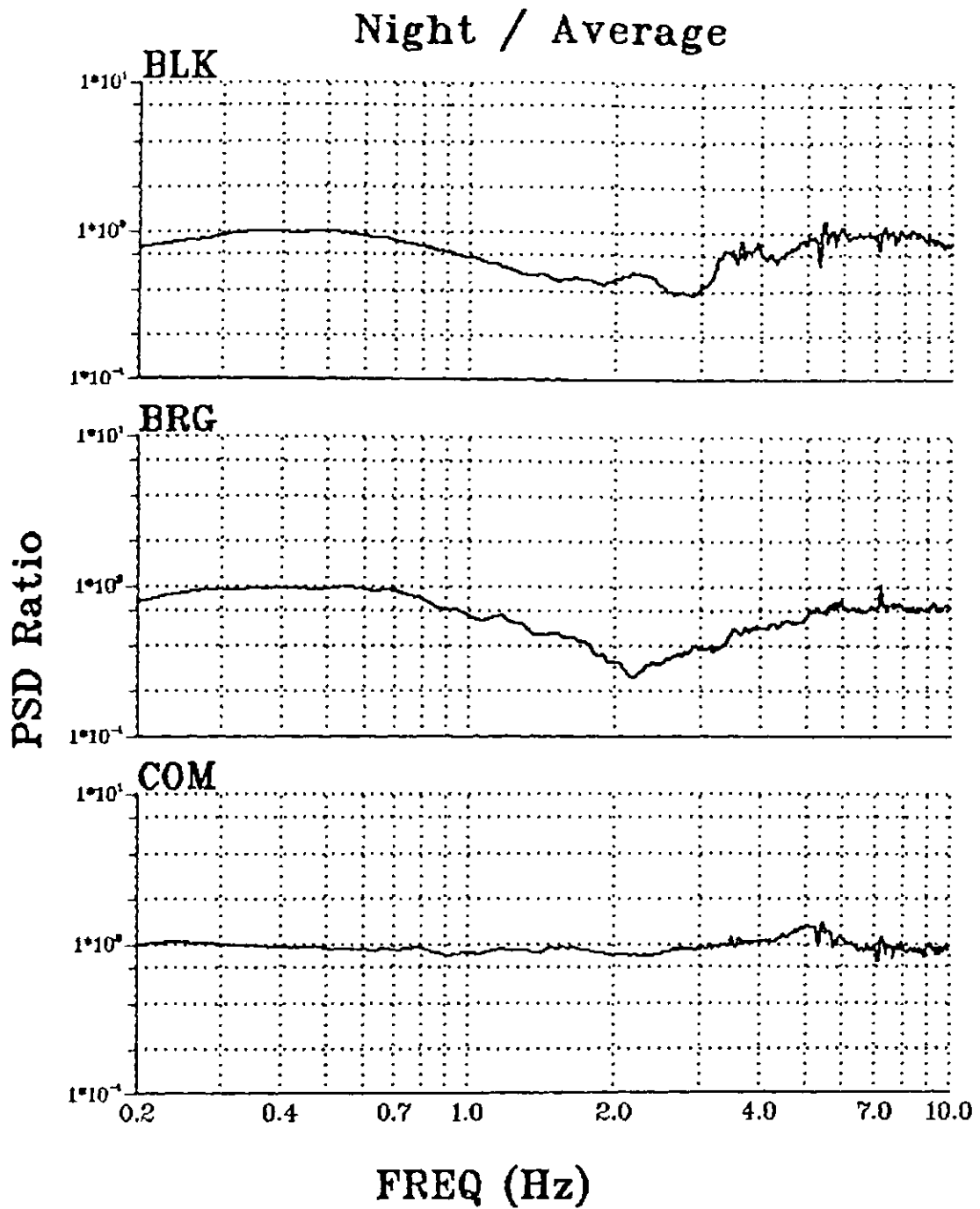


Figure 6.7. Ratio of night time PSD to year long PSD for the vertical USSN stations.

averages. The COM noise levels were found to be more stationary from day to night. An interesting diurnal variation at COM is the curious change at 5.0 Hz, the noise peaks during the night. The Cominco potash mine operates continuously, twenty-four hours a day, so the cause of COM's diurnal change in PSD around 5 Hz is not known. Generally though, the observations here are consistent with cultural seismic earth noise observed by others (eg., Given, 1990).

#### 6.5 Seasonal Variations in Noise

Summer and winter noise levels are compared to the average year noise levels in figures 6.8 and 6.9 respectively. Each seasonal spectrum was obtained by averaging three month periods: June to August and December to February. Again, the BRG horizontal components are not displayed as they show little difference from the vertical spectral changes.

In the micro-seismic band, the increase in noise is much less than changes observed in other parts of the world. This is most likely a result of the array location within the central part of North America. The most notable decreases in noise occur in the winter for BLK and BRG between 0.7 and 10 Hz. Some portions of the BLK PSD's are nearly 10 times smaller in the winter. The reduction in noise during the winter may be due to a quiescence of farming activity. There are many farms in the areas close

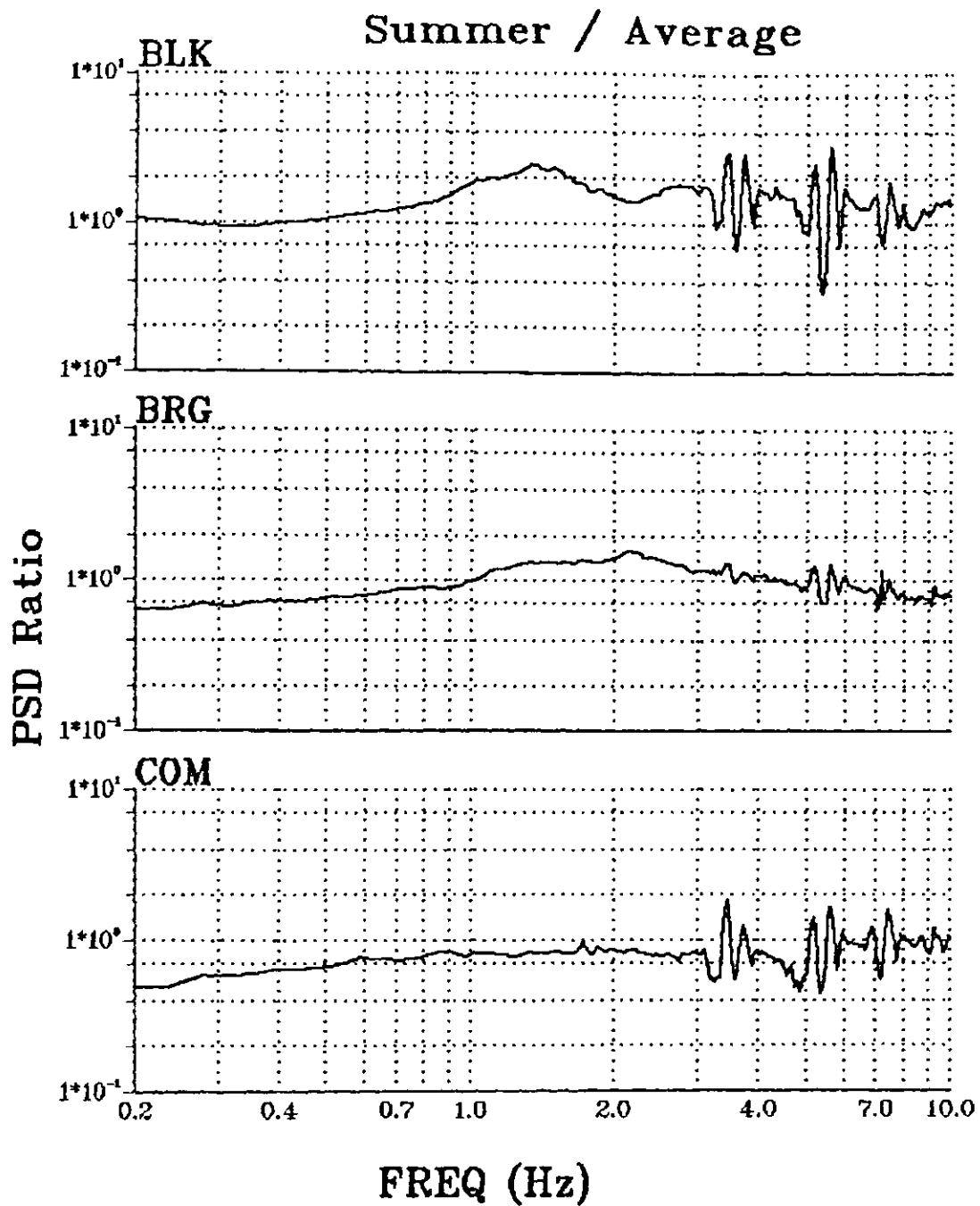


Figure 6.8. Ratio of summer time PSD to year long PSD for the vertical USSN stations.

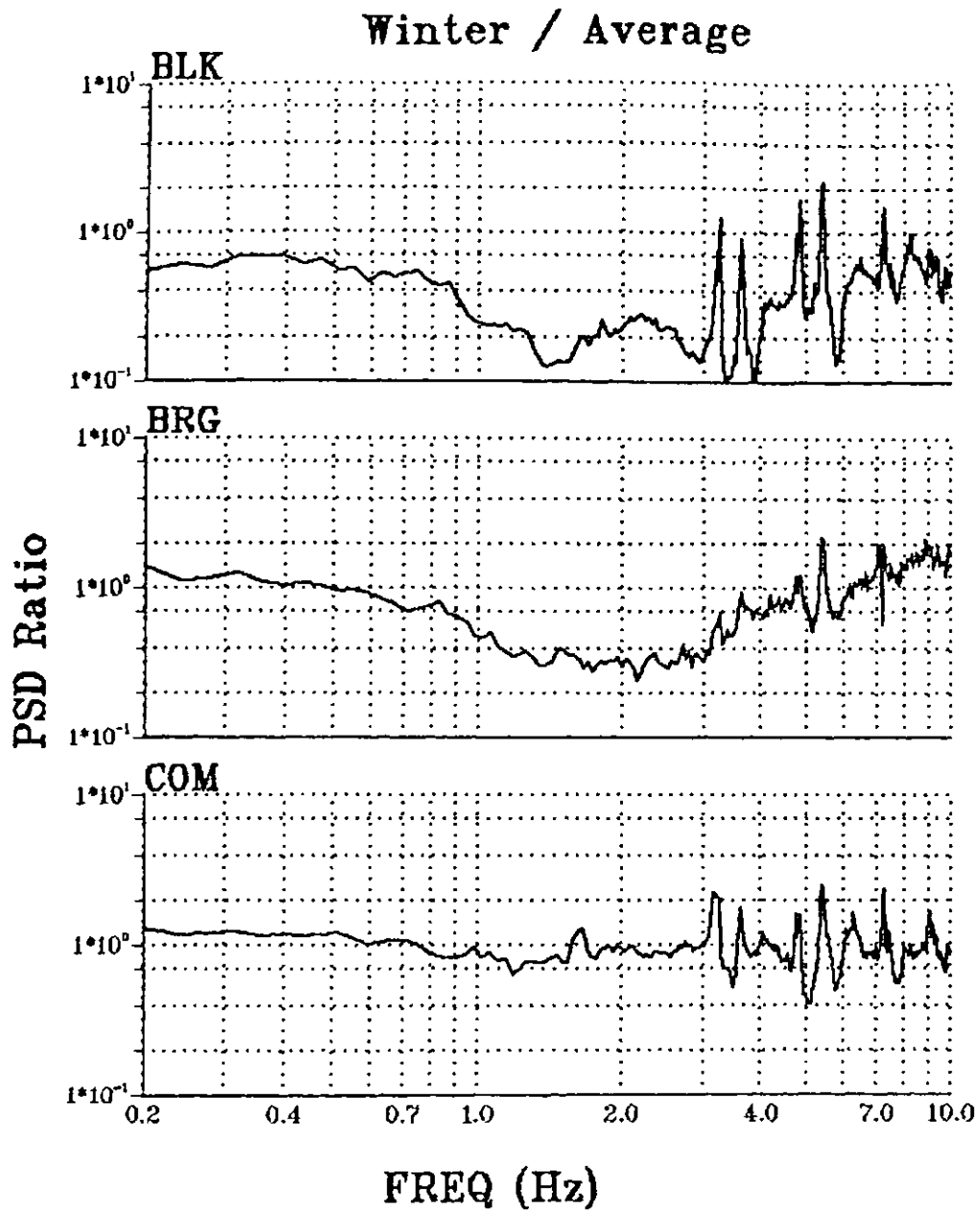


Figure 6.9. Ratio of winter time PSD to year long PSD for the vertical USSN stations.

to the USSN stations. Also, the frozen ground in the winter is probably more stable than in the summer. This effect is pronounced at BLK (a dirt site) where the seismometer becomes firmly frozen into the ground.

The Cominco mine was closed for four weeks in the summer, during the experiment. The summer noise at COM shows a slight decrease which is probably related to the shut-down at the mine. An ideal time period for recording earthquakes in Saskatchewan is in the winter, at night, for surface stations. The mine site is essentially immune to time-of-day or seasonal changes.

#### 6.6 An Example of the Effect of Wind on Seismic Noise

A particularly windy day was chosen to examine the effect of wind on USSN seismic noise. The wind velocities were obtained from the Saskatoon airport, which is located on the northern edge of the city. The velocities may not correspond exactly to the conditions at the stations, but are probably close since the weather system was widespread. Three noise samples are displayed for each station; each sample corresponds to an increase in velocity. The samples are displayed as PSD ratios to average spectra for the season. The BRG vertical and the two horizontal spectra are displayed on figures 6.10 through 6.12; the BLK spectra are displayed in figure 6.13. Each spectrum is labeled with its corresponding time period and the average to peak wind

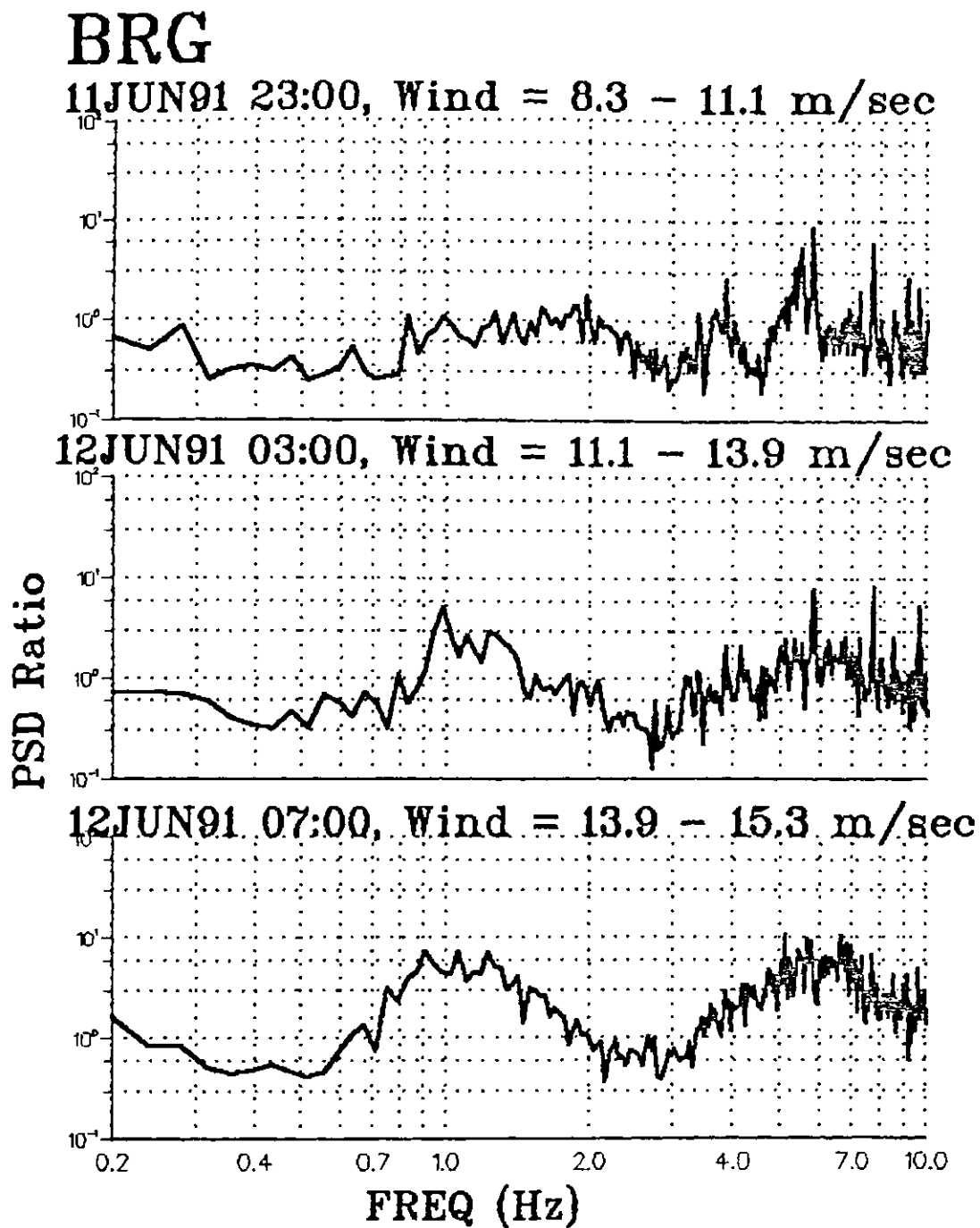


Figure 6.10. PSD ratios to seasonal average for the BRG vertical seismometer during a windy day.

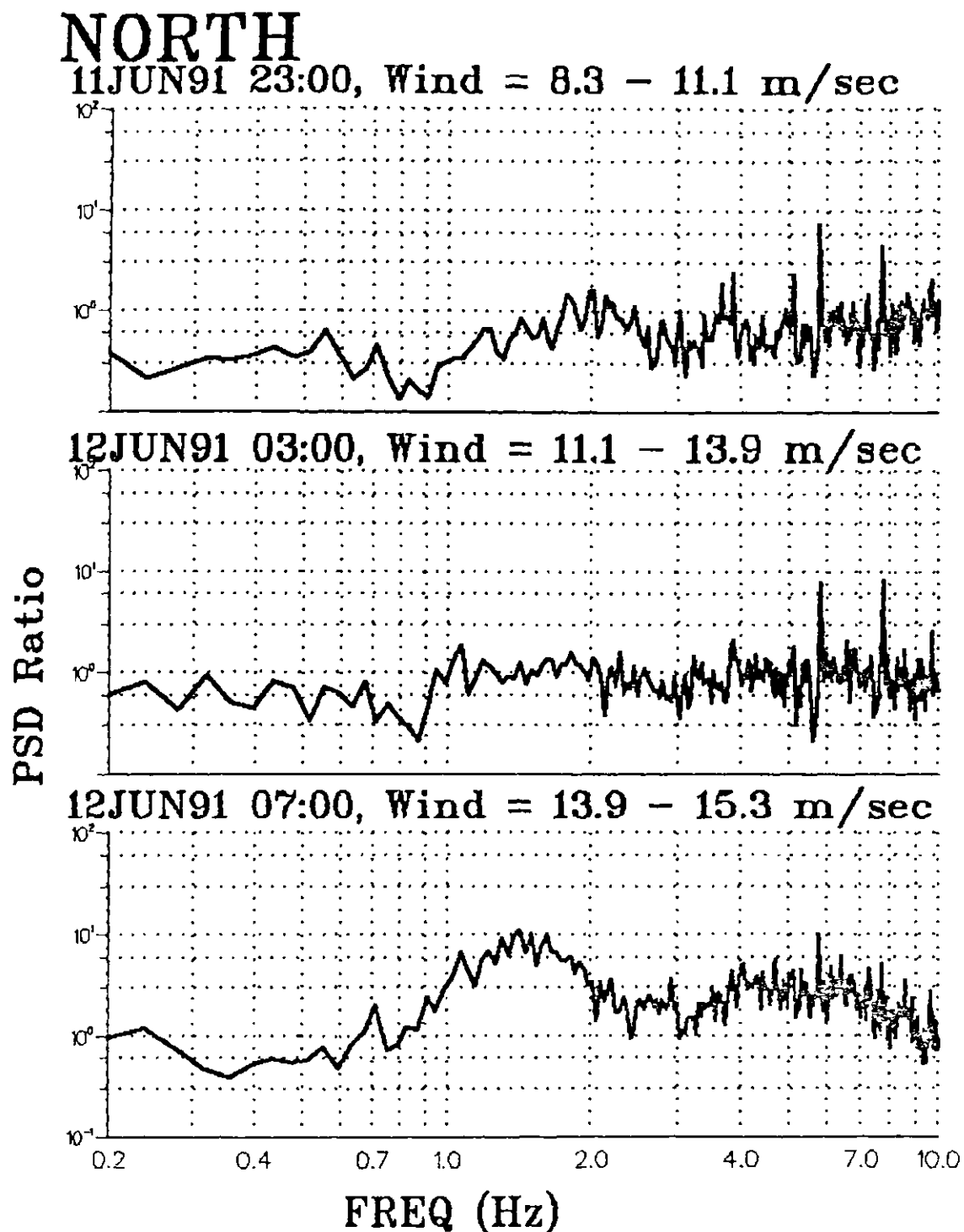


Figure 6.11. PSD ratios to seasonal average for the BRC north seismometer during a windy day.

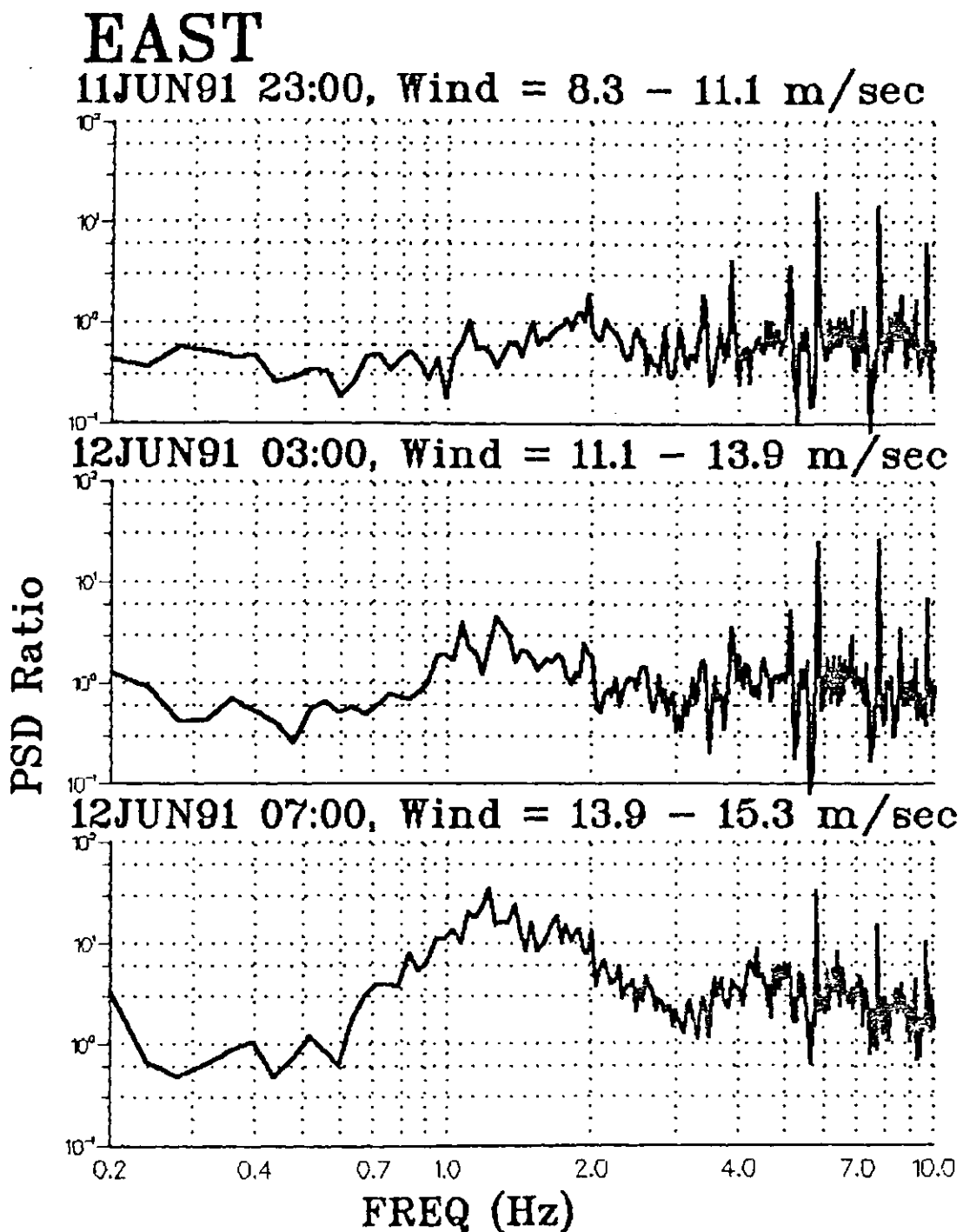


Figure 6.12. PSD ratios to seasonal average for the BRG east seismometer during a windy day.

# BLK

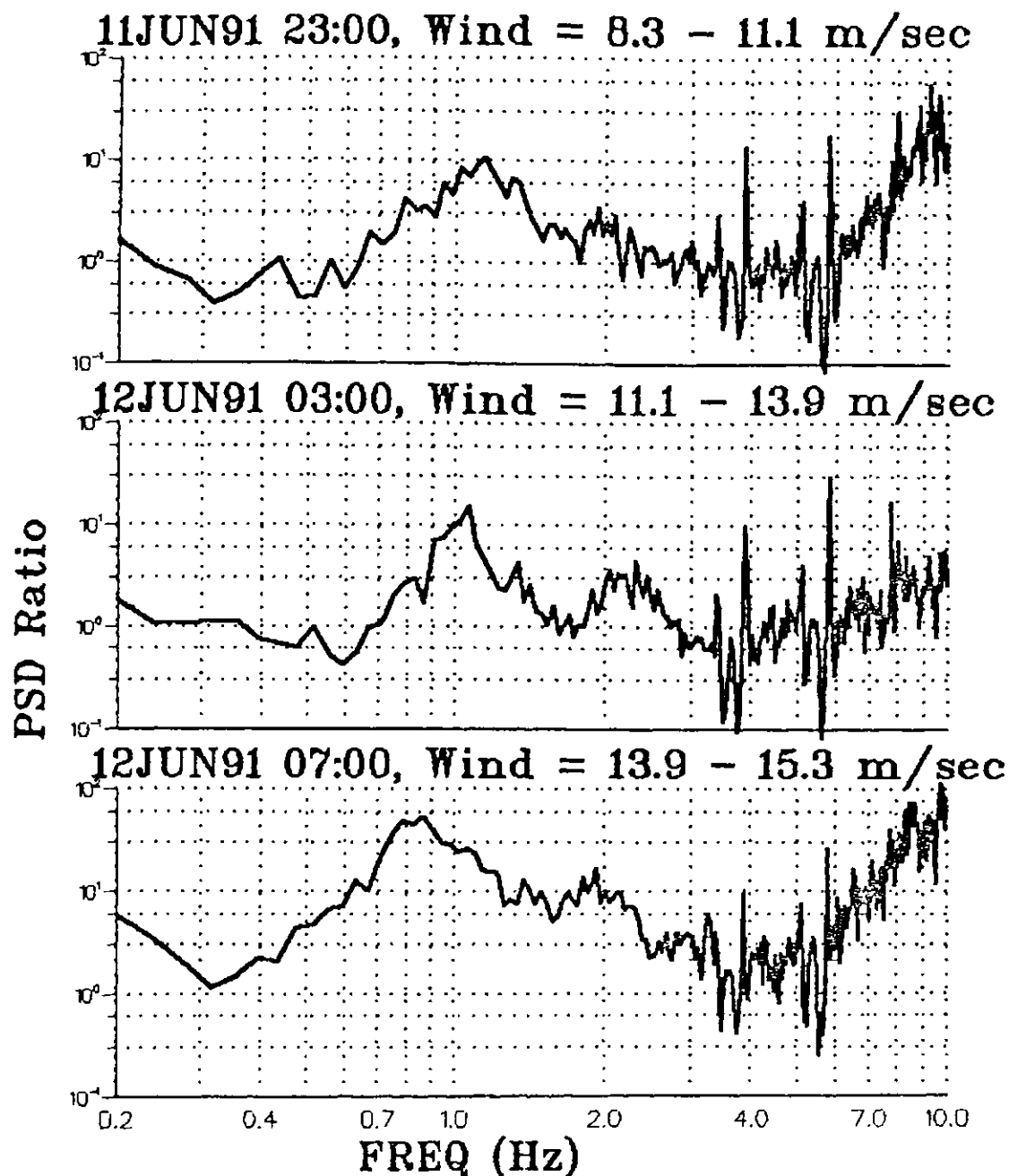


Figure 6.13. PSD ratios to seasonal average for the BLK vertical seismometer during a windy day.

velocity during the time period. COM spectra are not given because the mine site shows no changes with wind velocity.

The most notably affected station is BLK, showing a PSD 50 times larger (34 dB) than the average for June at a mean wind velocity of 13.9 m/sec. BRG's maximum increase on the vertical component was about 7 times (17 dB) the normal seasonal level. The horizontals show larger changes: the PSD for the east component increased about 12 times (21.5 dB).

In this example, the wind has little influence on the PSD for frequencies below about 0.7 Hz. At BRG two peaks are evident in the noise spectra: one at about 1 Hz and another around 6 to 7 Hz. At BLK, the spectra also peak around 1 Hz but the spectra have a broader shape. The changes in the higher frequencies (above 5 Hz) at BLK may not be exclusively related to the wind. During the time period, some road construction was underway close to the site which created considerable high frequency noise.

The vault proves to be successful in reducing the affect of wind on seismic noise. The spectra show only a small increase in noise even for wind speeds as high as 11 m/sec. In contrast, the dirt site (BLK) shows a steady increase in PSD with wind velocity. The COM site is completely exempt from wind noise.

## 6.7 Magnitude Threshold: a Comparison of Station Data Quality

The ambient seismic noise at the stations controls their event magnitude threshold as a function of distance. This study has shown that the seismic noise can be extremely variable, so magnitude sensitivities will vary from day to day. The main focus of this section is to establish average thresholds for each station; and study diurnal and seasonal threshold variations. Such a study has implications on station quality, since the locations with the quietest and most stationary ambient noise will have the lowest magnitude threshold.

### 6.7.1 Calculating the Threshold Functions

The thresholds are calculated via Nuttli's magnitude relationship (Nuttli, 1973):

$$M_N = -0.10 + 1.66(\log\Delta) + \log(A/2\pi), \quad 6.1$$

where:  $M_N$  is Nuttli magnitude,

$\Delta$  is epicentral distance in kilometers,

$A$  is the 1 Hz zero to peak maximum trace

amplitude of the  $L_g$  phase, in units of micrometers per second.

Nuttli's scale is valid for earthquakes in eastern North America, when distances are between about 400 Km and 3000 Km. The relationship has proven successful for events recorded by the USSN.

The amplitude ( $A$  in eq. 6.1) was estimated from the PSD functions for the USSN stations. The PSD at 1 Hz is readily converted to average trace amplitude by Parseval's theorem. To establish the possible range of the ambient earth noise, two standard deviations are added to the average value. Minimum amplitude needed for detection is then defined as four times the background amplitude. The requirement is notably conservative, as events with smaller S/N at the  $L_g$  phase have been detected by the system. However the criterion was set to ensure that all phase arrivals within the coda can be accurately discerned.

The COM mine site station poses a problem for the minimum detectability as peak trace amplitudes for the  $L_g$  phases are smaller on the seismograms. Hauksson et al. (1987) report a similar experience with vertically incident P and S waves where they found the amplitudes to be four and nine times smaller, respectively, at a depth of 1500 m. There has been no formal study here on the phenomenon, but based on personal experience with the system, peak  $L_g$  phases tend to be about four times smaller on the COM seismograms when compared to the surface recordings. The requirement for minimum detectability at the COM site has been defined as sixteen times that of the background noise level, in

order to make the station equivalent to the surface sites.

#### 6.7.2 USSN Station's Magnitude Thresholds

Station magnitude threshold functions are displayed for the day, night, summer, and winter in figures 6.14 through 6.17 respectively. Each function displays the three USSN station thresholds for the period. Notably, COM has the lowest threshold of the USSN stations, for all time periods, averaging about half a magnitude unit more sensitive. Recall that the COM threshold is defined as sixteen times the background noise level rather than four for the surface stations. The plots emphasise the very low background noise level at the COM site. BLK averages about 0.2 units greater than BRG.

The thresholds show subtle diurnal and seasonal changes. The logarithms in the magnitude scale (eq. 6.1) make the relationship fairly insensitive to changes in amplitude. BLK shows changes in amplitude of 35 percent between summer and winter. This translates to a decrease of 0.2 magnitude units, from summer to winter. The amplitude changes for BRG are small, making changes in magnitude threshold almost negligible with time. The COM threshold is essentially constant.

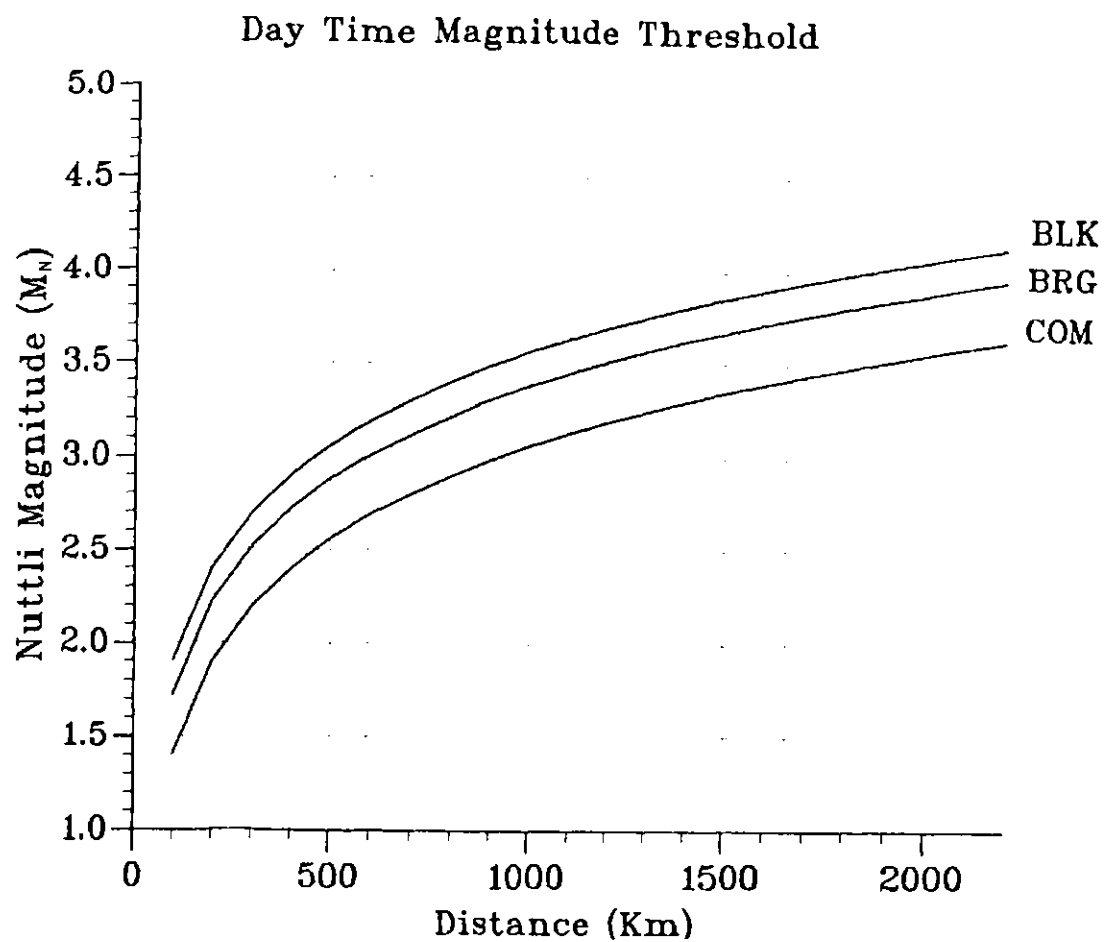


Figure 6.14. Day time magnitude threshold as a function of distance.

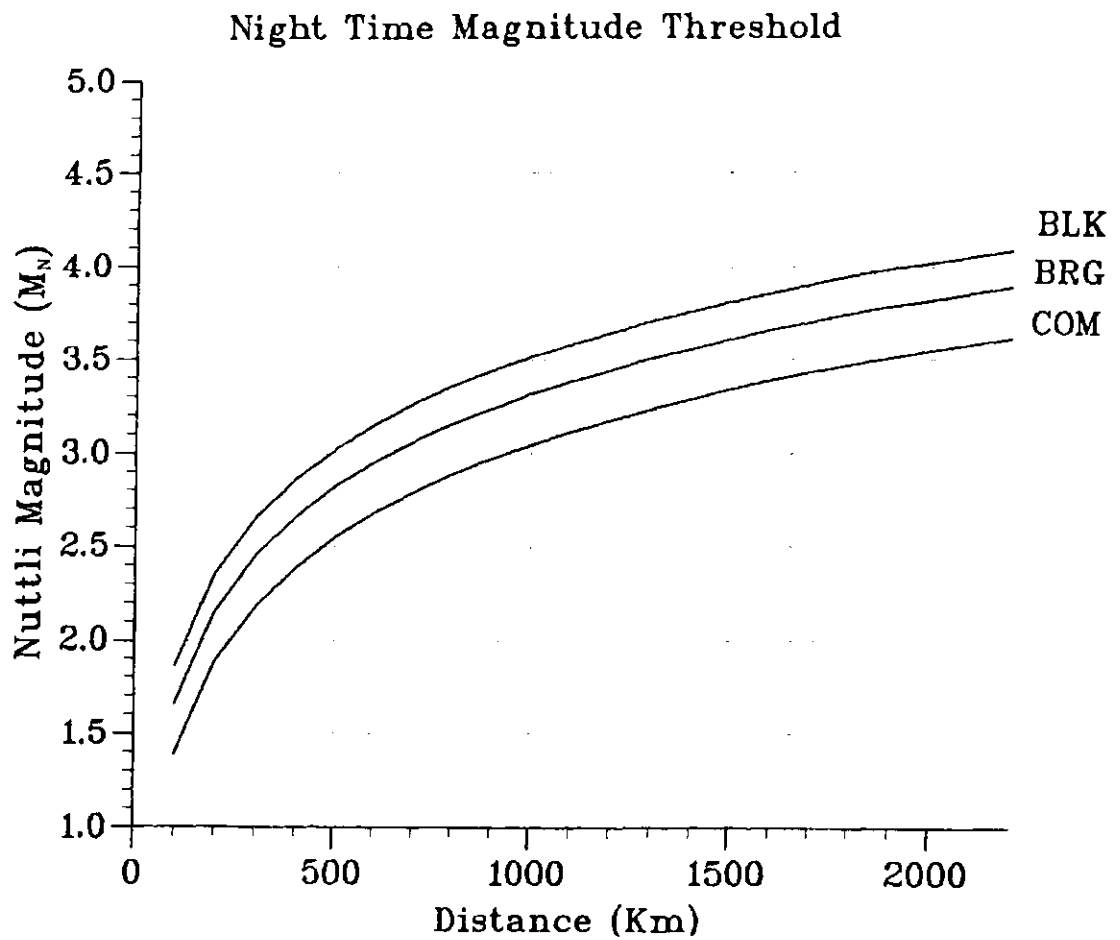


Figure 6.15. Night time magnitude threshold as a function of distance.

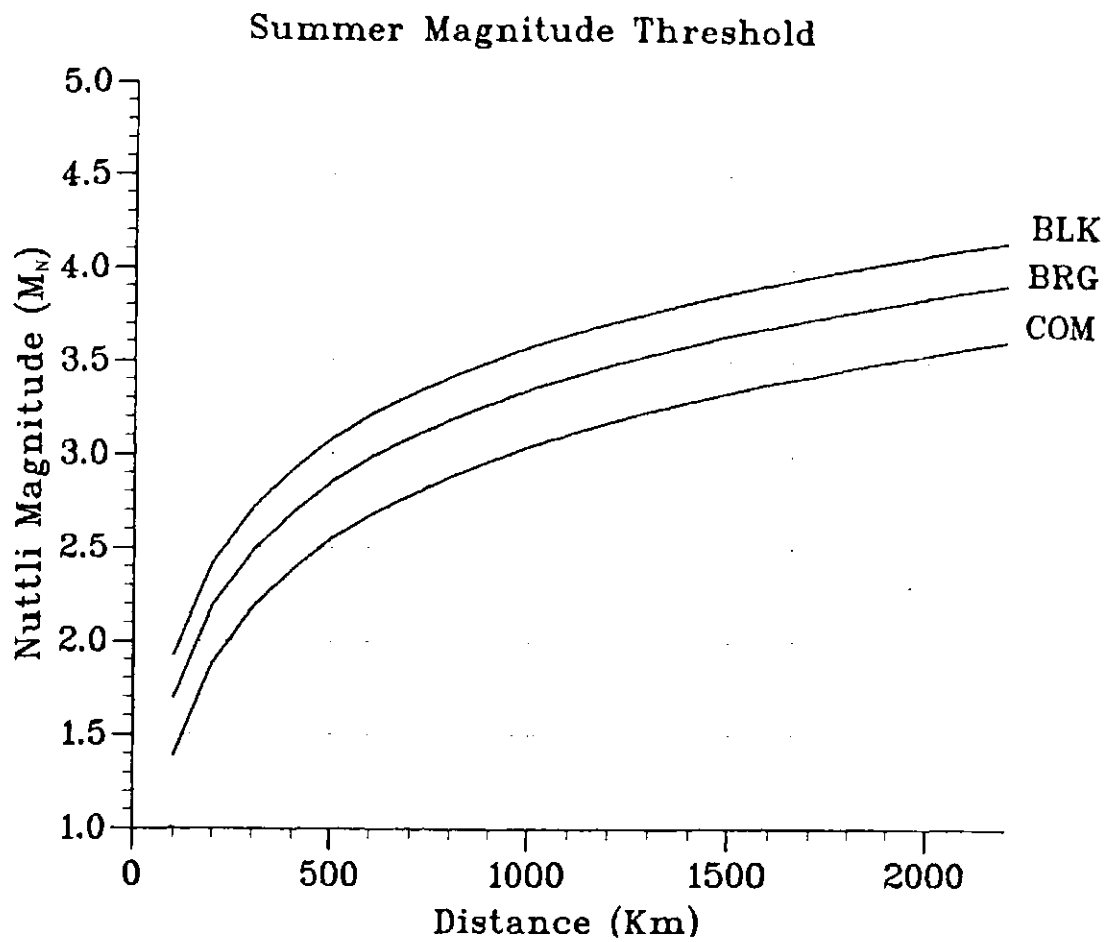


Figure 6.16. Summer time magnitude threshold as a function of distance.

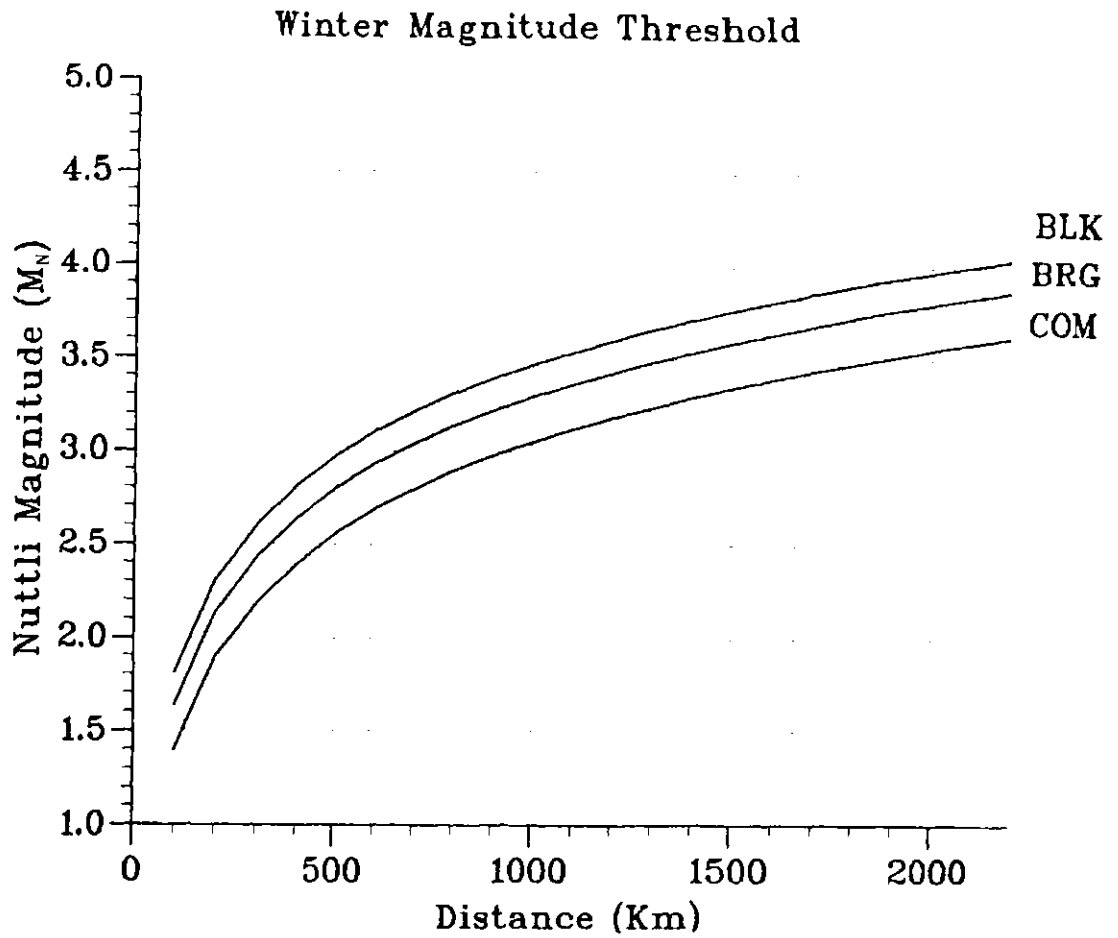


Figure 6.17. Winter time magnitude threshold as a function of distance.

### 6.7.3 USSN Station's Magnitude Dynamic Ranges

The dynamic range of the ground motions at the stations have been investigated by calculating the maximum magnitude that can be recorded as a function of distance. The results are shown for various gain levels for surface stations on figure 6.18. Obviously, the seismometers can record any event over their threshold; however, the peak ground motions that can be recorded without distortion are limited. The voltage controlled oscillator (VCO) in the instrumentation is the limiting component and can only pass a maximum of about 5 V (peak-to-peak) from the amplifiers. Based on calibration experiments at 78 dB gain, the maximum ground velocities that can be recorded without distortion (clipping), around 1 Hz, are 4  $\mu\text{m}/\text{sec}$ . The peak ground motions at other gain levels are readily obtained assuming linearity of the instrumental components.

COM will invariably have the highest dynamic range of the USSN stations because of its low threshold and reduction of surface wave amplitude with depth. The dynamic ranges at 78 dB gain are about 24 dB for BLK, 27.5 dB for BRG, and 44.6 dB for COM. While at 66 dB gain, the dynamic ranges are 36 dB for BLK, 40 dB for BRG and 56.6 dB for COM. One can see that a low magnitude threshold is desirable both for good sensitivity and dynamic range.

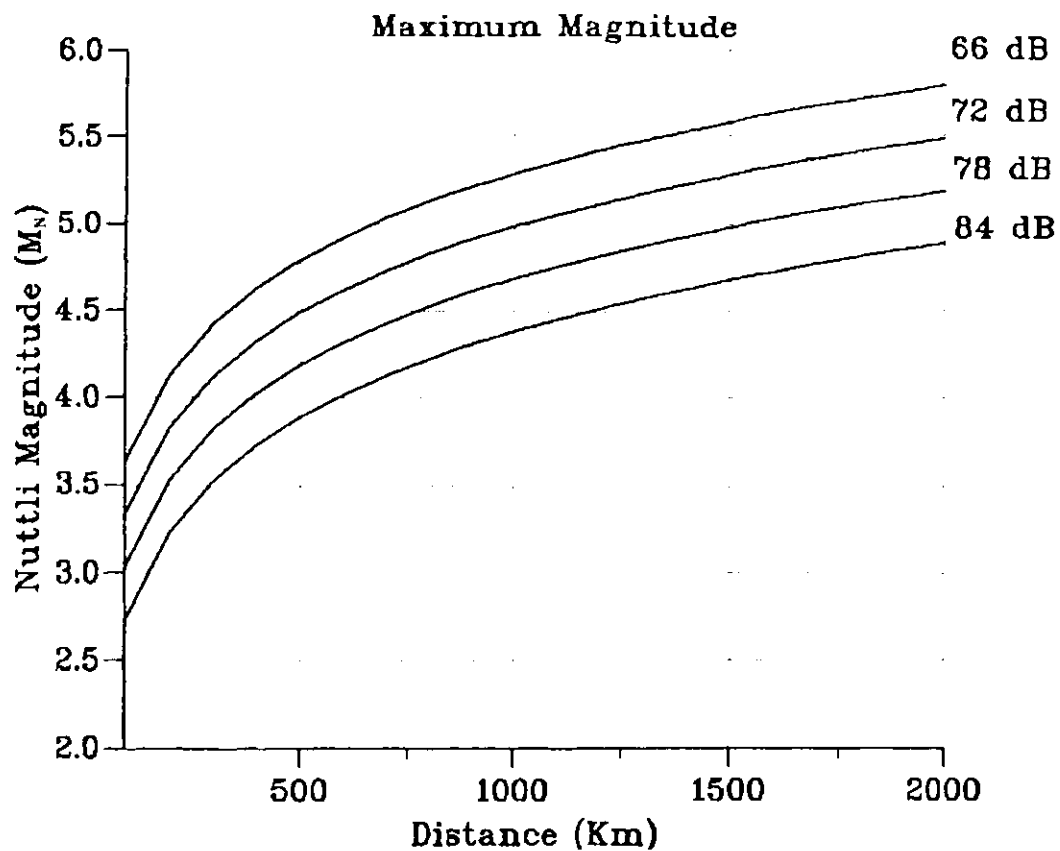


Figure 6.18. Maximum magnitude capability of the USSN as a function of distance (for surface stations).

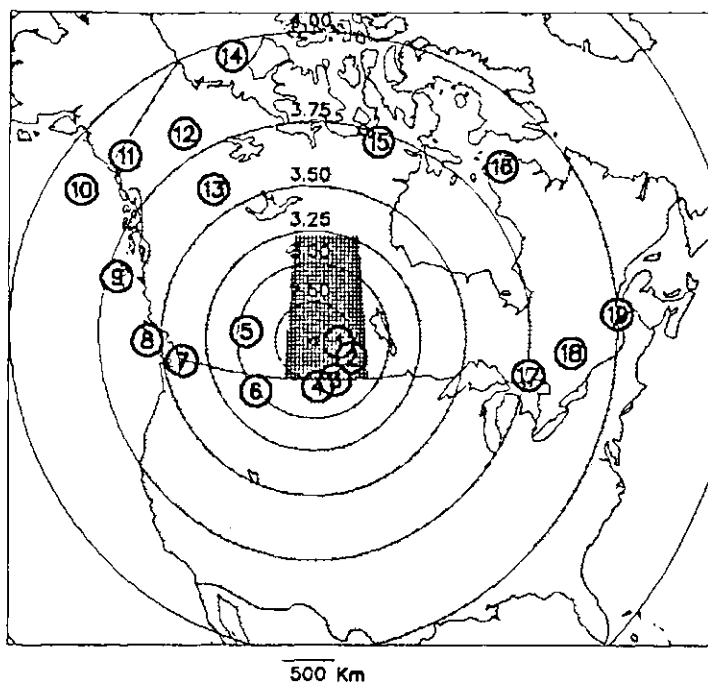
## 6.8 Noise Study Summary

The magnitude threshold and maximum event size is summarised in figure 6.19. The maps shows contours of Nuttli magnitude in relation to areas in Canada that have had earthquakes in the past. The threshold map is an average of the surface station sensitivity. The maximum event size map is for an instrumental gain setting of 78 dB. The latter shows that the present USSN gain levels would clip seismograms from a magnitude  $5\frac{1}{2}$  event like the one that occurred in southern Saskatchewan in 1909.

The magnitude threshold functions for the USSN stations are strong indicators of relative station quality. The study has shown that a deep mine site can improve event magnitude threshold by as much as  $0.5 M_N$  units in comparison to surface sites. The study also shows the impact of the surface vault on data quality. For winter, the average noise amplitude at 1 Hz for the open site is actually lower than the vault; however, the magnitude threshold at the dirt site is worse because of the large standard deviation. The findings are similar to Given (1990), who states that "a good vault cannot eliminate cultural noise, but becomes essential in reducing its impact."

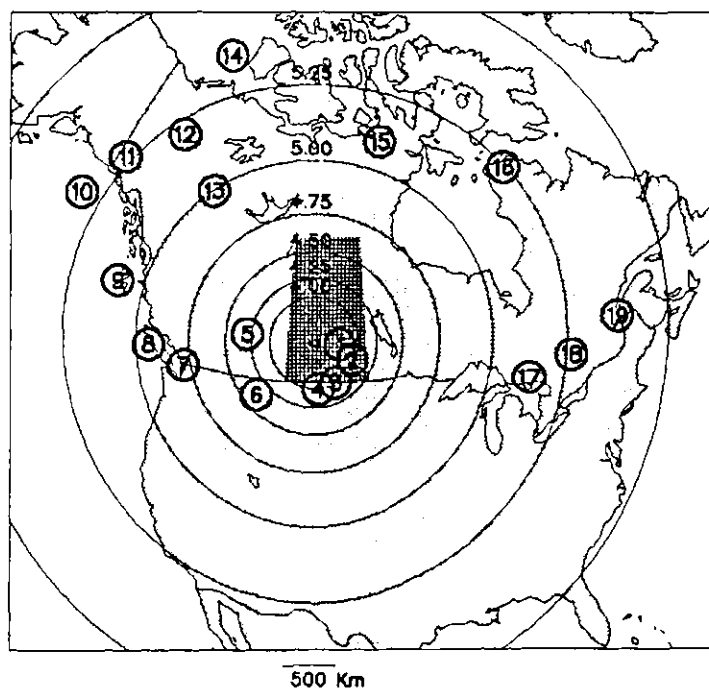
## Recording Capability of the US Seismograph Array

### Minimum Surface Station Threshold



- 1 - Kuroki, Sask.
- 2 - Esterhazy, Sask.
- 3 - Largest Sask Event
- 4 - Montana
- 5 - Rocky Mountain House, Alta.
- 6 - Montana
- 7 - Washington State
- 8 - Vancouver Isl.
- 9 - Queen Charlotte Isl.

### Maximum Event Size



- 10 - Gulf of Alaska
- 11 - St Elias MTNS, Yukon
- 12 - Mackenzie, MTNS, NWT
- 13 - Nahanni, NWT
- 14 - Beaufort Sea
- 15 - Chantry Inlet, NWT
- 16 - Northern Quebec
- 17 - Sudbury Basin, Ont.
- 18 - Western Quebec
- 19 - Charlevoix Quebec

Figure 6.19. Maps showing magnitude threshold and maximum event size. The maximum event size map is based on an instrumental gain of 78 dB.

## CHAPTER 7

STUDY OF THE CRUST USING EARTHQUAKES

Earthquake seismograms are valuable for studying the earth's crust. There have been no such studies in the Saskatoon area to date. Deep seismic refraction (explosive source) surveys have been conducted in Southern Saskatchewan. The derived models may be inappropriate for this area since the crust in southern Saskatchewan is thought to be very complex. In this chapter the crust in the Saskatoon area is investigated using local, regional and teleseismic seismograms. The regional data provide earthquake phase velocities and a depth to the upper mantle. From the teleseismic data, one can infer a complex crustal structure in the area because of variable time delays found in the first P phase arrivals at the different stations. Finally, seismograms made from an interesting local earthquake strongly imply the presence of a significant refracting discontinuity within the crust. The analysis of the P-wave refractions will show that the horizon may have a significant dip.

## 7.1 Devising a Crustal Model for the Saskatoon Area

Southern Saskatchewan is situated over the northern flank of the Williston Basin. At Saskatoon the Phanerozoic

sedimentary sequence has a thickness of about 1700 m, which increases to nearly 3200 m in the southern portion of the province. The sequence consists of approximately 600 m of sands and shales overlying more than 800 m of carbonates and evaporites. The bottom of the sequence consists of some 300 m of sand which rest unconformably on the Precambrian surface (Christopher et al. 1971). A generalized geological section of the stratigraphy around Saskatoon is shown in figure 7.1; note the position of the potash mining zone in this figure.

The seismic P-wave velocity model for the sediments on figure 7.1 has been derived from sonic logs in the area. The model is a simplified description of the actual velocities. A two layer approximation of the sedimentary section is adequate because the change in velocity at about 600 m is the largest transition in the sedimentary section. The structural dip on this velocity transition amounts to no more than 1.8 m/km (derived from Christopher et al., 1971; Simpson and Dennison, 1975).

A structure contour map of the Precambrian basement in the Williston Basin area is shown in figure 7.2. The basement is known to be geologically complex throughout the province. The regional structure is essentially a large dipping plane (although structures of diastrophic origin exist in both the Precambrian and Phanerozoic). The dip of the basement in the Saskatoon area is about 4.8 m/km. Also shown on figure 7.2 are several positive gravity features in

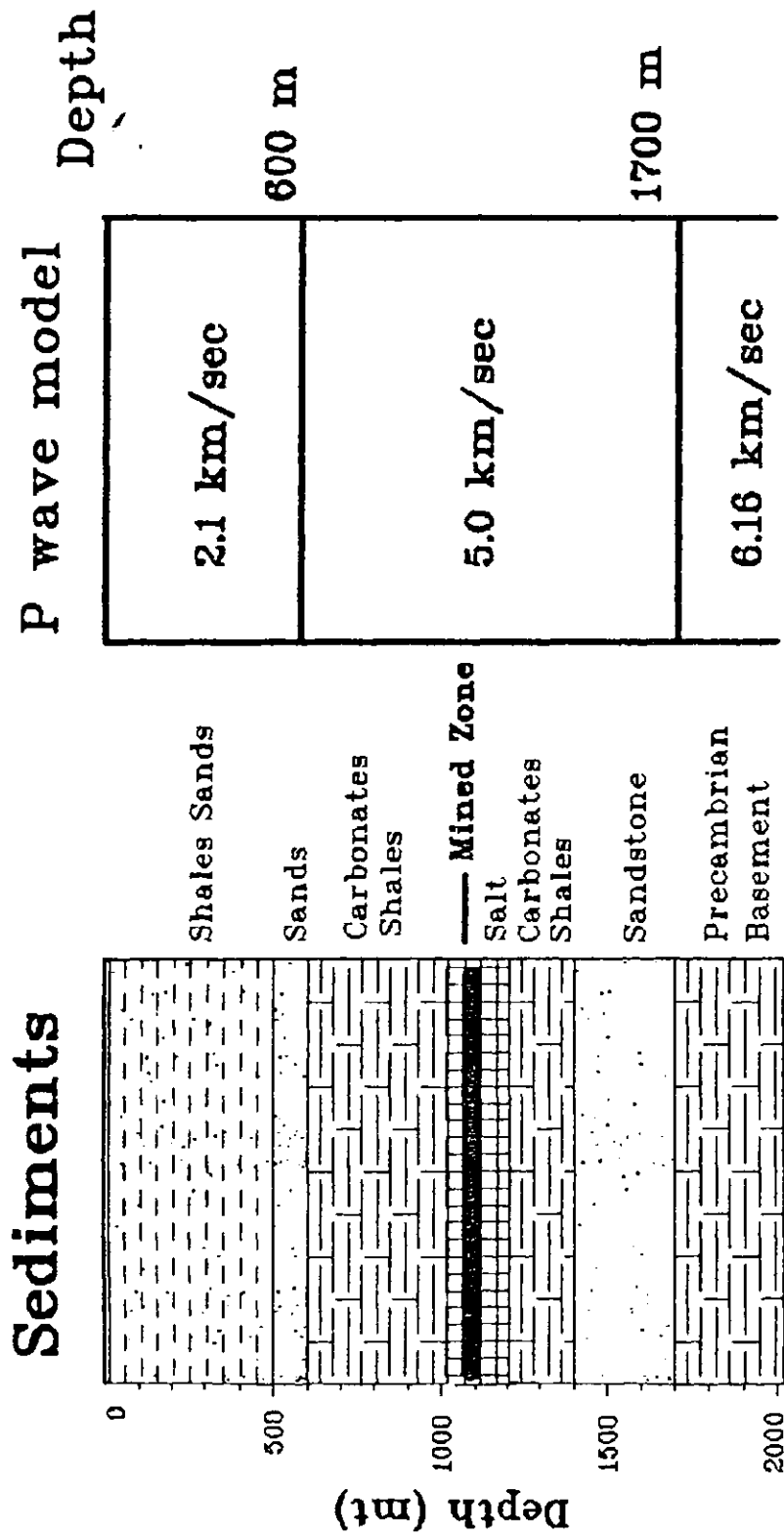


Figure 7.1. Generalized geological section and P wave velocity model.

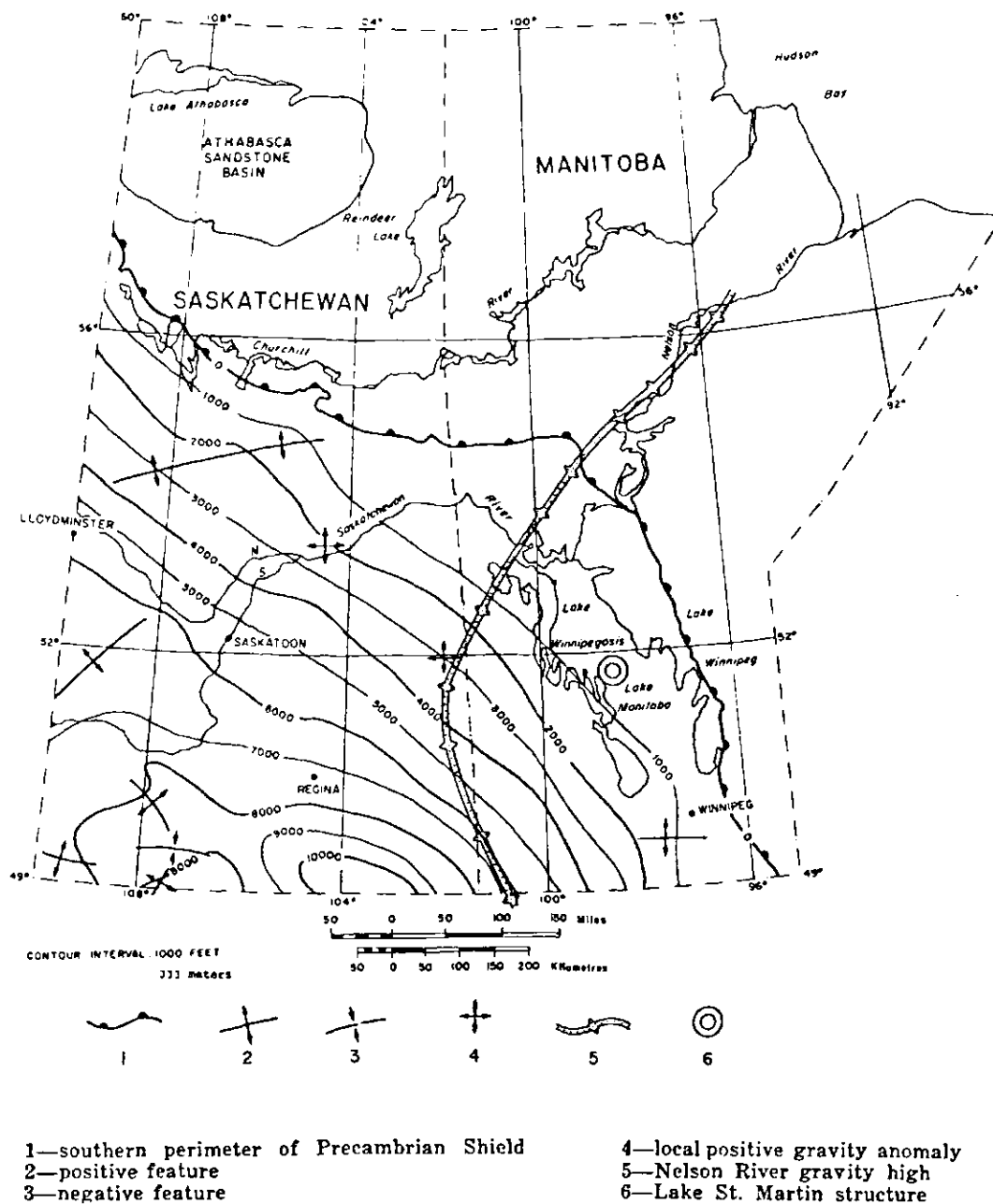


Figure 7.2. Depth of Precambrian basement below surface (from Simpson and Dennison, 1975).

the area (Christopher et al., 1971; Simpson and Dennison, 1975; Thomas, 1974; Kent, 1973).

To date, there have been no crustal seismic studies in the Saskatoon area. However, a crustal velocity model can be estimated from deep crustal refraction surveys conducted several hundred kilometers to the south of the USSN. The experiments consisted of eight reversed refraction and some broadside refraction profiles (discussed by Green, 1980; Hajnal et al., 1984; Morel-A-L'Huissier et al., 1987; Kanasewich et al., 1987). A crustal profile (from Hajnal et al., 1984) in figure 7.3 reveals the complex nature of the crust. Recently, Zhu (1992) imaged additional structures on the Precambrian surface, in the southern portion of the province.

The crustal profile in figure 7.3 shows that P-wave velocities within the crust can vary from 6.05 to as high as 7.25 km/sec. The depth to the upper mantle ranges between 45 and 50 km. Several horizons show dips greater than 4 deg. The notations "Riel A" and Riel M" will be discussed later.

Although the structure in the crust is complex, a simple crustal model must be adopted. A two layer model (ie. crust and upper mantle) has been proposed by Kanasewich et al. (1987). Their model for southern Saskatchewan is based on the aforementioned refraction surveys. They suggest an average P-wave velocity of 6.48 km/sec for the crust and an upper mantle velocity of 8.20 km/sec at 45 km

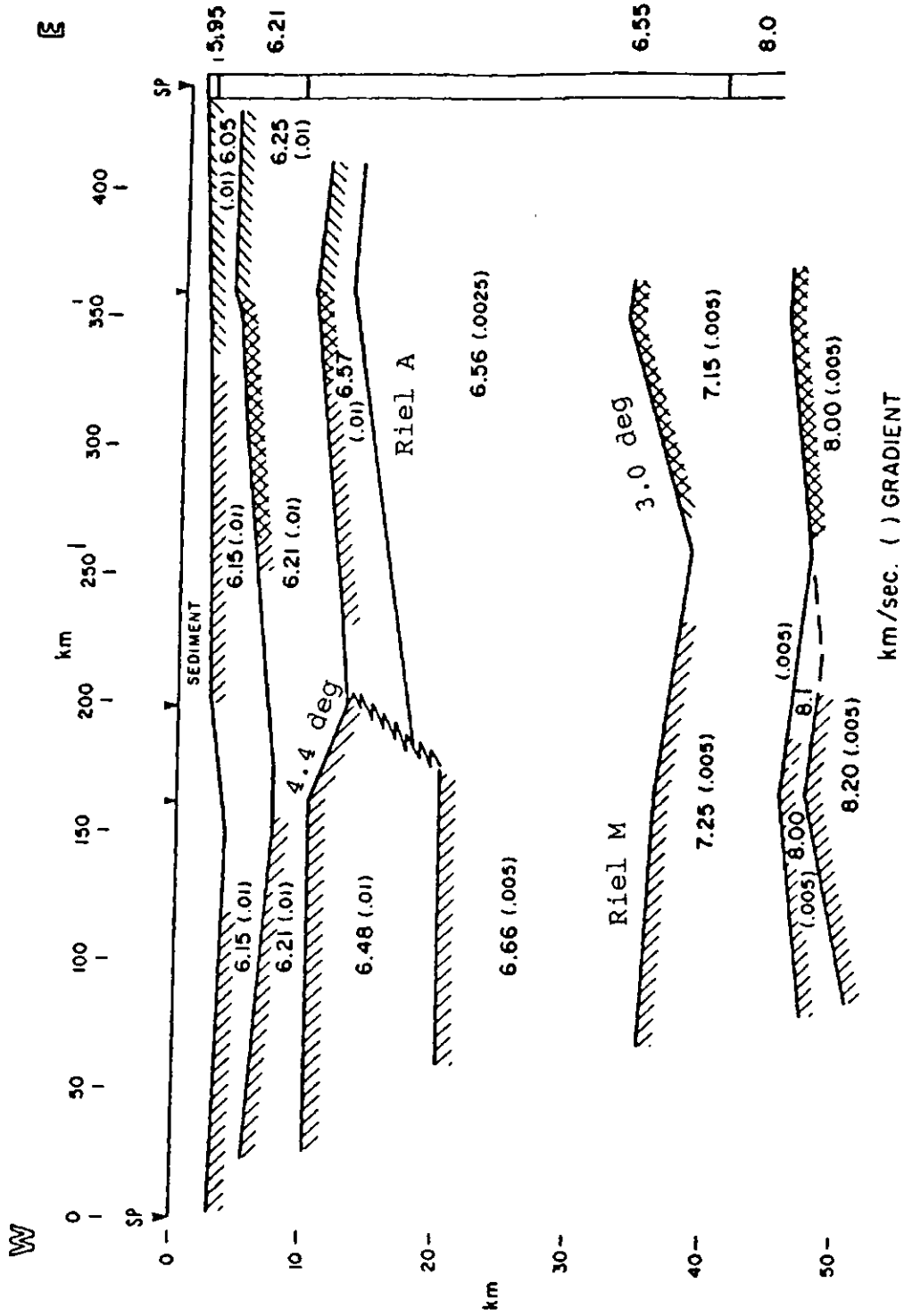


Figure 7.3. East to west crustal profile of southern Saskatchewan (from Hajnal et al., 1984).

depth. Horner et al. (1973) analysed phase velocities from seismograms of a southern Saskatchewan earthquake. Their work suggests P-wave velocities of 6.14 km/sec for the crust, and 8.40 km/sec for the upper mantle. The S-wave velocity for the latter was found to be 4.73 km/sec, and the  $L_0$  phase velocity was 3.56 km/sec. These results give different models for the crust. Horner et al.'s (1973) data were used for an initial model since their work is based on a Saskatchewan earthquake. The following sections use earthquake data to develop a new crustal model suitable for the Saskatoon area.

## 7.2 Regional Earthquake Travel Time Function

Fourteen regional earthquakes have been studied to devise a travel time function for the USSN. Only digitally recorded events with good S/N were used in the analysis. Figure 7.4 gives an example of BRG seismograms from an event used in the study. Descriptions of the earthquakes were obtained from the GSC and National Earthquake Information Centre. Figure 7.5a displays the locations and magnitudes of the events.

Processing of the data consisted of instrumental deconvolution and band-pass filtering. The filter pass-band had a low-cut of 0.5 Hz and high-cut of 3.5 Hz. The seismograms were plotted on paper, at 4 mm/sec, and the phase arrivals were picked by hand. The arrival phase times

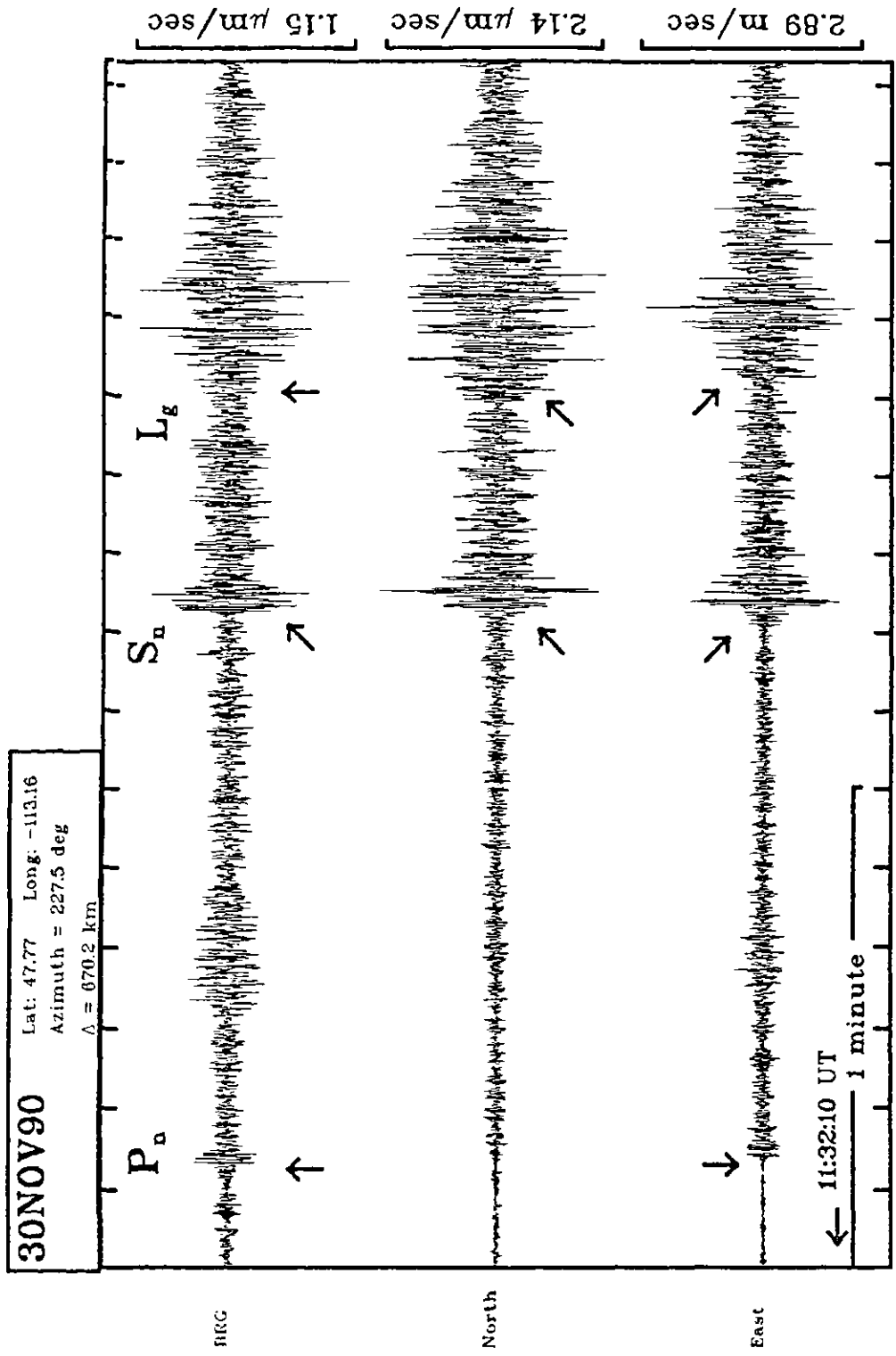


Figure 7.4. BRG seismograms from a regional earthquake.

## Regional Earthquake Phase Study

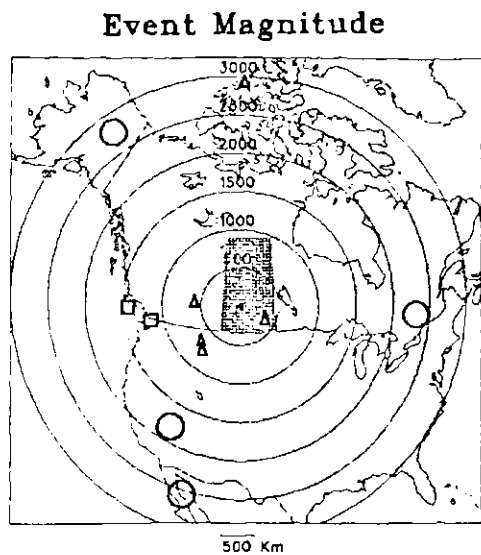


Figure 7.5a. Regional event magnitude  
**Mag. units ( $M_N$ )**

- $\Delta$  3.0 - 3.9
- $\square$  4.0 - 4.9
- $\bigcirc$  5.0 >

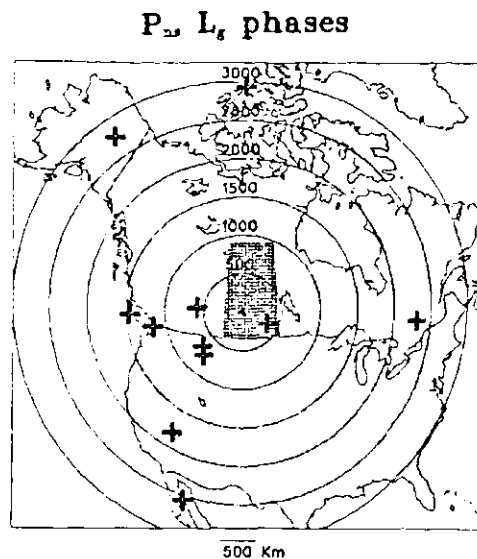


Figure 7.5b.  $P_n$  and  $L_g$  phase distribution.

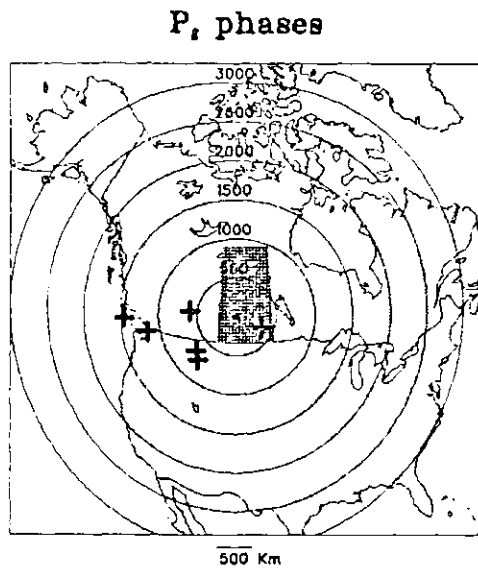


Figure 7.5c.  $P_s$  phase distribution.

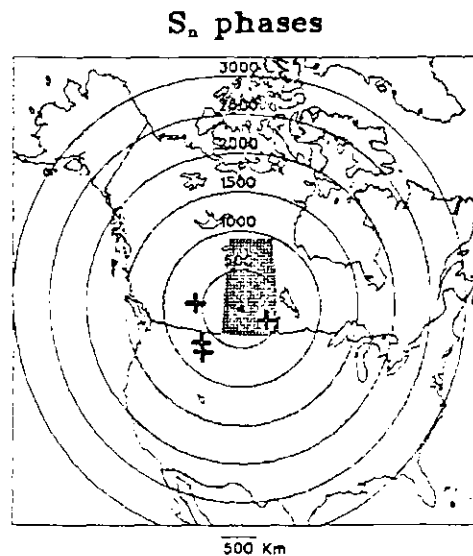


Figure 7.5d.  $S_n$  phase distribution.

**Contour Interval = 500 km**

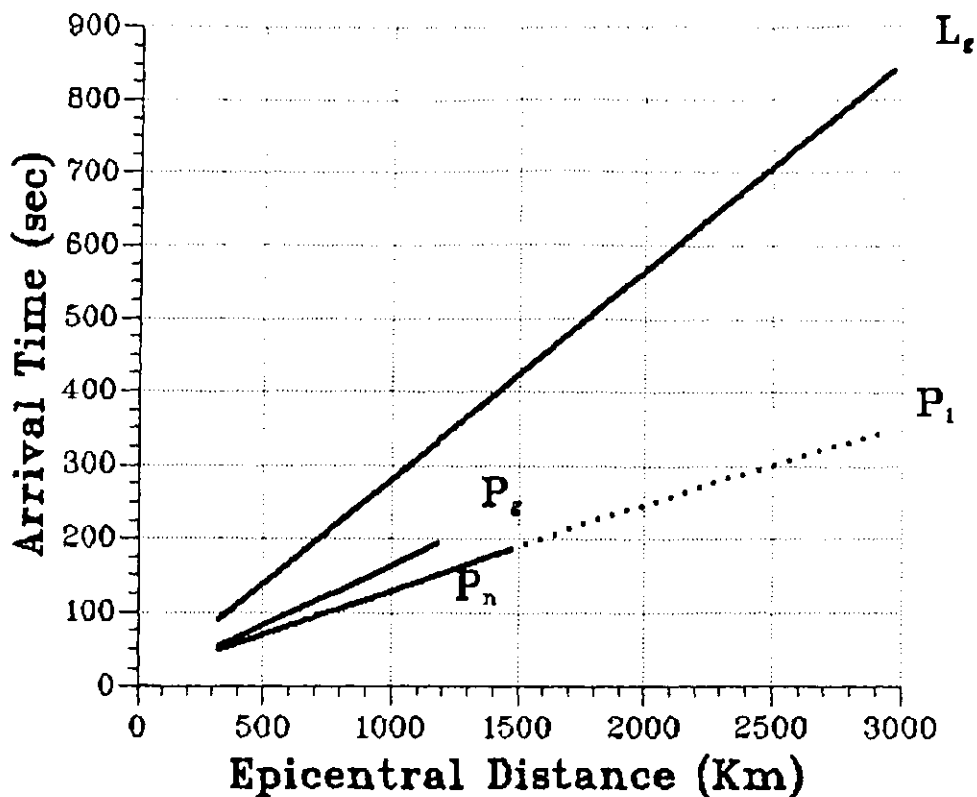
for the body-waves were time corrected to a source depth of 5 km. Also, the COM station phase arrivals were corrected for the depth of the station.

Phase arrivals on the seismograms were picked only if they were easily recognized. The most difficult phase to pick accurately was found to be  $S_n$ . Figure 7.5b shows the events used for  $P_n$  and  $L_g$  phase picks. Figure 7.5c shows the sources of the  $P_g$  phases used, and figure 7.5d shows  $S_n$  phase sources. Unfortunately, the  $S_n$  phase sources were all concentrated at similar epicentral distances so a reliable velocity could not be obtained from these data.

A summary of the regional phase study is given on figure 7.6. The  $P_n$  arrivals were found to have a velocity of 8.30 km/sec to an epicentral distance of about 1500 km. Past this point, the first P-wave arrivals seemed to have penetrated significantly into the mantle. These arrivals are indicated by a dashed line. The  $P_1$  designation implies that the arrivals were no longer refractions along the base of the crust. The  $P_g$  and  $L_g$  phases were found to travel at velocities of 6.16 km/sec and 3.51 km/sec respectively.

The phase velocities measured in this study are compared in Table 7.1 to results from other studies and the GSC crustal model. The  $P_n$  velocity from Kanasevich et al. (1987) may be lower because of a velocity gradient in the upper mantle. The offsets they used in the refraction experiments are much less than epicentral distances from regional earthquakes. Since  $S_n$  was not well observed, the

## Regional Phase Arrival Times



$P_n$   $8.30 \pm 0.06$  km/sec  $T_i = 9.5 \pm 0.8$  sec

$P_e$   $6.16 \pm 0.05$  km/sec  $T_i = 1.8 \pm 1.3$  sec

$L_e$   $3.51 \pm 0.02$  km/sec  $T_i = -1.2 \pm 3.1$  sec

Figure 7.6. Travel time table for regional earthquakes.

Phase	Velocity (km/sec)			
	This Study	Horner et al. (1973)	Kanasewich et al. (1987)	GSC
$P_n$	8.30/46	8.40/45	8.2/45	8.2/36
$P_g$	6.16	6.14	6.1	6.2
$L_g$	3.51	3.56	-	3.57
$S_n$	-	4.73	-	4.7

Table 7.1. Comparison of crustal phase velocities.  $P_n$  estimates have the depth to the Moho included after the slash.

value from Horner et al. will be used in the travel time table for the USSN.

The intercept time for  $P_n$  can be used to derive an average depth to the Mohorovicic discontinuity (Moho) from the following equation:

$$2h - f = T_1 V_2 V_1 / (V_2^2 - V_1^2)^{1/2}, \quad 7.1$$

where: h is depth to the Moho,

f is focal depth,

$T_1$  is the intercept time,

$V_1$  is the average crustal velocity,

$V_2$  is upper mantle velocity.

A depth of  $46 \pm 4$  km was derived, using the intercept time of figure 7.6, the  $P_0$  velocity for  $V_1$ , the  $P_n$  velocity for  $V_2$ , and a focal depth of 5 km. This value agrees with the average depth of 45 km suggested by Kanasewich et al. (1987) for southern Saskatchewan.

The travel time table presented here is meant to be a preliminary function for the USSN. The table has been entered into US\_ANALYSE and is used for regional epicenter location. Presently, the array event detector is saving most regional events that are being recorded by the system. With the increased volume of regional data, a more detailed travel time function can be derived in the future. A particularly interesting study would be an investigation

into azimuth variable body-wave phase travel times. If a pattern emerges, the derived azimuth variable velocities may be related to lineaments within the basement (discussed by Kent, 1973; Thomas, 1974).

### 7.3 Relative Travel Time Anomalies of Teleseismic Earthquakes

Seismochronography has revealed that many regions of the world exhibit deviations from standard travel times for earthquakes (Richter, 1958). These deviations are thought to result from lateral velocity inhomogeneities at three different locations along the ray path: the source region, at the deepest point of ray penetration, and at the receiver side of the ray path (Berteussen, 1975). The latter results from structure on the Moho, or some combination of structure and velocity inhomogeneities in the crust. Travel time disturbances near the stations affect incoming rays from many different directions and distances. Epicenter location methods which use seismic array data are based on travel time measurements. Clearly, such travel time disturbances would produce patterns of mis-located earthquakes. Such a phenomenon has been observed by researchers such as Engdahl and Felix, 1971; Mok et al., 1982; and VanDecar and Crosson, 1990.

This section investigates teleseismic earthquake mis-location anomalies at Saskatoon. Eighty well recorded

earthquakes, at distances between about 18 deg and 100 deg are used for the analysis. The mis-locations here fall into gross patterns which suggest that anomalous velocity changes within the crust are present under the USSN stations.

### 7.3.1 The Teleseismic Data

A map showing the locations of the earthquakes used in the study is given on figure 7.7. The earthquakes from the various areas can be divided into azimuthal sample ranges of the crust under the USSN. These ranges are grouped as follows:

- 1 0 - 60 deg, Europe, the Middle East and Pakistan;
- 2 130-174 deg, Central and South America;
- 3 175-219 deg, Nevada nuclear test site, southern California, Tuamotu Arch (Tuamotu Archipelago atoll nuclear tests);
- 4 220-279 deg, Pacific rim;
- 5 280-330 deg, Aleutian island arc, Kuril island arc, and Siberia.

There are some gaps in the azimuthal ranges between 60 deg to 130 deg and 330 deg to 360 deg. Earthquakes from India fall into the latter range. The distances are greater than 100 deg, so the events are of no use to this study. Earthquakes from the Mid- and Central Atlantic Ridges are located between 060 and 130 deg. Unfortunately, no events with adequate S/N were recorded from this region during the

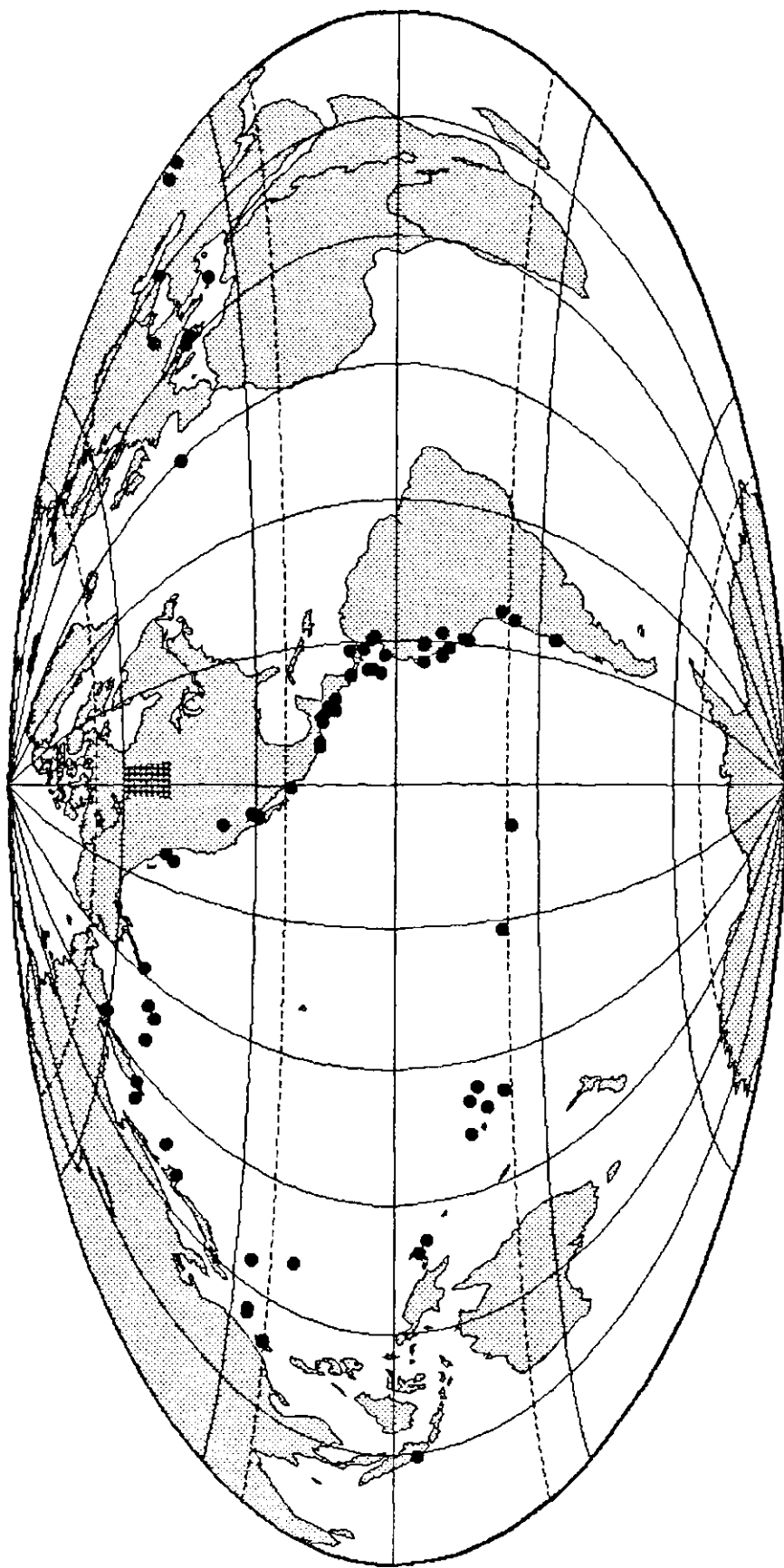


Figure 7.7. Location map of teleseismic earthquakes used in study.

study.

### 7.3.2 Method of Analysis

The slowness and azimuth of the first P phases from an earthquake are the only parameters required to locate the epicenter. These two parameters were acquired from the data using the cross-correlation and location procedures discussed in sections 5.3.1 and 5.3.2 respectively. Only strong peaks or troughs, which could be correlated between the station P phase arrivals, were utilised to obtain the relative arrival times. The procedures can measure relative arrival times between the stations to about 0.1 sec accuracy. This results in uncertainties of about 0.4 sec/deg and 3 deg for the apparent slowness and azimuth, respectively.

Mis-location patterns are investigated by comparing measured slowness and azimuth parameters to theoretical parameters that should be observed on a perfect earth. The theoretical slowness as a function of epicentral distance has been tabulated by Herrin et al. (1968a). Their results are based on a preliminary reference earth model (PREM) described by Herrin et al. (1968b). The other theoretical parameter, azimuth, is readily obtained from spherical trigonometric functions.

The derived epicenter locations from the USSN must be corrected for the depth of the COM mine site. If the

correction is neglected, gross location errors are introduced. The time correction varies as a function of distance, since the emergent angle of the P phase changes with epicentral distance. P phase emergent angles for a PREM have been tabulated as a function of distance by Pho and Behe (1972). The PREM was substituted with the preliminary earth model for the Saskatoon area (section 7.1) and new P phase emergent angles were calculated. A COM time correction function for P phases could then be devised using the emergent angles and the local earth model. The appropriate COM time adjustments have been applied to the teleseismic P phase arrivals used in this study.

### 7.3.3 Teleseismic Azimuthal and Slowness Anomalies

The mis-locations from each group are summarized by an array diagram which is presented in figure 7.8. An array diagram transposes an epicenter into a slowness and azimuth with respect to a seismic array. Large epicentral distances map close to the center of an array diagram while close events fall near the perimeter of the plot. For example, the 6 sec/deg circle on the diagram in figure 7.8 represents a distance of about 72 deg, while the 12 sec/deg circle represents a distance of about 18 deg.

The heads of the arrows on the diagram mark the positions of the location parameters that would be measured on a PREM. The geographical locations for the earthquakes

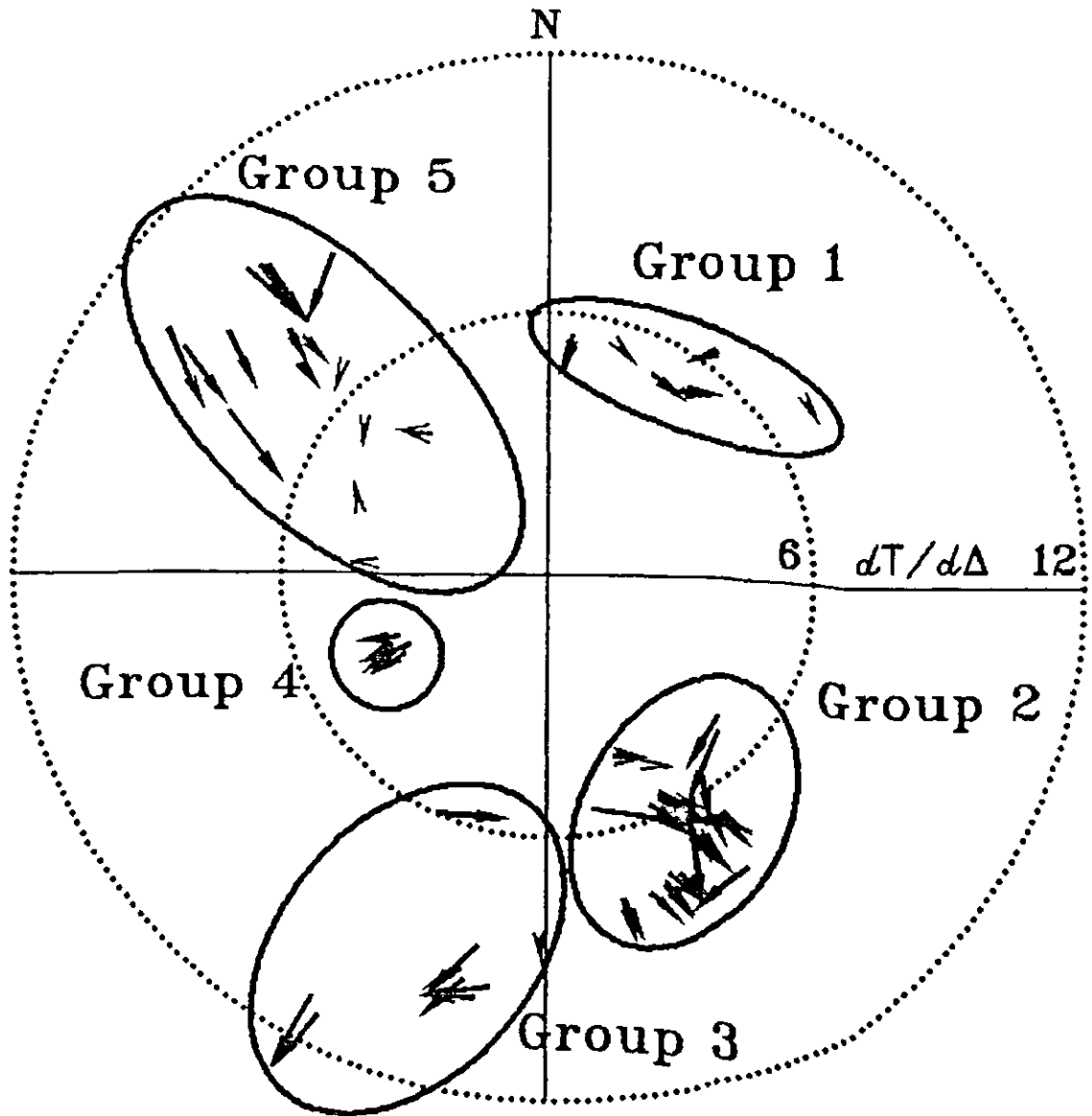


Figure 7.8. Array diagram showing mis-located earthquakes.

were obtained from the National Earthquake Information Centre. The slowness parameters for the locations have been corrected for the variations in hypocentral depth. The tails of the arrows are the parameters that were measured from the USSN data.

There are two basic trends in mis-locations on the array diagram. The most prevalent pattern is a strong mis-location trend in a north westerly direction which affect groups 1, 2 and 5. Another pattern suggested is in groups 3 and 4 where the mis-locations fall more into a north easterly trending direction.

The mis-location errors for group 5 are significant as they represent average errors in distance of about 7 deg. An example showing a mis-located earthquake is given on figure 7.9. The square box around the USSN location highlights the region of inherent error. The inherent error is a result of the limitations imposed by the timing accuracy. The actual location falls outside this region of error.

#### 7.3.4 Teleseismic Relative Travel Time Residual Patterns

To give actual time delay values to the array diagram of figure 7.8, relative travel time residuals (RTTRs) are plotted for the possible USSN station combinations on figure 7.10 as a function of azimuth. A relative travel time is

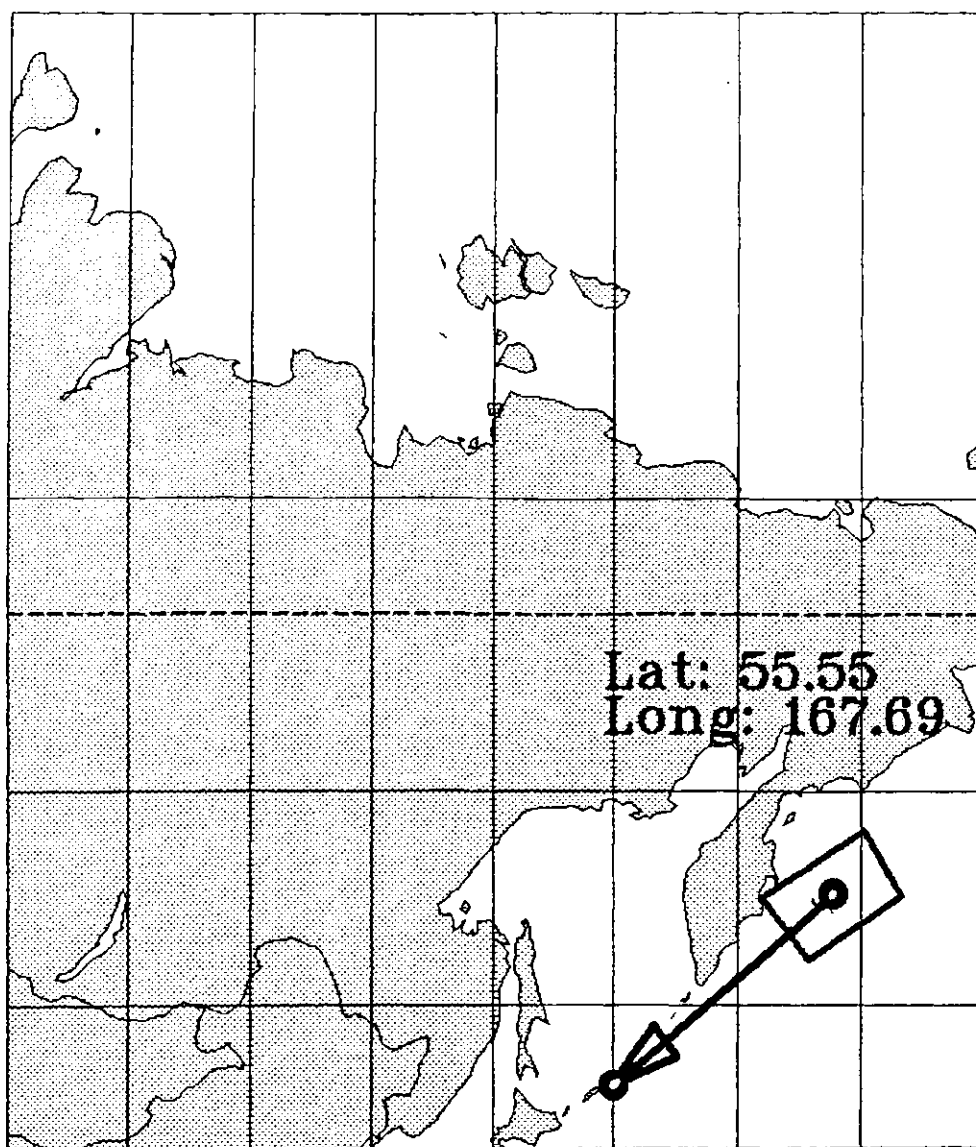


Figure 7.9. Map showing an example of the mis-location of an earthquake from the Kuril islands. The arrow points to the dot that marks the true location. The mis-location is significant.

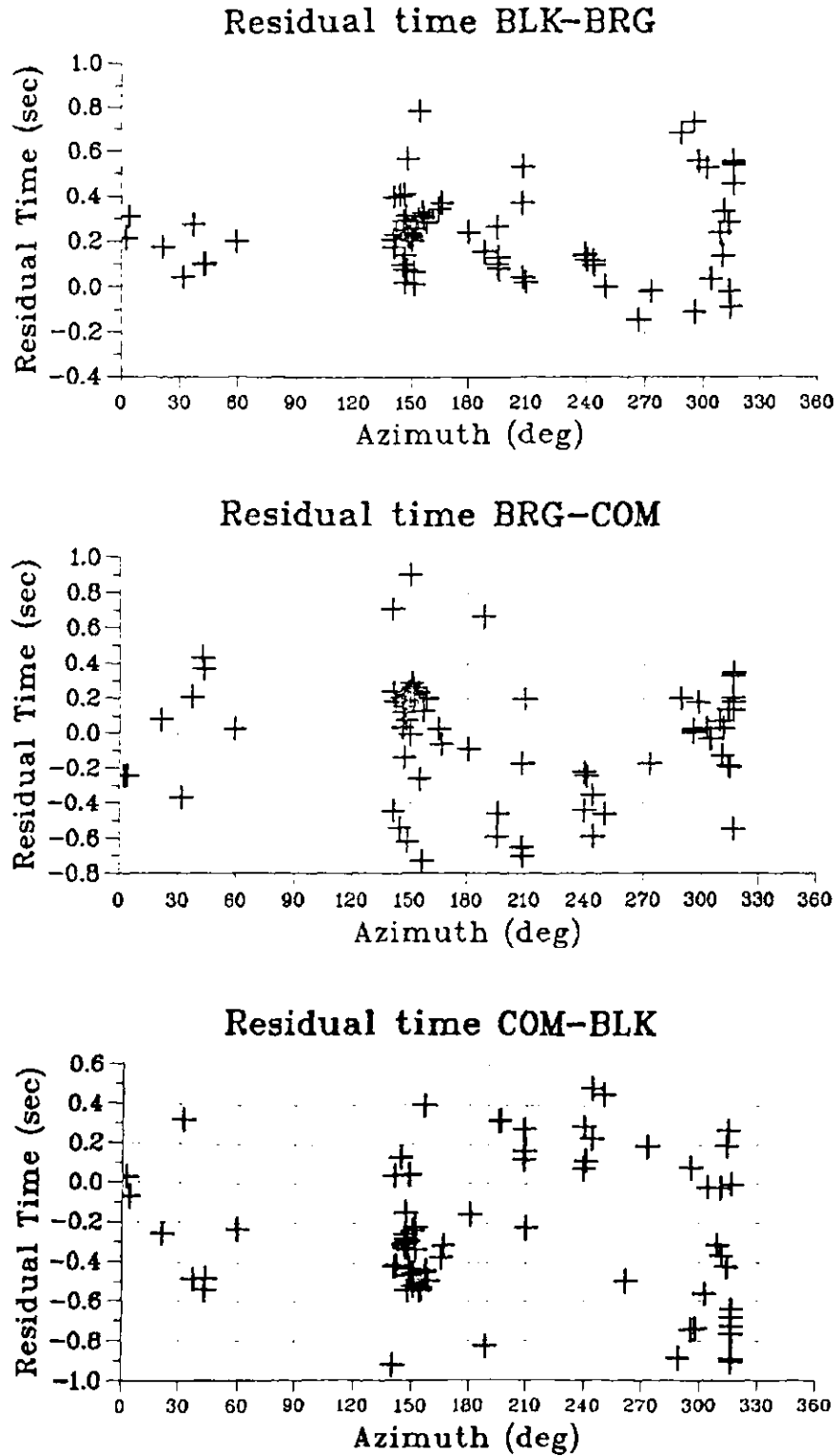


Figure 7.10. Relative travel time residuals for the teleseismic data.

defined as the difference in P phase arrival time between two stations separated by some distance. A RTTR is defined as follows:

$$\text{RTTR} = \text{TS} - \text{TP}, \quad 7.2$$

where: TS is the observed relative travel time between two stations,

TP is the theoretical relative travel time that would be observed on a PREM.

The RTTRs show a somewhat sinusoidal pattern with azimuth. Such patterns would be expected from moderate spatial changes in seismic velocity in the crust, under the array. The average RTTRs for each azimuthal zone (discussed in section 7.2.1) are found in table 7.2a.

In most of the azimuth groups, the station combinations that show the largest RTTRs are BLK-BRG and COM-BLK. Time delays as large as 0.43 sec are found for earthquakes between 280 and 330 deg. The common station is BLK. It appears that the site is usually experiencing late P phase arrivals.

The station combinations of COM-BLK and BRG-COM show a different pattern between azimuths of 175 and 280 deg. The COM station has the late P phase arrivals from this azimuthal group.

Clearly, the patterns of RTTRs cannot occur at the

Group	Number	Azimuthal Range (deg)	Average RTTRs (sec)		
			BLK-BRG	COM-BLK	BRG-COM
1-	9	0- 60	0.16±0.02	-0.19±0.01	0.03±0.01
2-	33	060-175	0.26±0.02	-0.34±0.01	0.09±0.03
3-	9	175-220	0.17±0.04	0.14±0.10	-0.31±0.15
4-	8	220-280	0.20±0.07	-0.10±0.09	-0.10±0.02
5-	21	280-330	0.36±0.04	-0.43±0.10	0.07±0.06

Table 7.2a. Average relative travel time residuals for the azimuthal groups.

Slowness (sec/deg)	Number	Average RTTRs (sec) Group 5. 280 deg - 330 deg		
		BLK-BRG	COM-BLK	BRG-COM
<6	4	-0.04±0.02	0.11±0.07	-0.07±0.05
>6	17	0.46±0.02	0.56±0.08	0.11±0.06

Table 7.2b. Average relative travel time residuals for Group 5.

source regions or deep in the mantle. It is unlikely that such effects would cause a pattern of RTTRs to develop. The patterns must be a result of local velocity heterogeneities within the crust.

#### 7.3.5 Station Time Corrections

The average RTTRs for the azimuthal groups have been used to develop a relative station time correction function. BLK was chosen as the reference station. Then, the BRG time corrections as a function of azimuth is the RTTRs for BLK-BRG. Similarly, the time corrections for COM are the negative of the RTTRs for COM-BLK.

The station correction function has been applied to the data, and the corrected array diagram is presented on figure 7.11. The orientations of the mis-location vectors have become more random than the array diagram of figure 7.8. An obscure pattern is still apparent for the group 5 earthquakes. Events with a slowness greater than 6 sec/deg appear to be under-corrected, while the other events are over-corrected.

A slowness variable time correction was adopted for the group 5 earthquakes to compensate for the residual mis-locations. The correction is listed in table 7.2b. The array diagram with the new correction function is given in figure 7.12. The orientations of the mis-location vectors are mostly random on the entire plot.

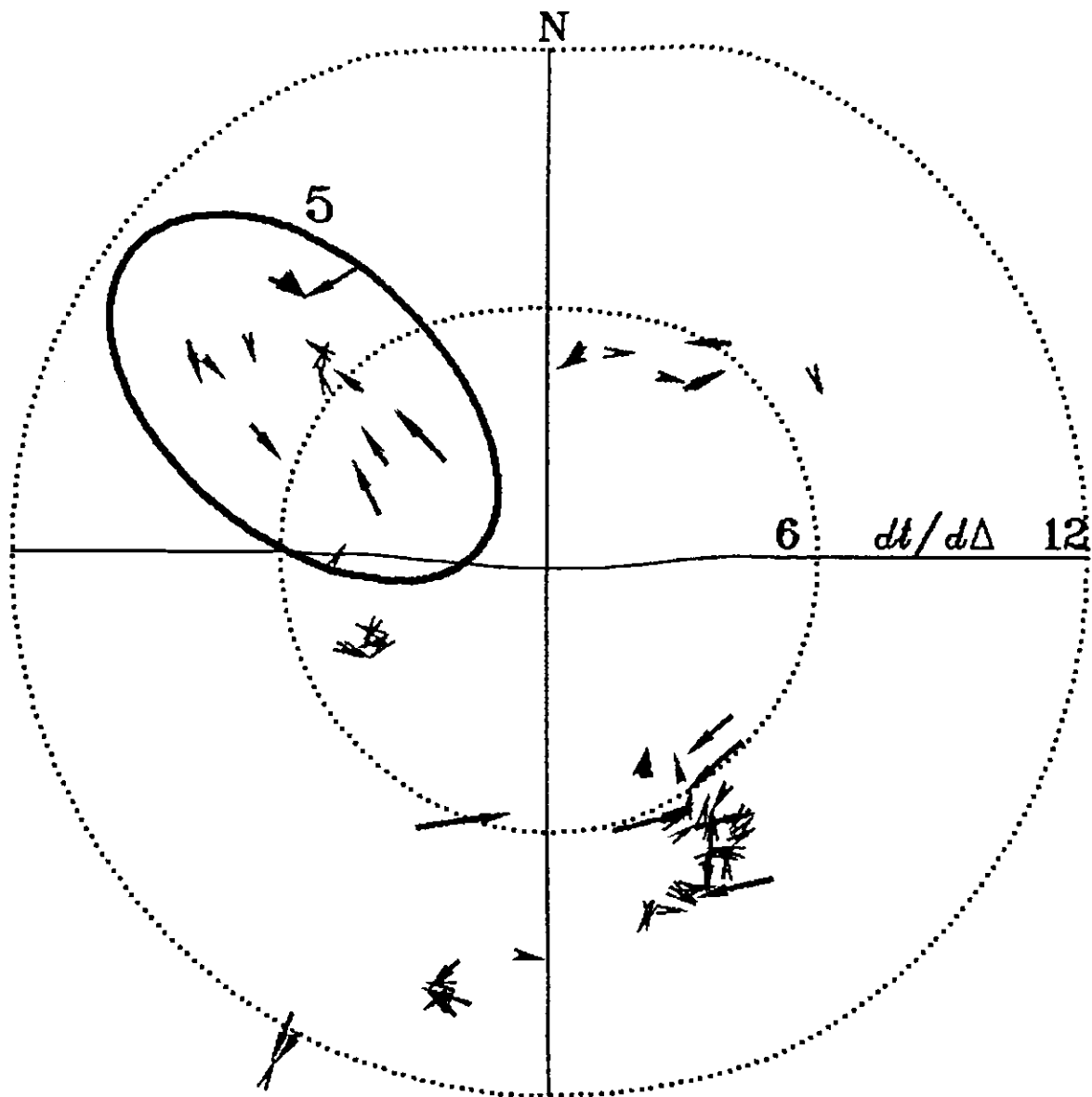


Figure 7.11. Array diagram after application of azimuth variable travel time corrections. The group 5 events still show a residual pattern.

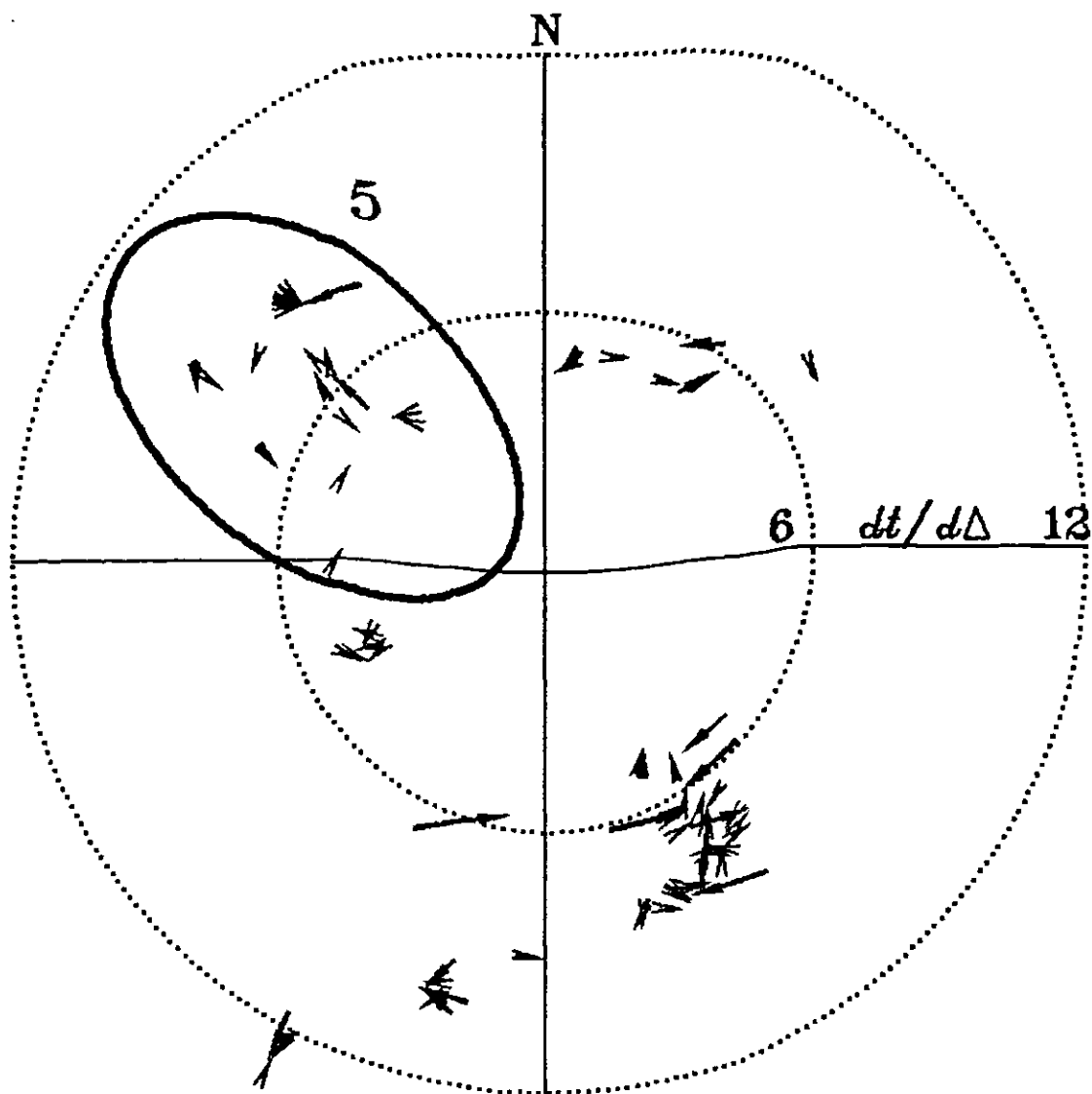


Figure 7.12. Array diagram after application of azimuth and slowness variable time corrections. Now the group 5 events are random in their orientations.

The earthquake which was located in figure 7.9 is re-located in figure 7.13, using the new station corrections. The actual location is within the inherent error of the location method. The scattered pattern on figure 7.12 results from the random inherent error in the method. Most of the non-random error, resulting from velocity variations in the crust, has been removed via the station corrections.

#### 7.3.6 Discussion

A distinct interpretation of the sub-surface under the USSN cannot be obtained from these data because of sparse spatial sampling. However, the structure must be complex in order to produce anomalous relative travel times as high as 0.4 sec over distances of 50 km. If these times are the result of structures in the crust, than the Bouguer gravity maps of the area should show rather large anomalies. For example, a time anomaly of 0.4 sec resulting from structure at the base of the Cretaceous, would require changes in depth below two stations of almost 1.5 km; for structure on the Precambrian, the depth difference would have to be greater than 11 km; on the Moho, depth differences of 40 km are needed. Undoubtedly, such structures would be obvious on the gravity maps.

The Bouguer gravity maps in the area do not seem to reflect the anomalous travel time. The BLK station was found to have late arrival times, but there is no

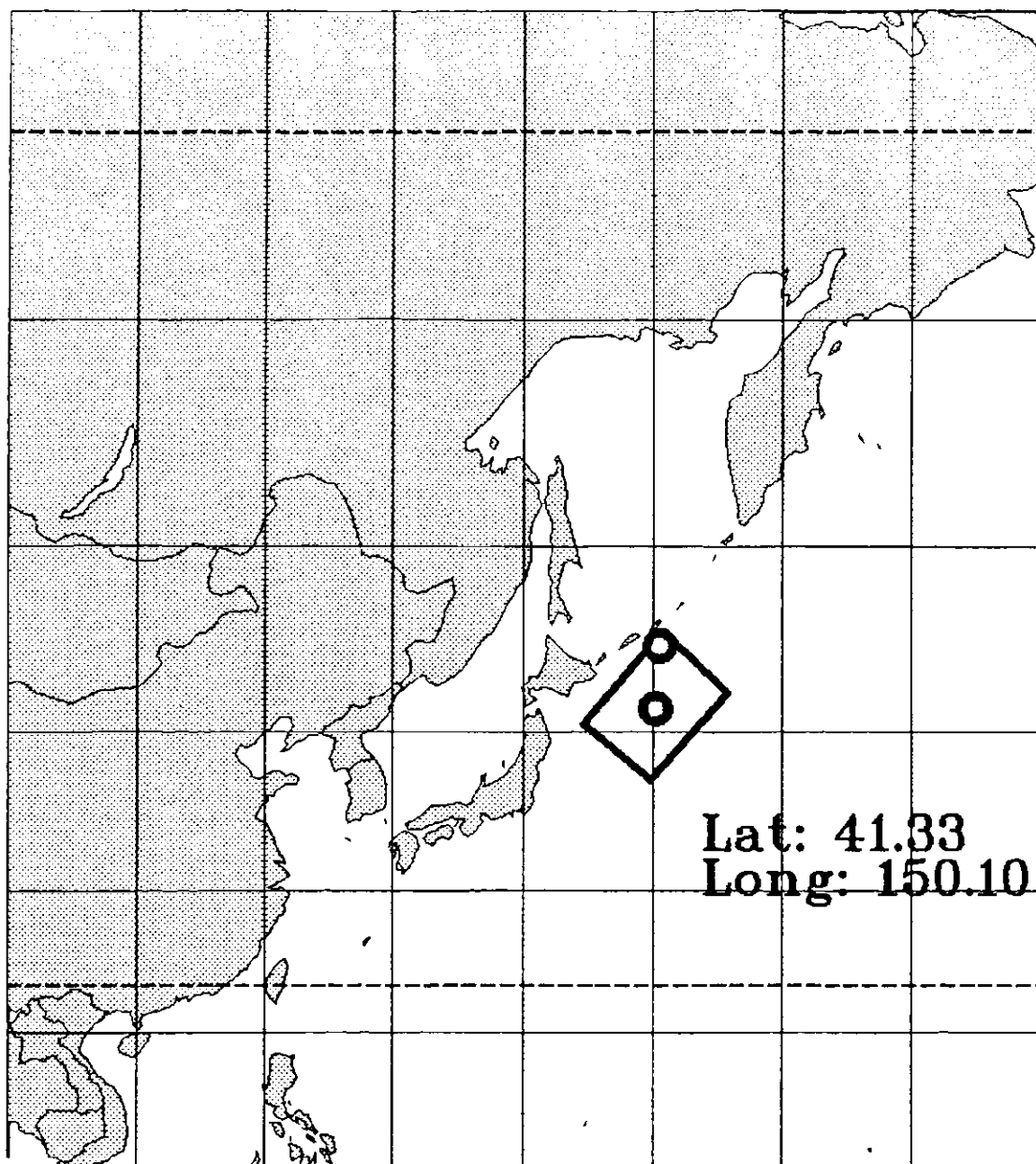


Figure 7.13. Map showing the mis-location of the earthquake in figure 7.9 after the station corrections. The error in location, after the station corrections, is random. The box marks the inherent error region of the location.

exceptional anomaly under the station. However, it is puzzling that there is a slightly positive anomaly under BRG which is not apparent under COM. Positive gravity anomalies imply that denser rocks are present, and denser rocks usually have higher seismic velocities. Both stations have similar travel times, for most azimuths, so the observation is very curious.

Mok et al. (1982) have noticed similar magnitudes of travel time anomalies for a tripartite array in London, Ontario. They, also, could not attribute the observations to the Bouguer gravity and structure within the crust. For their data, it was suggested that the anomalous times were caused by velocity heterogeneities within the crust. That implies that the velocity fluctuates both laterally and vertically. The fluctuations cause seismic rays from earthquakes to follow convolved paths through the crust, rather than straight lines for a homogeneous case. They suggested that velocity variations as small as 0.14 km/sec over a ray path distance of 15 km could produce travel time delays as large as 0.3 sec.

Mok et al.'s (1982) work may be a plausible explanation for the anomalous times observed here. Whatever the cause, the residual times change with azimuth. Time delays for groups 3 and 4 increase in a south-westerly direction (figure 7.8), while for the other groups, the direction trends strongly towards the south-east. It is interesting to note that the patterns follow the attitudes of the known

lineaments within the basement (Kent, 1973; and Thomas, 1974). Whether the observations are related cannot be discerned now.

A more conclusive picture should emerge in the future, from local and regional earthquake data which are being collected at present. The results should give insights about heterogeneous rock property variations within the crust.

#### 7.4 The Kuroki Earthquake: A Opportunity to Study

##### Refractions From a Discontinuity Within the Crust

The Kuroki earthquake of 25 April, 1991, produced exceptional seismograms at the USSN (figure 7.14). The magnitude of the event was  $M_N = 3.2$  (from the GSC) and location was confined by an isoseismal survey. The apparent velocity of 6.82 km/sec for the first P arrivals (denoted  $P_1$  in figure 7.14) were curious because the value is intermediate to  $P_g$  and  $P_n$  velocities. This suggests that a strong refractor exists within the crust in central Saskatchewan. An interesting coincidence with this earthquake is the cross-over distance for  $P_n$ , which occurs between BRG and COM. The  $P_n$  phase can be identified on the COM seismogram as a small first arrival (figure 7.14). The next arrival on COM was the large  $P_1$  arrival. The following discussion relates the  $P_1$  arrivals to the Riel discontinuity (known as the Conrad discontinuity in Europe). In order to

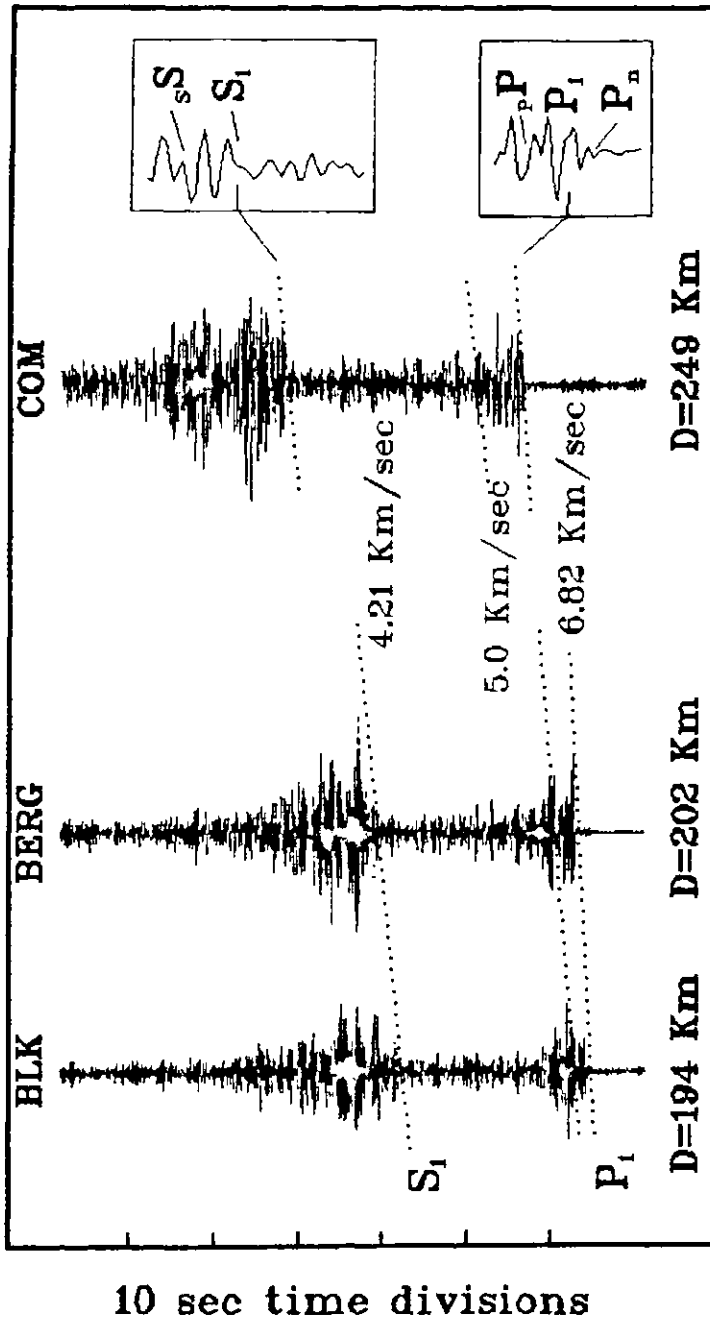


Figure 7.14. The vertical USNN seismograms from the 1991 Kuroki earthquake.

estimate the depth with some accuracy, a location, focal depth and origin time are required. The section begins with an estimation of these parameters.

#### 7.4.1 Epicenter Location

The location of this earthquake was well confined by an isoseismal survey (figure 7.15) to an accuracy of about 1 km. The derived location is considerably more accurate than one derived from a regional network. Typically, using seismic stations in western Canada, the location accuracy is about 20 km.

The survey was conducted on a door to door basis, and all the residents within about a 10 km radius of the epicenter were questioned. The intensities were assigned according to the Modified Mercalli intensity scale. The epicenter was directly east, 215 km from the center of the USSN array.

#### 7.4.2 Focal Depth

Accurate instrumental focal depth determinations require direct P and S arrival times from several stations at distances less than about 100 km (Horner et al., 1973). For the Kuroki event, such data are not available. However, a number of factors suggest that the depth is less than 2 km. The evidence is listed as follows.



#### 7.4.2.1 Isoseismal Survey

The large area of perceptibility suggests that the event is quite shallow. This survey is similar to the nature of isoseismal maps from other Saskatchewan earthquakes of similar magnitudes (see Horner and Hasegawa, 1978; Horner et al., 1980; Gendzwill et al., 1982; Gendzwill, 1984; Gendzwill and Prugger, 1980). All Saskatchewan earthquakes that have occurred in the past are believed to be shallow. The depth for the Kuroki event can be estimated using empirical formulas of Shebalin (1959) and Karnik (1969). The analysis suggests a depth less than 1.5 km.

#### 7.4.2.2 Surface Waves

A train of low frequency, low velocity surface waves were very pronounced on all the USSN seismograms. The BRG vertical and horizontal seismograms are shown in figure 7.16. The seismograms are filtered with a low-cut of 0.3 Hz and a high cut of 1.5 Hz. The azimuth of the event was directly east of the array, so the east and north seismometers were orientated radial and transverse, respectively, to the rays. Note that the transverse component seismogram was clipped, thus the apparent low frequencies are artifacts of the filtering.

The slow waves apparent on the seismograms were

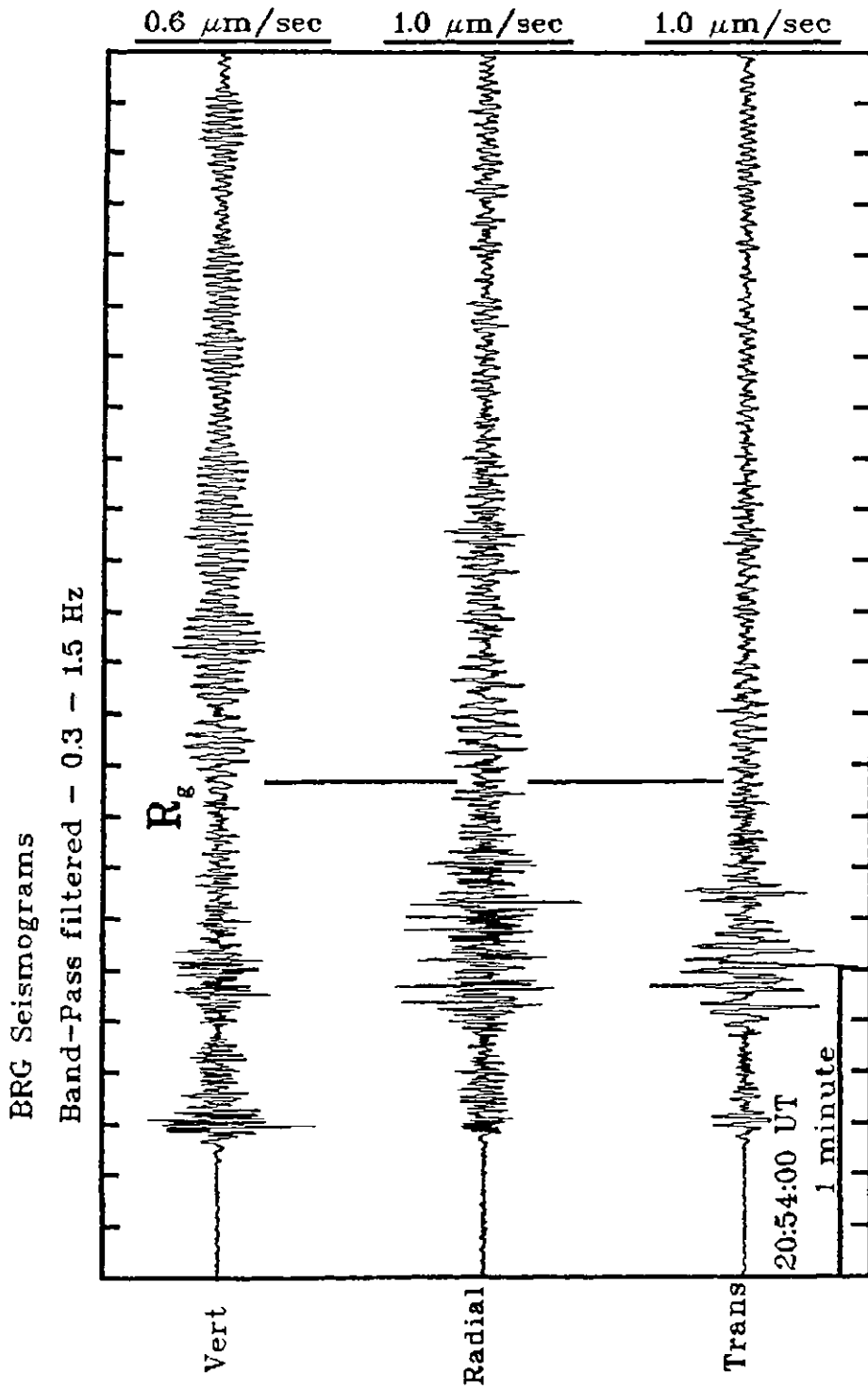


Figure 7.16. Low velocity  $R_g$  from the Kuroki earthquake.

traveling with a group velocity of 1.5 km/sec. Most of the trace motion for these waves are evident on the vertical and radial seismometers, implying that they are Rayleigh waves ( $R_g$ ). Such waves are often observed from shallow, Saskatchewan earthquakes (for an example, see Gendzwill et al., 1982). According to Kulhánek (1990), the presence of  $R_g$  on short-period seismograms "is a reliable indicator of a very shallow event with a focal depth of one or a few kilometers." The extremely low group velocity of  $R_g$  on the Kuroki seismograms suggests that the focal depth must have been very shallow since typical  $R_g$  crustal group velocities are around 3 km/sec.

#### 7.4.2.3 Seismogram Modeling

The seismograms are very complex (figures 7.14 and 7.17) and this alone suggests a shallow focal depth (Kulhánek, 1990). Seismogram modeling was used to investigate the effect of focal depth on the seismogram complexity. The method of modeling was the reflectivity method, which is limited to earth models with flat layers that have constant velocities. A point source, and the geological model of section 7.1, were used for the analysis. Figure 7.17 compares the BRG vertical seismogram to seismogram models for a 1 km and 10 km source depth. The 10 km focal depth model shows less complexity than the shallower model; suggesting that much of the complexity in

# Seismogram Modeling

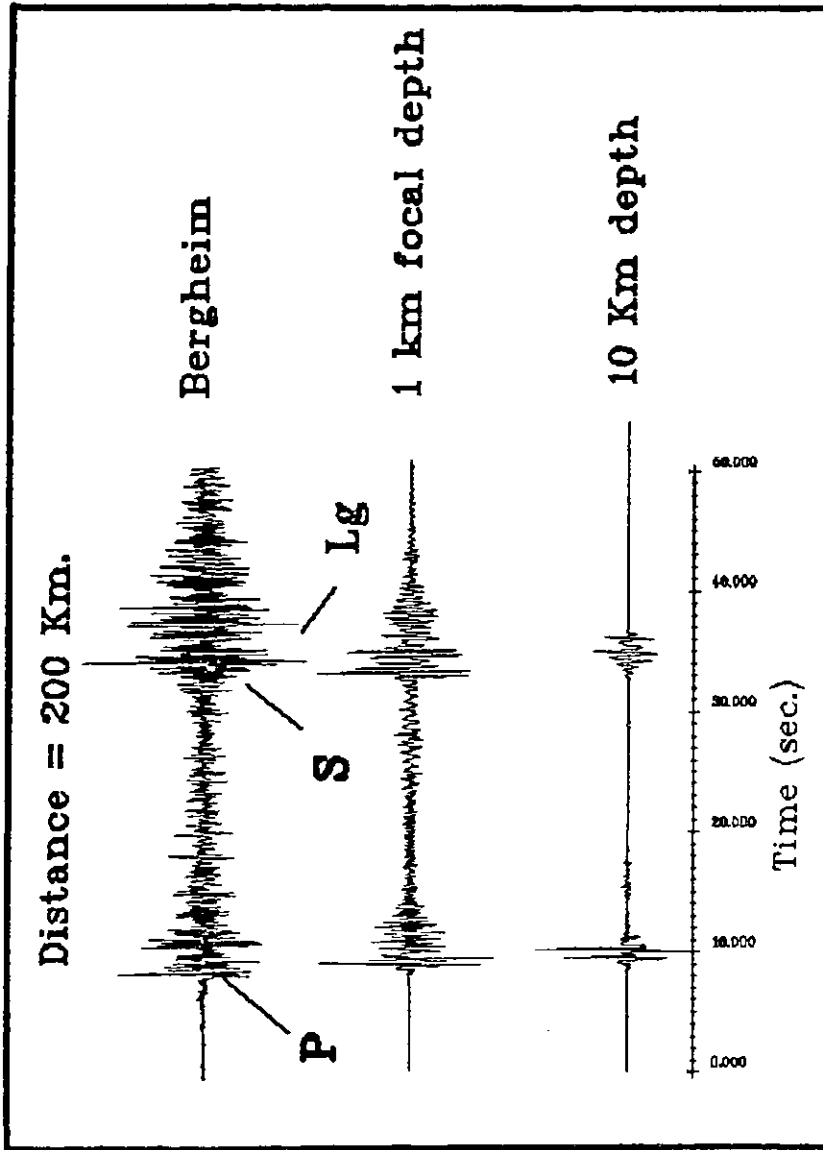


Figure 7.17. Seismogram modeling. The models show a reduction in seismogram complexity with focal depth.

the actual seismograms are the result of a shallow source.

An interesting peripheral observation, related to seismogram complexity, are the so called "depth phases" on the enlarged portions of the COM seismogram in figure 7.14. These phases, denoted  ${}_pP$  and  ${}_sS$ , are reflections from the surface above the COM station. Such phases appear often on COM seismograms.

#### 7.4.2.4 Geology

The north eastern edge of the Prairie Evaporite salt underlies the Kuroki area (Christopher et al., 1971; and Simpson and Dennison, 1975). It is speculated that removal of salt by dissolution causes subsidence of the overlying layers, which may lead to violent failures within the relatively competent carbonate rocks above the salt. There have been two other felt events from this area in the past ten years, suggesting that a continuing process is causing the events.

#### 7.4.2.5 Focal Depth Conclusion

With the four independent sources of evidence, the focal depth can be constrained with some confidence, to less than 1 km depth.

### 7.4.3 Phase Velocities Comparison

The origin time suggested by the GSC was 20:53:53.9 UT using their crustal model (listed in table 7.1). Seven stations in the Canadian Seismograph Network (excluding the USSN stations) recorded the Kuroki earthquake. The GSC estimate of the origin time can be used to compare travel times of crustal phases derived from a standard GSC model (table 7.1) to the phase arrival times observed on the USSN seismograms. The accuracy of the origin time estimate can be evaluated from the comparison. The study is given in figure 7.18, where 0.0 sec on the travel time axis corresponds to the GSC origin time estimate. The GSC crustal phases' arrival times are plotted as functions of epicentral distance. Two  $P_n$  phase arrival functions are plotted for Moho depths of 36 and 45 km. The standard depth to the Moho, used by the GSC, is 36 km. The  $P_1$  and  $S_1$  arrivals measured on the USSN seismograms, are plotted on the graphs as crosses, and the  $P_n$  arrival at COM is plotted as an asterisk. The phase arrival times measured on the COM seismogram have been time corrected for the 1 km depth of the station.

The enlarged portion of the graph on the top of figure 7.18 suggests that the GSC origin time is too early. The  $P_1$  arrivals, and the  $P_n$  arrival at COM, are later than the  $P$  phase arrivals suggested by the GSC model. Additionally, the trend of the  $P_1$  arrivals show that their apparent

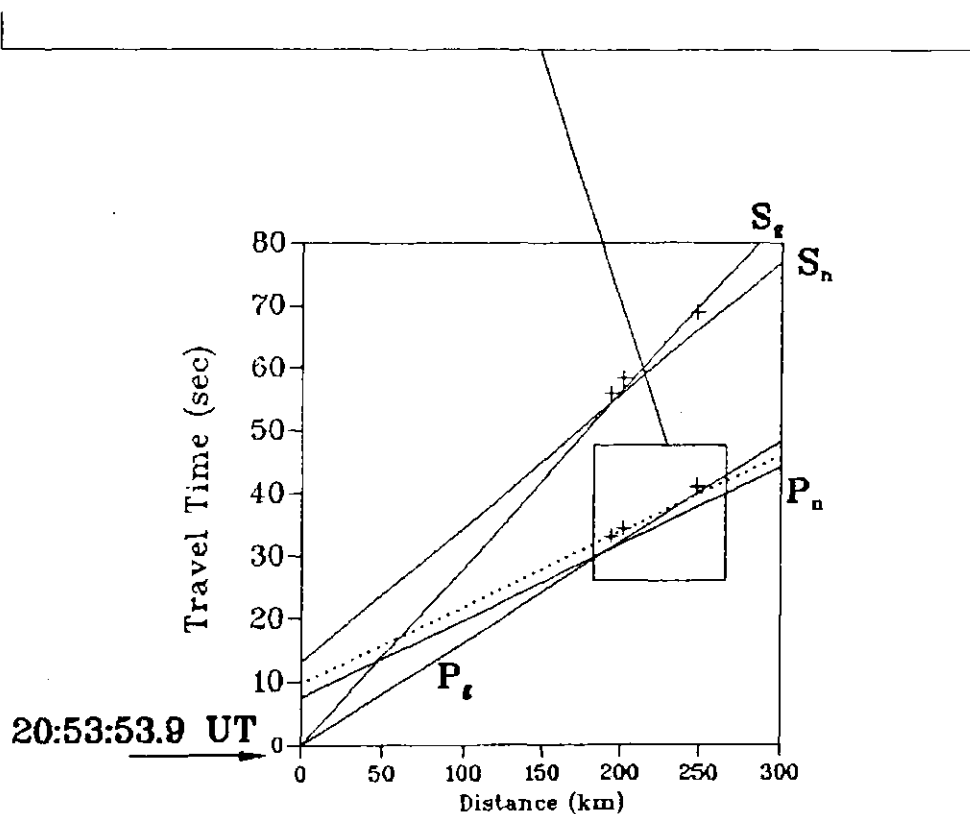
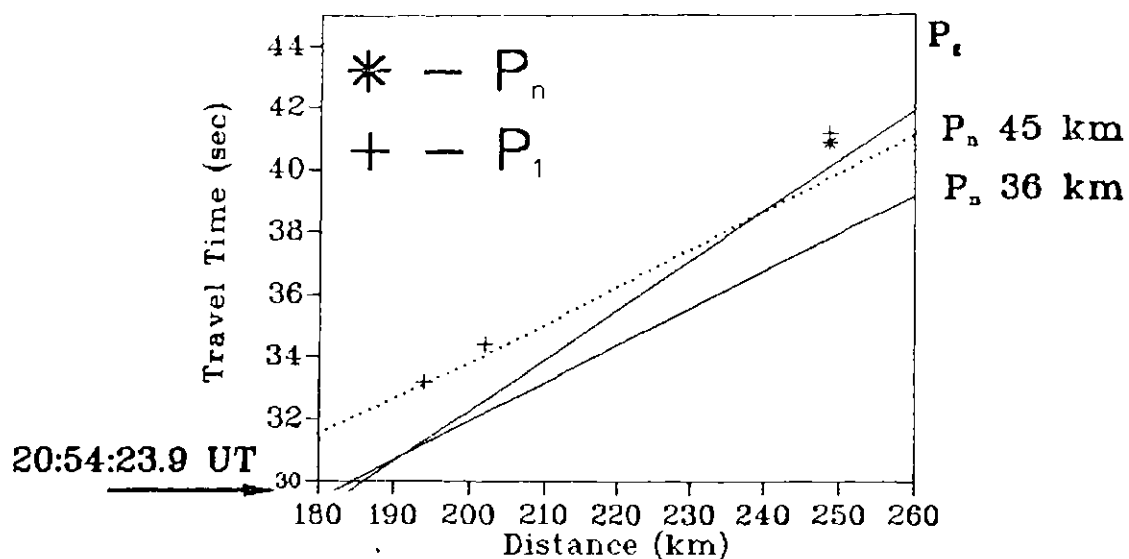


Figure 7.18. Comparison of phase arrival times from the Kuroki earthquake to times suggested by the GSC model. The GSC origin time estimate was used to make the graphs. Two  $P_n$  travel time functions are given in the figure. They correspond to Moho depths of 36 (solid) and 45 km (dashed).

velocity is neither  $P_g$  or  $P_n$ . This suggests that the  $P_1$  arrivals must be refractions from a discontinuity within the crust.

The  $S_1$  arrivals identified on the USSN seismograms may be either surface waves or shear waves (figure 7.14). Their arrival times, plotted on figure 7.18, fall close to the  $S_g$  travel time function. However, the derived apparent velocity for the  $S_1$  arrival is 4.21 km/sec. Also, the COM  $S_1$  time is sooner than the trend suggested by the other two arrivals. That is, the  $S_1$  times do not follow a good linear trend, as a function of distance, between the stations. The derived Poisson's ratio between the  $S_1$  and  $P_1$  apparent velocities is 0.192, assuming  $S_1$  to be shear waves refractions from the same discontinuity as  $P_1$ . This ratio is too low for crustal refractions; an acceptable ratio would be around 0.23. That indicates that there may be a confusion between surface wave arrivals on the surface seismograms and a shear wave arrival on the COM seismogram. Due to the discrepancy, the  $S_1$  arrivals have not been used in the rest of the analysis.

#### 7.4.4 Origin Time

A new origin time estimate is needed because the GSC crustal model P phase arrivals disagree with the observations on the USSN seismograms. The  $P_n$  arrival at COM has a known travel time function (figure 7.6), and therefore

the phase can be used to find a new origin time. An estimate for the depth to the inter-crustal  $P_1$  refractor can then be given.

The results of the origin time analysis are given in table 7.3. Three cases were assumed for the analysis. The first two cases investigate the affect of changing the  $P_n$  velocity. Regional earthquakes show a  $P_n$  velocity of 8.3 km/sec. However, refraction data in southern Saskatchewan shows velocities of 8.2 km/sec. There may be a velocity gradient in the upper mantle causing the discrepancies. The 8.2 km/sec velocity is more plausible for this analysis since the distances are similar to the offsets for the refraction surveys in southern Saskatchewan. The third  $P_n$  origin time analysis case investigates the effect of changing the focal depth from 1 km to 10 km. All three cases used a Moho depth of 46 km, and a crustal P-wave velocity of 6.16 km/sec. The P-wave model given in figure 7.1 was used for the sediments.

The three  $P_n$  derived origin time estimates (table 7.3) are all later than the GSC estimate. A difference of 0.5 sec is found using a focal depth of 1 km and a  $P_n$  velocity of 8.2 km/sec. This time of 20:53:54.4 UT will be used for the following analysis.

#### 7.4.5 Depth to $P_1$ Refractor

A depth of 26 km for the  $P_1$  refractor is obtained using

P<sub>n</sub> Origin Time Analysis Using COM Seismogram

For all the arrival times listed below,  
the reference time = 20:52:30

FOR EXAMPLE: an arrival time of 20:53:31 would give  
a tabulated arrival time of 61 sec.

Note:

---

COM P<sub>n</sub> arrival time — 124.8 sec (corrected for receiver  
depth)

---

Case 1:

Assume focal depth = 1 km and P<sup>n</sup> velocity = 8.2 km/sec

$$\begin{aligned} T_1 &= 10.1 \text{ sec} \\ T_0 &= 84.4 \text{ sec} = 20:53:54.4 \end{aligned}$$

Case 2:

Assume focal depth = 1 km and P<sup>n</sup> velocity = 8.3 km/sec

$$\begin{aligned} T_1 &= 10.2 \text{ sec} \\ T_0 &= 84.7 \text{ sec} = 20:53:54.7 \end{aligned}$$

Case 3:

Assume focal depth = 10 km and P<sup>n</sup> velocity of 8.2 km/sec

$$\begin{aligned} T_1 &= 9.1 \text{ sec} \\ T_0 &= 85.4 \text{ sec} = 20:53:55.4 \end{aligned}$$

---

Table 7.3. Origin time analysis using P<sub>n</sub>.

the origin time estimate, and a upper crust P-wave velocity of 6.16 km/sec. The depth was calculated via refraction delay time analysis, assuming flat layers. Refraction modeling was then used to ensure that the depth for the  $P_1$  refractor gives P-wave arrival times similar to the observed times. That is, arrival times for  $P_n$ ,  $P_g$  and the  $P_1$  phase were calculated at each USSN station. The results are given on a travel time graph in figure 7.19. This graph shows that refractions with an apparent velocity of 6.81 km/sec, from a flat layer at 26 km depth, are hidden. The first arrivals at BLK and BRG would be  $P_g$  — not the observed  $P_1$ . The investigation suggests that the assumption of a flat layer is invalid. More analysis will be presented after a discussion on the Riel discontinuity.

#### 7.4.6 Suggestion for the Presence of the Riel Discontinuity

Crustal data from many parts of the world suggests the presence of correlatable deep crustal horizons up to distances as great as 200 km (Kulhánek, 1990). However, in Canada, crustal data suggests that the Moho is the only deep reflector that can be correlated across the continent (Chandra and Cumming, 1972). Crustal studies in southern Alberta have revealed the presence of a deep crustal reflecting layer with a P wave velocity higher than 7 km/sec (Kanasewich and Cumming, 1965). Clowes et al. (1968)

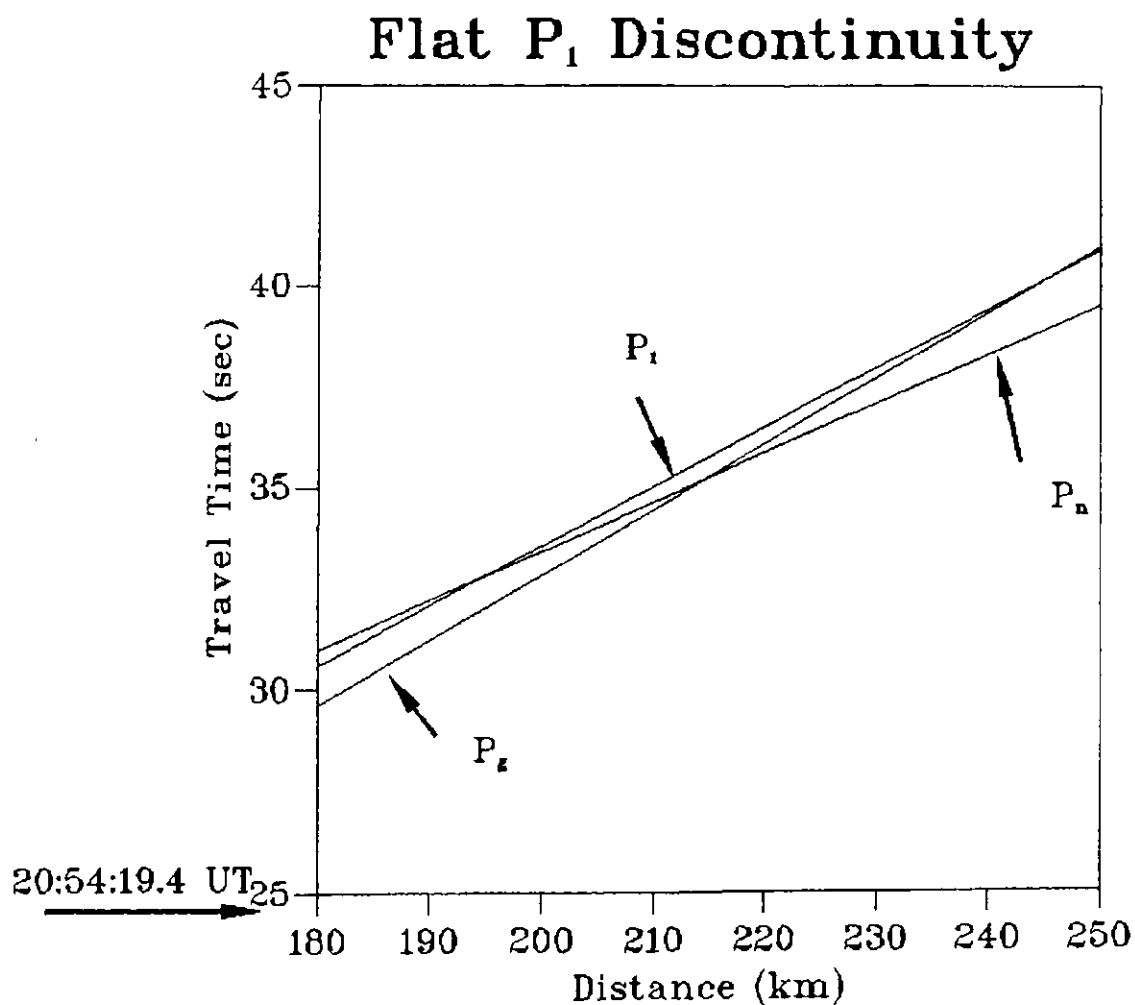


Figure 7.19. P phase arrivals assuming a flat  $P_1$  discontinuity. The depth to the  $P_1$  horizon was 26 km. The graph shows that  $P_1$  would never be observed as a first arrival for this case.

renamed the horizon the "Riel" discontinuity because the velocity contrast is different from that of the Conrad in Europe. Hall and Brisbin (1965) noticed a similar deep crustal horizon in Manitoba which they named the Conrad. Later, the Riel notation was suggested for the discontinuity by Hall and Hajnal (1973). Sprenke (1982) used inversion of gravity data in Western Canada to suggest that there are actually two deep crustal discontinuities in Alberta and Manitoba. These horizons were named "Riel A" and "Riel M". Kanasewich et al. (1987) have found both discontinuities present on their refraction data in southern Saskatchewan (discussed in section 7.1). The P wave velocities are 6.6 km/sec for Riel M at 20 km depth, and 7.0 km/sec for Riel A at 34 km depth. Kanasewich et al. (1987) emphasize "that these are not known to be continuous geological horizons but are convenient geophysical designations."

The analysis of the Kuroki earthquake suggests that the so-called Riel discontinuity/discontinuities may also be present under Saskatoon, and for some distance to the east. The apparent velocities measured here disagree with those suggested by Kanasewich et al. (1987), although the derived depth is close to that of the Riel A. It is possible that the velocities suggested by Kanasewich et al. (1987) are not observed from the  $P_1$  refractions, because the discontinuity is dipping under Saskatoon. A dip of 4.5 deg towards the east, on the Riel A, will give the observed apparent velocity. If the refractor is the Riel M, a dip of about 4

deg towards the west is needed. Either case is plausible according to the seismic image of southern Saskatchewan, interpreted by Hajnal et al. (1984; figure 7.3).

Refraction arrival times from Riel A, and from Riel M, were calculated assuming dips on the horizons, under the array. This implies that the dips occur over a distance of about 50 km. The analysis showed that a dip of 4.5 deg on the Riel A, with a velocity of 6.6 km/sec, and a depth of 20 km below the BKL station, would produce the observed arrival times for both  $P_1$  and  $P_n$  (figure 7.20). A dipping Riel M does not match the observations. Figure 7.20 shows that the Riel A refractions would only be observed as first arrivals between epicentral distances of about 180 to 230 km.

#### 7.5 A New Crustal Model for the Saskatoon Area

A crustal model for the Saskatoon area is given in figure 7.21. The seismograms from the Kuroki earthquake show that both the Riel A and M may have to be considered for origin time analysis and location procedures. A dip is suggested on Riel A, although the dip value will have to be used with caution for earthquakes from azimuths other than the east. Additional data will give more constraint on the dip estimates and attitudes.

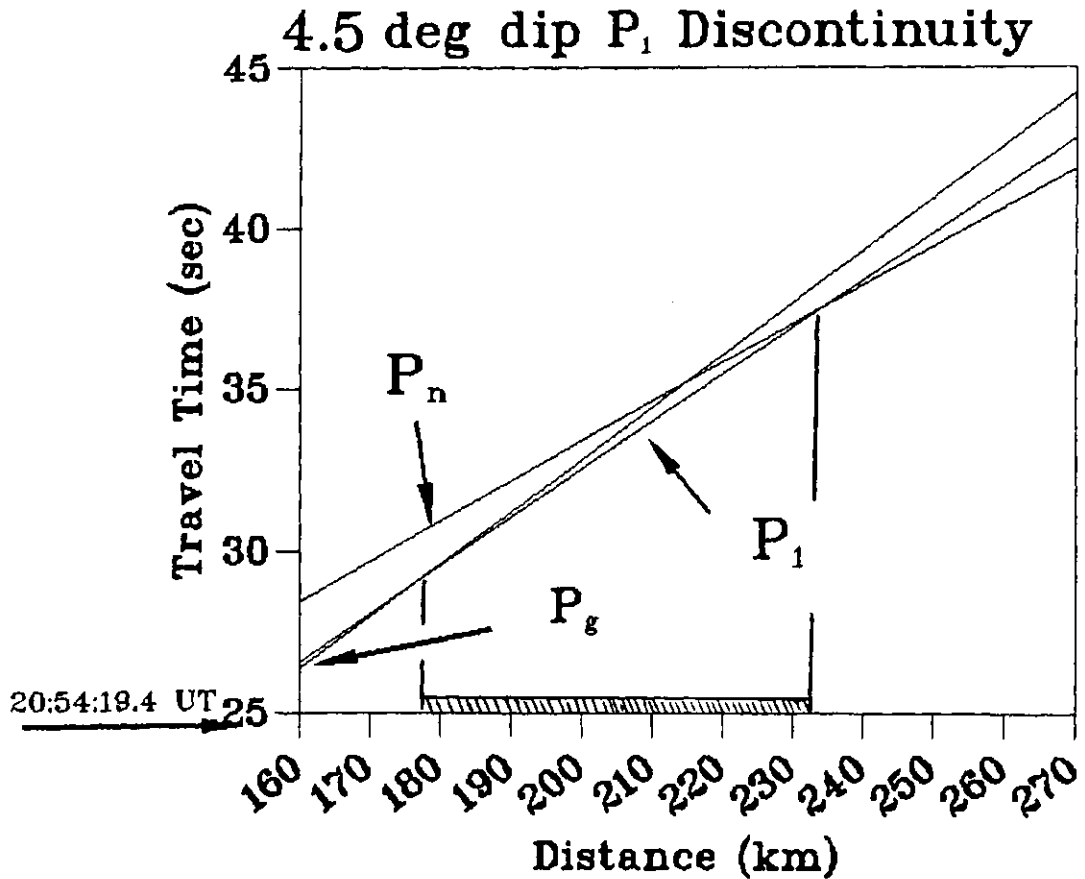


Figure 7.20. P phase arrivals assuming a 4.5 deg dip on the Riel A discontinuity. A depth to the Riel A horizon of 20 km was assumed under BLK. The horizon dip was up towards the west. The graph shows that the refractions would be observed over a very limited range.

Sediments

2.1 / 1.1	0.6
5.0 / 2.9	1.7

Note:

Velocities in km/sec P / S
----------------------------------

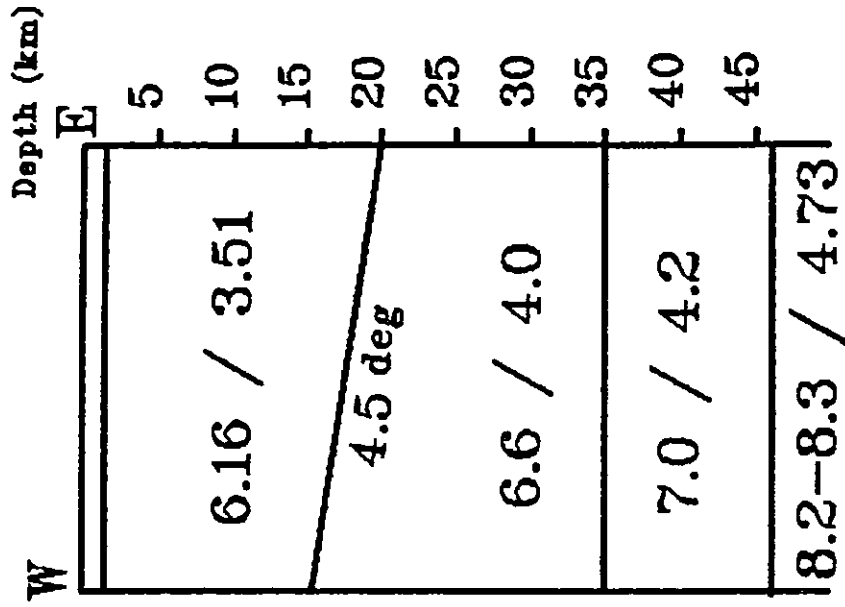


Figure 7.21. A crustal model for the Saskatoon area.

## CHAPTER 8

CONCLUSIONS

This work has established the University of Saskatchewan Seismograph Network for earthquake analysis. The array detector proves to be effective for recognizing events that are nearly imperceptible on the helicorder paper records. The volume of detected events has increased significantly since the initiation of the detector. The instrument response deconvolution is a crucial part of the analysis of the detected earthquakes. The procedure enhances phase arrivals and restores the true ground motions on the digital seismograms. This provides accurate phase arrival time assessments, and also makes both magnitude and spectral analysis possible.

The ambient earth-noise study shows that the noise levels at the USSN stations are quite low. Both the vault and the underground station prove to be effective in reducing the noise levels. The noise study indicates that the most desirable location for a seismograph station is underground. An improvement of  $0.5 M_N$  units in magnitude threshold is realized at the 1 km deep COM station.

The noise study and calibration experiments offer recommendations on the instrumental gain settings. The study suggests that the present gain setting of 78 dB is too large for the needs of the system. Seismograms would be

distorted for Saskatchewan earthquakes larger than about magnitude 4.0. Such earthquakes have occurred in the past. It is recommended that the gains should be lowered to 72, or even 66 dB.

The crustal study is the first investigation of the crust below the Saskatoon area. The results indicate that the crust is quite complicated. The fractured nature of the basement may be causing travel time delays as large as 0.4 sec for teleseismic earthquake P-waves. The local Kuroki earthquake seismograms reveal that a simple two layer crustal model is inadequate for the area. Furthermore, dipping horizons, at 20 km depth, may have to be considered for local earthquake seismogram analysis.

REFERENCES

- Aki, K. (1967). Scaling law of seismic spectrum, Journal of Geophysics Research, V72, pp. 1217-1231.
- Allen, R. V. (1978). Automatic earthquake recognition and timing from single traces, Bulletin of the Seismological Society of America, V68, pp. 1521-1532.
- Allen, R. V. (1982). Automatic phase pickers: their present use and future prospects, Bulletin of the Seismological Society of America, V72, pp. S225-S242.
- Anton, H. (1977). Elementary Linear Algebra, John Wiley & Sons, Toronto.
- Bache, T.C., Marshall, P.D. and Young, J.B. (1986). High frequency seismic noise characteristics at the four United Kingdom-type arrays, Bulletin of the Seismological Society of America, V76, pp. 601-616.

- Basham, P.W., and Whitham, K. (1966). Microseismic noise on Canadian seismograph records in 1962 and station capabilities, Publications of the Dominion Observatory, V32, pp. 123-135.
- Bath, M. (1974). Spectral Analysis in Geophysics, Elsevier Scientific Publishing Co., Amsterdam.
- Berger, J., Eissler, H.K., Vernon, F.L., Nersesov, I.L., Gokhberg, M.B., Stolyrov, O.A., and Tarasov, N.T. (1988). Studies of high-frequency seismic noise in eastern Kazakhstan, Bulletin of the Seismological Society of America, V78, pp. 1744-1758.
- Berteussen, K.A. (1975). Array data in crustal structure research, Proc. of NATO Advanced Study Institute, Sandefjord, Norway, Noordhoff International Publishing, pp. 463-470.
- Blandford, R. R. (1982). Seismic event detection, Bull. Seism. Soc.Am. 72, S69-S87.
- Brune, J.N. (1970). Tectonic stress and the spectra of seismic shear waves from earthquakes, Journal of Geophysics Research, V75, pp. 4997-5009. Correction to paper (1971). Journal of Geophysics Research, V76, P 5002.

- Brune, J.N. (1971). Correction (to 1970 paper). Journal of Geophysics Research, V76, P. 5002.
- Bungum, H., and Husebye, E.S. (1971). Errors in time delay measurements, Pure and Applied Geophysics, V91(VIII), pp. 56-70.
- Bungum, H., Mykkeltveit, S., and Kvaerna, T. (1985). Seismic noise in Fennoscandia, with emphasis on high frequencies, Bulletin of the Seismological Society of America, V75, pp. 1489-1513.
- Carter, J.A., Barstow, N., Pomeroy, P.W., Chael, E.P., and Leahy, P.J. (1991). High-frequency seismic noise as a function of depth, Bulletin of the Seismological Society of America, V81, pp. 1101-1114.
- Chandra, N.N. and Cumming, G.L. (1972). Seismic refraction studies in Western Canada, Canadian Journal of Earth Sciences, V9, pp. 1099-1109.
- Christopher, J.E., Kent, D.M., and Simpson, F. (1971). Hydrocarbon potential of Saskatchewan, Saskatchewan Department of Mineral Resources, Report No. 157.

- Clowes, R.M., Kanasewich, E.R., and Cummings G.L. (1968).  
Deep crustal reflections at near-vertical incidence,  
Geophysics, V33, pp. 441-451.
- Douze, E.J. (1967). Short period seismic noise, Bulletin  
of the Seismological Society of America, V57, pp. 55-  
81.
- Engdahl, E.R., and Felix, C.P. (1971). Nature of travel  
time anomalies at LASA, Journal of Geophysical  
Research, V76, pp. 2706-2715.
- Espinosa, A.F., Sutton, G.H., and Miller, H.J. (1962). A  
transient technique for seismograph calibration,  
Bulletin of the Seismological Society of America,  
V52, 767-779.
- Fix, J.E. (1972). Ambient earth motion in the period  
range from 0.1 to 2560 sec, Bulletin of the  
Seismological Society of America, V62, pp. 1753-1760.
- Frantti, G.E. (1963). The nature of high-frequency earth  
noise spectra, Geophysics, V28, pp. 547-562.
- Freiberger, W. F. (1963). An approximate method in signal  
detection, Quaterly Journal of Applied Mathematics,  
V20, pp. 373-378.

- Gendzwill, D.G., Horner, R.B., and Hasegawa, H.S. (1982).  
Induced earthquakes at a potash mine near Saskatoon,  
Canada, Canadian Journal of Earth Sciences, V19, pp.  
466-475.
- Gendzwill, D.G. (1984). Induced seismicity in  
Saskatchewan potash mines, Proc. of first symposium  
of Rockbursts and Seismicity in Mines, Johannesburg,  
South African Institute of Mining and Metallurgy,  
Editors: Gay, N.C., and Wainwright, E.H., pp. 131-  
146.
- Gendzwill, D.G., and Prugger, A.F. (1990). Seismic  
activity in a flooded Saskatchewan potash mine,  
Minneapolis, Minnesota, Proc. of second symposium of  
Rockbursts and Seismicity in Mines, Minneapolis.
- Given, H.K. (1990). Variations in broadband seismic noise  
at IRIS/IDA stations in the USSR with implications  
for event detection, Bulletin of the Seismological  
Society of America, V80, pp. 2072-2088.
- Gledhill, K.R. (1985). An earthquake detector employing  
frequency domain techniques, Bulletin of the  
Seismological Society of America, V75, pp. 1827-1835.

- Goforth, T. and E. Herrin (1980). An automatic seismic signal detection algorithm based on the Walsh transform, *Bulletin of the Seismological Society of America*, V71, pp. 1351-1360.
- Green, A.G. (1980). Delineation of geological contacts by seismic refraction with application to the fault zone between the Thompson Nickel Belt and the Churchill Tectonic Province, *Canadian Journal of Earth Science*, V18, pp. 13-25.
- Gurrola, H., Minster, J.B., Given, H., Vernon, F., Berger, J. and Aster, R. (1990). Analysis of high frequency seismic noise in the western United States and eastern Kazakhstan, *Bulletin of the Seismological Society of America*, V80, pp. 951-970.
- Hall, D.H., and Brisbin, W.C. (1965). Crustal structure from converted head waves in central western Manitoba, *Geophysics*, V30, pp. 1053-1065.
- Hall, D.H., and Hajnal, Z. (1973). Deep seismic crustal studies in Manitoba, *Bulletin of the Seismological Society of America*, V63, pp. 885-910.

- Hajnal, Z., Fowler, C.M.R., Mereu, R.F., Kanasewich, E.R., Cumming, G.L., Green, A.G., and Mair, A. (1984). An initial analysis of the earth's crust under the Williston Basin: 1979 COCRUST Experiment, *Journal of Geophysical Research*, V89 (B11), pp. 9381-9400.
- Hamming, R.W. (1983). *Digital Filters*. Prentice-Hall Inc., Englewood Cliffs, N.J.
- Hauksson, E., Ta-Liang, T., and Henyey, T.L. (1987). Results from a 1500 m deep, three-level downhole seismometer array: site response, low Q values, and  $f_{\max}$ , *Bulletin of the Seismological Society of America*, V77, pp. 1883-1904.
- Herrin, E., Arnold, E.P., Bolt, B.A., Clawson, C.E., Engdahl, E.R., Freedman, H.W., Gordon, D.W., Hales, A.L., Lobdell, J.L., Nuttli, O., Romney, C., Taggart, J., and Tucker, W. (1968a). Seismological tables for P phases, *Bulletin of the Seismological Society of America*, V58, pp. 1193-1241.
- Herrin, E., Tucker, W., Taggart, J., Gordon, D.W., and Lobdell, J.L. (1968b). Estimation of surface focus P travel times, *Bulletin of the Seismological Society of America*, V58, pp. 1273-1291.

- Horner, R.B., and Hasegawa, H.S. (1978). The seismotectonics of southern Saskatchewan, Canadian Journal of Earth Sciences, V15, pp. 1341-1355.
- Horner, R.B., Stevens, A.E., and Hasegawa, H.S. (1973). The Bengough, Saskatchewan, earthquake of July 26, 1972, Canadian Journal of Earth Sciences, V10, pp. 1805-1821.
- Horner, R.B., Stevens, A.E., and Wetmiller, R.J. (1980). Canadian earthquakes—1978/Tremblements de terre Canadiens—1978. Seismological Series of the Earth Physics Branch, No. 83.
- Hudson, J.A. (1980). The Excitation and Propagation of Elastic Waves, Cambridge University Press, Great Britian.
- Isacks, B. and Oliver, J. (1964). Seismic waves with frequencies from 1 to 100 cycles per second recorded in a deep mine in northern New Jersey, Bulletin of the Seismological Society of America, V54, pp. 1941-1980.
- Joswig, M. (1990). Pattern recognition for earthquake detection, Bulletin of the Seismological Society of America, V80, pp. 170-186.

- Kanasewich, E.R., and Cumming, G.L. (1965). Near-vertical incidence seismic refraction from the 'Conrad' discontinuity, *Journal of Geophysical Research*, V70, pp. 3441-3446.
- Kanasewich, E.R., Hajnal, Z., Green, A.G., Cumming, G.L., Mereu, R.F., Clowes, R.W., Morel-A-L'Huissier, P., Chiu, S., Macrides, C.G., Shahriar, M., and Congram, A.M. (1987). Seismic studies in the crust under the Williston Basin, *Canadian Journal of Earth Science*, V24, pp. 2160-2171.
- Karnik, V. (1969). Seismicity of the European Area, Part I. Reidel Publishing Company, Dordrecht-Holland.
- Kent, D.M. (1973). Paleozoic hydrocarbon reservoirs in Saskatchewan and their relationship to basement lineaments, *Journal of Canadian Petroleum Technology*, V12, pp. 20-24.
- Kromer, R.P. (1986). Wind effects on the NRSA High-Frequency Seismic Element (HFSE), in *Proceedings of the 1986 RSTN/NORESS Research Symposium*, 30 April to May 1986, Lawrence Livermore National Lab., pp. 116-133.

- Kulhánek, O. (1990). Anatomy of Seismograms. Elsevier Science Publishers, Amsterdam.
- Magotra, N., Ahmed, N. and E. Chael (1986). A comparison of two parameter estimation schemes, IEEE Proc. V74, pp. 760-761.
- Magotra, N., Ahmed, N. and E. Chael (1987). Seismic event detection and source location using single-station (three-component) data, Bulletin of the Seismological Society of America, V77, pp. 958-971.
- Magotra, N., Ahmed, N. and E. Chael (1989). Single-station seismic event detection and location, IEEE Transactions. on Geoscience and Remote Sensing, V27, 15-23.
- Mark Products, Inc. (1992). Mark Products Catalogue, Mark Products, Ltd., 1108 55th Ave. N.E., P.O. Box 73, Calgary, Alta, Canada, T2P 2G9.
- Mok, K.H., Mereu, R.F., and Yapp, A.P. (1982). A study of slowness anomalies around London, Ontario from University of Western Ontario seismic array observations, Canadian Journal of Earth Sciences, V19, pp. 1810-1816.

- Morel-A-L'Huissier, P., Green, A.G. and Pike, C.J. (1987).  
crustal refraction surveys across the Trans-Hudson  
orogen/Williston Basin of south central Canada,  
Journal of Geophysical Research, V92 (B7), pp. 6403-  
6420.
- Noble, B. and J.W. Daniel (1977). Applied Linear Algebra,  
Prentice-Hall, Inc., Englewood Cliffs, New Jersey.
- Nuttli, O.W. (1973). Seismic wave attenuation and  
magnitude relations for eastern North America,  
Journal of Geophysical Research, V78, pp. 876-885.
- Pho, H.T. and Behe, L. (1972). Extended distances and  
angles of incidence of P waves, Bulletin of the  
Seismological Society of America, V62, pp. 885-902.
- Richter, C.F. (1958). Elementary Seismology, W. H.  
Freeman Co., San Francisco.
- Rind, D. and Donn, W.L. (1979). Microseisms at Palisades.  
2. Rayleigh and Love wave characteristics and the  
geological control of propagation, Journal of  
Geophysical Research, V84, pp.5632-5642.

Rind, D. (1980). Microseisms at Palisades. 3. Microseisms and microbaroms, *Journal of Geophysical Research*, V85, pp. 4854-4862.

Roberts, R.G., Christoffersson, A., and Ingate, S.F. (1989). Real time event detections, phase identification and source location estimation using single-station three-component seismic data, *Geophys. J. Int.* V97, pp. 471-480.

Rodgers, P.W., Taylor, S.R., and Nakanishi K.K. (1987). System and site noise in the regional seismic test network from 0.1 to 20 Hz, *Bulletin of the Seismological Society of America*, V77, pp. 663-678.

Ruud, B.O. and Husebye, E.S. (1992). A new three-component detector and automatic single-station bulletin production, *Bulletin of the Seismological Society of America*, V82, pp. 221-237.

Samson, J.C. and J.V. Olson (1981). Data-adaptive polarization filters for multichannel geophysical data, *Geophysics* V46, pp. 1423-1431.

- Shebalin, N.V. (1959). Correlation between magnitude and intensity of earthquakes; asthenosphere, Publication du Bureau central international de seismologie, Travaux Scientifiques A20, pp. 31-37.
- Simpson, F., and Dennison, E.G. (1975). Subsurface waste-disposal potential of Saskatchewan, Saskatchewan Department of Mineral Resources, Report No. 177.
- Sorrells, G.G., McDonald, J.A., Der Z.A., and Herrin, E. (1971). Earth motions caused by local atmospheric pressure changes, Geophysical Journal of the Royal Astronomical Society, V26, pp. 83-98.
- Spottiswoode, S.M. and McGarr, A. (1975). Source parameters of tremors in a deep level gold mine, Bulletin of the Seismological Society of America, V65, pp. 93-112.
- Sprenke, K.F. (1982). Potential field inversion. Ph.D thesis, University of Alberta, Edmonton, Alta.
- Swindell, W.H. and N.S. Snell (1977). Station processor automatic signal detection system, Phase I: Final Report, Station Processor Software Development, Report ALEX(01)-FR-77-01, AFTAC Contract F08606-76-C-0025, Texas Instruments, Dallas.

- Thomas, G.E. (1974). Lineament-block tectonics: Williston-Blood Creek Basin, American Association of Petroleum Geologists Bulletin, V58, pp. 1305-1322.
- Toksöz, M.N. and Lacoss, R.T. (1968). Microseisms: mode structure and sources, Science, V159, pp. 872-873.
- VanDecar, J.C., and Crosson, R.S. (1990). Determination of teleseismic relative phase arrival times using multi-channel cross-correlation and least squares, Bulletin of the Seismological Society of America, V80, pp. 150-169.
- Willmore, P.L. (1975). Characteristics of seismic transducers, array transmission and recording, Proc. of NATO Advanced Study Institute, Sandefjord, Norway, Noordhoff International Publishing, pp. 25-35.
- Wyss, M., and Hanks, T.C. (1972). The source parameters of the San Fernando earthquake inferred from teleseismic body waves, Bulletin of the Seismological Society of America, V62, pp 591-602.
- Zhu, C. (1992). A seismic study of the northern Williston Basin, PhD thesis, University of Saskatchewan, Saskatoon.

## APPENDIX A

## Theory for Three-Component Event Detection

Generally, the first arrivals of energy from earthquakes are P phases and these phases are well polarized along the direction of propagation. Magotra et. al. (1987) projected the two horizontal channels of a three-component station onto the line of travel of the seismic signal to obtain maximum variance of the signal. That should provide improved S/N for detection as compared to single channel event detectors. The following discussion reviews the theory presented by Magotra et. al. (1989) where they expand their theory to use all components of a three-component station.

A projection  $y$ , which maximizes the variance for a  $3 \times 1$  data vector  $X$  (ie. vertical, east, and north components) is desired. The scalar  $y$  can be shown as a dot product

$$y = u^T \cdot X = \begin{bmatrix} u_1 & u_2 & u_3 \end{bmatrix} \cdot \begin{bmatrix} v \\ e \\ n \end{bmatrix},$$

where:  $u$  is a unit vector in the  
direction of maximum variance.

The scalar  $y$  is assumed to have a zero mean

$$y = E[y] = E[u^T X] = 0.$$

Therefore the variance of  $y$  is simply

$$\sigma^2 y = E[y^2] = u^T C u.$$

$C$  is the covariance matrix and is defined as

$$C = \begin{bmatrix} \sigma^2 n & \sigma n e & \sigma n v \\ \sigma n e & \sigma^2 e & \sigma e v \\ \sigma n v & \sigma e v & \sigma^2 v \end{bmatrix} = E[X X^T].$$

The variance  $\sigma^2 y$  must be maximized in the direction of  $u$  and this is possible if

$$(C - \lambda_m I)u = 0 \quad A1.$$

is satisfied (Magrota et. al., 1987). Equation A1 implies that for maximum variance,  $\lambda_m$  is a maximum eigenvalue of the covariance matrix  $C$ , and  $u$  is an eigenvector corresponding to  $\lambda_m$  which points in the direction of maximum variance.  $\lambda_m$  is proportional to the total power in the seismic signal, as will be illustrated in the next section.

### Properties of the Theoretical Data Covariance Matrix

Several assumptions for the Covariance matrix must be made:

- 1 The signal is perfectly polarized on all three orthogonal components;
- 2 The noise is white, zero mean, Gaussian distributed

and does not correlate between channels;

3 The signal and noise do not correlate.

Assumption 3 implies that since the signal and noise are dissimilar, one can model the recorded seismic data as a combination of signal and noise,

$$X(m) = X_s(m) + X_n(m),$$

where:  $m$  is the current time sample,

$X_s(m)$  is the signal vector,

$X_n(m)$  is the noise vector.

The covariance matrix of  $X(m)$  is

$$C(m) = C_s(m) + C_n(m),$$

where:  $C_s(m)$  and  $C_n(m)$  are the covariance matrices of the signal and noise.

The signal covariance matrix has the form

$$C_s(m) = \begin{bmatrix} \sigma^2_n & \sigma_{ne} & \sigma_{vn} \\ \sigma_{ne} & \sigma^2_e & \sigma_{ev} \\ \sigma_{vn} & \sigma_{ev} & \sigma^2_v \end{bmatrix},$$

and the noise covariance matrix has the form

$$C_n(m) = \begin{bmatrix} \sigma^2 & 0 & 0 \\ 0 & \sigma^2 & 0 \\ 0 & 0 & \sigma^2 \end{bmatrix} .$$

$C_n(m)$  has this form due to assumption 2, ie. noise does not correlate between channels.

Since  $C_n(m)$  is a diagonal matrix it has three eigenvalues ( $\lambda$ ) which are all equal to  $\sigma^2$ . Due to assumption 1,  $C_s(m)$  has only one non-zero eigenvalue (Samson and Olson, 1981) and therefore this eigenvalue is simply the sum of the trace of  $C_s(m)$  (Noble and Daniel, 1977)

$$\lambda_1^C s = \sigma^2 v(m) + \sigma^2 n(m) + \sigma^2 e(m) = \sigma^2 s(m),$$

where:  $\sigma^2 s(m)$  is the maximum variance of the seismic signal.

The eigenvalues of  $C(m)$  (ie. the observed covariance matrix) are the sum of the eigenvalues of  $C_n(m)$  and  $C_s(m)$

$$\lambda_1^C(m) = \sigma^2 s(m) + \sigma^2,$$

$$\lambda_2^C(m) = \sigma^2,$$

$$\lambda_3^C(m) = \sigma^2.$$

The above observations imply that if a highly linear perfectly polarized signal occurs in a random noise field, the covariance matrix will yield a unique maximum eigenvalue,  $\lambda_m$ . Theoretically,  $\lambda_m$  should be observed in any amount of noise, therefore a seismic detection algorithm

which monitors  $\epsilon_m$  should be a very good signal detector.

The original signal detection theory developed by Freiburger (1963) stated that the optimum signal detection algorithm is a power detector. Hudson (1980) gave an equation for the magnitude of energy flux (EF),

$$EF = \rho \alpha (dv/dt)^2,$$

where:  $\rho$  is density of the medium,

$\alpha$  is propagation velocity,

$dv/dt$  is velocity of particle motion.

Energy flux has units of power/m<sup>2</sup> and is a maximum along the direction of travel of the wavefront (Hudson, 1980). The maximum eigenvalue of the covariance matrix in the presence of signal is a sum of the variance of the signal and noise. One can see that energy flux is proportional to variance and therefore, this detection scheme performs power detection on all three components of the seismic signal. This scheme should be superior to single component monitoring schemes because they cannot detect the total power in the signals and therefore will have lower S/N.

## APPENDIX B

## Computer Programs

All computer programs that have been mentioned in this thesis are available for viewing at the Department of Geological Sciences, University of Saskatchewan. Operation manuals are also offered with the programs.

The programs are written in FORTRAN 77, under Digital Control Language (DCL). UNIRAS software, version 6.1, is used for the graphics routines. IMSL software and VAXlab processing are used for some of the signal processing and interpolation sub-routines.

Assistance may be provided by Academic Computing Services, or D.J. Gendzwill, if one wants to view the programs. They are found in the Departments VAX 11/785 main-frame computer. The housing directories for the programs (and the associated sub-routines) are tabulated on the next page.

## Computer programs used for analysis:

---

Program	Directory	Purpose
US_CALBR	PUB2:[GSC.FUNKC.CALIBRATE]	USSN interactive instrument calibration.
US_DETECT	PUB2:[GSC.FUNKC.DETECT]	USSN real time event detection.
US_ANALYSE	PUB2:[GSC.FUNKC.PLOT]	USSN interactive event plotting, signal processing, and interpretation.

List of Figures

FIGURES

2.1	Map of the USSN array.....	7
2.2	USSN instrumentation.....	10
3.1	A calibration pulse sequence from the BRG station.....	17
3.2	Frequency response from the calibration pulse sequence in figure 3.1.....	18
3.3	A stacked set of calibration pulses.....	19
3.4	Frequency response derived from the stacked pulses in figure 3.3.....	20
3.5	A set of calibration operators and delta functions.....	22
4.1	Flow chart of the array detector.....	36
4.2	$f_m/f_{sm}$ versus delay for $f_{sm}$ .....	40
4.3	A regional event with a very weak initial phase arrival.....	41
4.4	Detector performance evaluation and false alarm analysis based on four months of operation.....	43
4.5	Seismograms of small detected events.....	45
5.1	Typical processing flow in US_ANALSE.....	47
5.2	Band-pass filtering.....	50
5.3	Improvements realized with deconvolution.....	52
5.4	The utility of cross-correlation.....	54
5.5	Example of an earthquake location map.....	57
5.6	Known Seismicity in the Williston Basin.....	59